# ON BUILDING AN APPARATUS FOR HYBRID ATOM-OPTOMECHANICS WITH ULTRACOLD LITHIUM

A Thesis

Presented to the Faculty of the Graduate School

of Cornell University

in Partial Fulfillment of the Requirements for the Degree of

Master of Science

by

Kristina Renee Colladay

August 2014

## ABSTRACT

Cavity quantum electrodynamics (cQED) is a central paradigm for the study of open quantum systems. The study of cQED aims to understand phenomena such as quantum decoherence and the emergence of semiclassical dynamics, striving to better connect empirical realism and axiomatic theory. Within this quantum regime, it is possible to prepare a mechanical oscillator in pure quantum states and observe how it evolves under interaction with the environment. Furthermore, quantum coupling of these mechanical systems to ultracold atomic systems offers a novel approach to controlling macroscopic systems at the quantum level. We are laying the experimental groundwork for hybrid atom-optomechanics where the optomechanical coupling is atom-mediated using an ultracold $^6$Li atomic gas. The ultracold $^6$Li gas is to be in close proximity with and strongly coupled to a high quality factor fused silica microtoroid resonator by confinement in a two-color evanescent wave optical dipole trap. The infrastructure, construction, and operation of an ultracold Li apparatus is presented and followed with a report of the characterization of our first observation of an ultracold lithium gas in the laboratory. Specifically, this thesis briefly covers theory and experimental implementation of laser cooling methods, development of the homemade laser and laser amplifier systems, and development and construction of the homemade electronic systems for the precise control and monitoring of atomic parameters. Finally, magneto-optical trap characterization methods and images of the cold atoms using time-dependent fluorescence imaging are shown and followed with a discussion of further work.

## ACKNOWLEDGMENTS

Many people have contributed to the success of this thesis, and I owe thanks to all of them.

First, I am grateful to Prof. Mukund Vengalattore for giving me the opportunity to be a part of his group and to work on building the lithium experiment. His incredible passion, never-ending myriad of ideas he contributed to this work, and the exceptional work environment he created have been crucial to the success of this thesis and to my development as a masters student.

I owe much thanks to my colleague in the lithium-6 experiment, Yogesh Patil, for his invaluable insights and close to instant understanding of many of the technical difficulties and physical effects. Much of the success of this thesis results from his insights during our countless discussions. Thank you so much for the time we spent in the lab together!

Many thanks to our undergraduate member, Airlia Shaffer-Moag, for a full set of crosstalk data on all 32 DIO circuits. Also, many thanks to all other group members from previous years who provided the original designs that the circuits in the lithium experiment are based upon.

Finally, I am grateful to those who were not directly involved in the lithium-6 experiment but nevertheless contributed to making this thesis a successful and very pleasant one. First, I thank Lauren Aycock for her guidance, encouragement and invaluable suggestions in the lab and on this thesis. I thank Collin Reynolds for pointing out some very key circuit issues and for his constant feedback and encouragement. Finally, I thank Srivatsan Chakram for his help and insights and for his willingness to discuss my questions!

To my instructors, mentors, and colleagues.

## TABLE OF CONTENTS


Acknowledgments . . . . . b
Dedication . . . . . c
Table of Contents . . . . . d
List of Tables . . . . . g
List of Figures . . . . . h

**1 Introduction** **1**
1.1 Motivation . . . . . 1
1.2 Overview of experiment . . . . . 2
1.3 Thesis overview . . . . . 3

**2 Theory** **5**
2.1 Cavity QED and hybrid atom-optomechanical systems . . . . . 5
2.2 Cavity optomechanics . . . . . 5
2.2.1 Optomechanical systems . . . . . 5
2.2.2 Cavity optomechanics Hamiltonian . . . . . 7
2.2.3 Cooling fused silica microtoroid resonators . . . . . 8
2.2.4 Optical coupling to a micromechanical resonator through a fiber taper . . . . . 9
2.2.5 Lowest mechanical modes of a microtoroidal resonator . . 10
2.3 Brief description of cooling techniques . . . . . 11
2.3.1 Doppler cooling . . . . . 11
2.3.2 Polarization gradient (Sisyphus) cooling . . . . . 12
2.3.3 Optical molasses . . . . . 14
2.4 Magnetic trapping of neutral alkali atoms . . . . . 15
2.5 Ultracold atoms in a magneto-optical trap . . . . . 17
2.5.1 Phase space density . . . . . 23
2.6 Ultracold atoms in optical potentials . . . . . 24
2.6.1 Optical dipole potential . . . . . 24
2.6.2 Two-color dipole trap near a dielectric surface . . . . . 26
2.6.3 Optical lattice potential . . . . . 28
2.6.4 Bragg scattering of atoms in an optical lattice . . . . . 29
2.7 Raman sideband cooling . . . . . 30
2.8 Evaporative cooling . . . . . 32
2.8.1 Fermi temperature as a function of trap frequency . . . . . 33
2.9 Saturated absorption spectroscopy for laser frequency locking . . 34
2.9.1 Locking the laser to the transition wavelength . . . . . 40
2.10 Hyperfine structure and fundamental properties of lithium . . . . 40

**3 Lithium Laser System** **43**
3.1 Laser light at the $^6$Li D2 transition by injection locking . . . . . 43
3.2 Homemade external cavity diode lasers . . . . . 48
3.2.1 PZT driver . . . . . 52
3.3 Homemade tapered amplifier . . . . . 53
3.4 Achieving desired frequency detunings from the atomic resonance 55
3.4.1 Double pass AOMs . . . . . 55
3.4.2 AOM efficiency . . . . . 57
3.4.3 Homemade AOM drivers . . . . . 59
3.5 Optical system for the magneto-optical trap . . . . . 61
3.6 Optical lattice laser system . . . . . 63

**4 Lithium Magnetic Field System** **68**
4.1 Magnetic quadrapole trap . . . . . 68
4.1.1 Power dissipation of anti-Helmholtz coils . . . . . 69
4.1.2 Helmholtz coils . . . . . 70
4.2 Current control of Helmholtz coils . . . . . 70
4.2.1 Magnetic field and current from lattice energy level spacing 70
4.2.2 Current control for Raman sideband cooling . . . . . 72

**5 Computer Control of Atomic Experiment** **83**
5.1 CICERO and ATTICUS . . . . . 83
5.2 Homemade digital input-output electrical isolators . . . . . 84
5.2.1 Digital channel-to-channel crosstalk . . . . . 85
5.3 Homemade analog electrical isolators . . . . . 86

**6 Vacuum System** **88**
6.1 Evolution from 3D to 2D/3D chambers . . . . . 88
6.2 Modifying an ultra-high vacuum chamber . . . . . 89
6.3 Sonicating ultra-high vacuum components . . . . . 92

**7 Controlling and Characterizing Ultracold Atomic Lithium** **93**
7.1 Measuring temperature of the ultracold lithium atom cloud . . . 93
7.1.1 Atom number from atomic fluorescence imaging . . . . . 93
7.1.2 Time-of-flight . . . . . 94
7.1.3 Release and recapture . . . . . 96

**A Improvements to the Experiment** **101**

**B Circuit Diagrams and Schematics** **102**
B.1 Digital input-output circuit diagrams . . . . . 102
B.1.1 Updated DIO circuit diagrams . . . . . 102
B.1.2 Suggested improvements to DIO board . . . . . 103
B.2 Helmholtz current control circuit diagrams . . . . . 104
B.2.1 Current control testing diagram and box layout . . . . . 104

B.2.2 Suggested improvements to current control circuit . . . . . 105

**Bibliography** **109**

## LIST OF TABLES

2.1 Brief table of fundamental properties of $^6$Li [11] . . . . . 42

## LIST OF FIGURES


2.1 Example of a silicon microtoroid resonator used in optomechanics 6
2.2 Displacement patterns of the mechanical modes of a microtoroidal resonator . . . 11
2.3 Illustration of Doppler cooling . . . 12
2.4 Zeeman shift of the $2^2S_{1/2}$ of $^6$Li . . . 16
2.5 Magnetic trapping potential for atoms having opposite spins . . 17
2.6 Optical force as a function of atom velocity and detuning . . . . 19
2.7 Example of spatial restoring force in 1D . . . 21
2.8 Magneto-optical trap . . . 22
2.9 Three counter-propagating laser beams used in a 3D MOT . . . . 22
2.10 Diagram of the magneto-optical trap . . . 23
2.11 Raman sideband cooling diagram . . . 31
2.12 Truncation and rethermalization during evaporative cooling . . . 33
2.13 Setup for saturated absorption spectroscopy . . . 36
2.14 Velocity vectors of pump and probe in lithium vapor cell . . . . . 37
2.15 Saturated absorption as a function of pump and probe frequency 37
2.16 Energy level diagram corresponding to crossover transmission peak . . . 39
2.17 Light of $\sigma+$ and $\sigma-$ polarizations give rise to the error signal . . 39
2.18 Fine and hyperfine structure of $^6$Li and $^7$Li . . . 41

3.1 Wavemeter output . . . 44
3.2 Free-running diode output power vs. internal diode temperature 45
3.3 Schematic of the injection locking scheme . . . 46
3.4 Real injection lock setup . . . 46
3.5 Output of the Fabry-Pérot as a function of PZT drive voltage . . 47
3.6 Angle of diffraction grating for ECDL . . . 50
3.7 Schematic of the homemade External Cavity Diode Laser . . . . 51
3.8 Schematic of the homemade tapered amplifier . . . 54
3.9 Diagram of Bragg scattering in a photoelastic material . . . . . 57
3.10 Double-pass AOM configurations for up- and down-shifting laser frequency . . . 58
3.11 Alignment and zero and first order output beam characteristics . 60
3.12 Typical VCO range of operation . . . 61
3.13 Nonlinearity characteristics of the VCO . . . 62
3.14 Laser system for the magneto-optical trap . . . 64
3.15 Lithium lattice depth . . . 65
3.16 Lattice light intensity, heating rate and atom lifetime as a function of laser detuning for a given lattice depth . . . 66

4.1 Magnetic field gradient in the lithium apparatus . . . 69
4.2 Orientation of Helmholtz coils . . . 71

4.3 Experimental setup of the Helmholtz coils control circuit . . . . . 73
4.4 Hall probe calibration for current control circuit . . . . . 75
4.5 Operation of the current control circuit used in Raman sideband cooling . . . . . 76
4.6 Crosstalk measurements between three current control circuits . 77
4.7 Risetime of the controlled current across inductor as a function of MOSFET drain-source voltage . . . . . 78
4.8 MOSFET sawtooth oscillations . . . . . 79
4.9 Bandwidth of the current control circuit . . . . . 80
4.10 Scheme for measuring current noise . . . . . 81
4.11 Current noise spectrum after addition of preamp . . . . . 82

5.1 Example of Cicero interface . . . . . 84
5.2 PXI and homemade digital input-output systems . . . . . 85
5.3 Crosstalk of the digital input-output circuits . . . . . 86

6.1 Diagram of the 2D/3D MOT lithium vacuum system . . . . . 89

7.1 Fluorescence collected by photodiode, lens, and iris . . . . . 94
7.2 Diagram of release and recapture imaging scheme . . . . . 97
7.3 Images of the lithium atom cloud at various delays . . . . . 98
7.4 Fit of the atom number to obtain atom cloud temperature . . . . 100

B.1 Digital input-output circuit schematic . . . . . 102
B.2 Digital input-output circuit board layout . . . . . 102
B.3 Suggested improvements to DIO circuit schematic . . . . . 103
B.4 Suggested improvements to DIO circuit board layout . . . . . 103
B.5 Schematic of the current control circuit . . . . . 104
B.6 Diagram of the current control circuit layout . . . . . 105
B.7 Testing current control circuit without connecting to the solid state relay . . . . . 106
B.8 Cross section of the MOSFET water-cooling plate . . . . . 107
B.9 Suggested improvement to current control circuit . . . . . 107
B.10 Suggested improvement to current control circuit board layout . 108

CHAPTER 1

# INTRODUCTION

## 1.1 Motivation

Cavity Quantum Electrodynamics (cQED) is a central paradigm for the study of open quantum systems. Cavity QED scrutinizes the gap between axiomatic theory and empirical realism, and seeks to clarify murky issues such as decoherence and the emergence of semiclassical dynamics [20]. Quantum electrodynamics implies the interaction of a material system with an electromagnetic field, and the term cavity refers to an optical or microwave resonator. Confinement or isolation of the system using a high-quality cavity prevents the system from decohering through interaction with the environment allowing for the observation of quantum coherence over dynamically important time scales.

Generating and measuring non-classical states of macroscopic mechanical oscillators is possible through coupling them to atomic quantum systems. We are laying the groundwork for hybrid atom-optomechanics where the optomechanical coupling is atom-mediated and achieved through bringing a ultracold $^6$Li atomic gas into close proximity with the microtoroid by its confinement in a two-color evanescent wave optical dipole trap. Coupling a silicon microtoroid resonator with a gas of ultracold atoms offers a novel approach to controlling mechanical systems at the quantum level [27]. Specifically, confining a Bose-Einstein condensate (BEC) to an optomechanical resonator can be used to observe state transfer between atomic Schrödinger fields and phonon fields. One particularly attractive aspect of quantum state transfer between micromechanical structures and atomic Schrödinger fields is that they can have extremely low dissipation and decoherence rates compared to optical fields in resonators [29].

Reaching this quantum regime makes it possible to prepare the mechanical oscillator in pure quantum states and observe how it evolves under interaction with the environment, potentially revealing yet unobserved decoherence mechanisms. From an applied perspective, these studies may also enable researchers to create biological sensors with improved sensitivity, force and displacement sensors with sensitivities beyond the standard quantum limit, or controlled quantum gates for quantum computation.

Here, I report on laying the experimental groundwork to creating an ultracold $^6$Li atomic gas for cavity quantum electrodynamics experiments using hybrid atom-optomechanics.

## 1.2 Overview of experiment

$^6$Li is an interesting candidate for interacting a Fermi gas with an object as it has anomalously large and attractive interactions and its critical temperature, $T_c$, for superfluid transition is highest for all BCS superfluids. Lithium is also subject to resonant scattering resonances, Feshbach resonances, which allow the interaction strength to be widely tuned with a bias magnetic field.

Our compact lithium apparatus evolved from a 3D magneto-optical trap (MOT) in which atoms are cooled directly from $^6$Li dispensers to a 2D-3D magneto-optical trap. The 2D stage acts as a source of precooled atoms from Li dispensers (now a lithium oven) in the 2D trap that are pushed by a beam into the 3D magneto-optical trap. The lifetime of the atoms in the magneto-optical trap is dependent on collisions with impurities in the chamber, therefore the pressures are kept at ultra-high vacuum, about $10^{-10}$-$10^{-11}$ Torr. To stabilize the laser frequency, we lock a 671 nm master laser to the $^7$Li D1 atomic transition lines using saturated absorption spectroscopy. The $^6$Li D2 and $^7$Li D1 lines have approxi-

mately the same wavelength, and $^6$Li is naturally less abundant, refer to Fig. 2.18 and Tab. 2.1. Atoms in the 3D MOT are then confined in an optical lattice formed by a counter-propagating beam and cooled further using Raman sideband cooling.

At later stages, fused silica microtoroid resonators will be introduced into the main chamber, also containing the 3D lithium MOT, for optomechanical cooling. Two colors of fiber-coupled laser light will be introduced through a flange into the vacuum chamber. The fiber in the chamber will have a taper to be brought within coupling range of the optical resonating waveguide of the microtoroid. This two-color light will leak out of the fiber taper and couple to resonant optical modes of the microresonator. The evanescent wave from the propagating light forms a two-color dipole trap that acts to confine Li atoms within close proximity to the microresonator resulting in a hybrid atom-optomechanical system.

## 1.3 Thesis overview

This thesis is divided into several sections. **Chapter 1** introduces and motivates our experiment. **Chapter 2** provides a brief introduction to cQED and cavity optomechanics. Fundamentals of our laser cooling techniques, the magneto-optical trap, Raman sideband cooling, and saturated absorption spectroscopy are reviewed. **Chapter 3** presents the development and assembly of the laser system, including the construction of homemade external cavity diode lasers, homemade tapered amplifiers, achieving the desired laser frequency detuning from atomic resonance, the design and construction of the magneto-optical trap, and on-going development of the optical lattice. **Chapter 4** presents in part the magnetic field system, including a discussion of the magnetic quadrapole trap, the role of the Helmholtz and anti-Helmholtz coils, and the construction

of electronic system for precise control and monitoring of the magnetic fields used in Raman sideband cooling. **Chapter 5** introduces operation of the software/hardware system used in precision timing and control atomic cooling and measurement sequences. Test results using this system and the development of homemade analog and digital electronics for isolation of control signals from the computer hardware are discussed. **Chapter 6** describes the development of our vacuum system from a 3D MOT to a 2D-3D MOT combination, and briefly discusses techniques used for ensuring ultra-high vacuum quality. **Chapter 7** describes the characterization of our first observation of an ultracold lithium gas using atomic fluorescence imaging techniques. The **Appendix** provides extra experimental details and follows up with a discussion of further work.

CHAPTER 2

# THEORY

## 2.1 Cavity QED and hybrid atom-optomechanical systems

Many questions in quantum optics can be addressed through the study of quantum electrodynamics. Within this quantum regime, if one degree of mechanical freedom is allowed, such as a movable mirror or a breathing mode, one obtains an optomechanical system. In a hybrid optomechanical system, a degenerate quantum gas is coupled to such a macroscopic optomechanical system. Atomic coupling leads to quantum mechanical control of the macroscopic object, and consequently, direct observation of a macroscopic mechanical system operating in the quantum regime.

## 2.2 Cavity optomechanics

### 2.2.1 Optomechanical systems

There are many optomechanical systems developed to date. Most of these can be categorized within one of five different groups: Fabry-Pérot cavities, superconducting microwave resonators, photonic crystal cavities, membrane in the middle resonators, and whispering gallery mode resonators. Fabry-Pérot optomechanical systems allow for the movement or vibration of one end mirror of the cavity. Gravitational wave detectors are an example of Fabry-Pérot cavities, and they are the largest optomechanical systems currently realized [6]. Superconducting microwave resonator systems (having applications in quantum computing [25]) can experience mechanical vibration which alters the resonance frequency of the resonator [15]. Photonic crystal cavities allow simultaneously

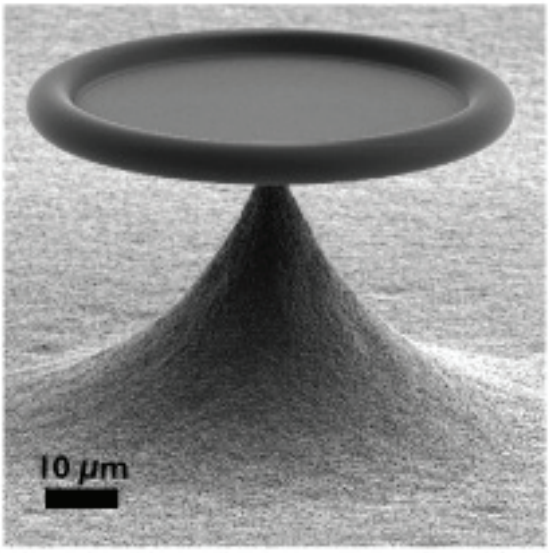


Figure 2.1: Example of a silicon microtoroid resonator used in optomechanics [18].

localized and strongly coupled optical and mechanical modes [10]. Membrane in the middle systems contain a partially reflective membrane (often SiN) that can form one mirror of a Fabry-Pérot cavity for 'reflective' optomechanical coupling, or can be placed between two highly reflective mirrors for 'dispersive' optomechanical coupling [30]. In both cases, optomechanical coupling results from the cavity resonance frequency shift produced by a small displacement of the membrane's position. Whispering gallery mode cavities can be spherically or toroidally shaped. An example is shown in Fig. 2.1. Mechanical eigenmodes that affect the optical path length are parametrically coupled to the light guided within the resonator.

Optomechanical cooling, as opposed to atomic cooling, does not rely on intrinsic resonances such as the atomic structure of the atom, but instead on the non-resonant radiation force acting on the mechanical system with resonant enhancement provided by the geometry of the optomechanical system [31].

### 2.2.2 Cavity optomechanics Hamiltonian

Optical and mechanical degrees of freedom are parametrically coupled in all types of optomechanical systems. The general equation below applies to all of the optomechanical systems described in Section 2.2.1 [31].

$$\hat{H} = \hat{H}_{mech} + \hat{H}_{opt} + \hat{H}_{int} + \hat{H}_{drive} \tag{2.1}$$

$$\hat{H}_{mech} = \frac{\hat{p}^2}{2m_{eff}} + \frac{1}{2} m_{eff} \Omega_m^2 \hat{x}^2 \tag{2.2}$$

$$\hat{H}_{opt} = \hbar\omega_c \left( \hat{a}^\dagger \hat{a} + \frac{1}{2} \right) \tag{2.3}$$

$$\hat{H}_{int} = \hbar g_0 \hat{x} \hat{a}^\dagger \hat{a} \tag{2.4}$$

$$\hat{H}_{drive} = i\hbar\sqrt{\eta_c \kappa} \left( \hat{s}_{in}(t) \hat{a}^\dagger e^{-i\omega_l t} - \hat{s}_{in}^\dagger(t) \hat{a} e^{i\omega_l t} \right) \tag{2.5}$$

$\hat{x}$ and $\hat{p}$ are the position and momentum operators of the mechanical degree of freedom, and $s_{in}(t)$ is the drive amplitude normalized to a photon flux at the input of the cavity $|s_{in}|^2 = P_{in}/\hbar\omega_l$. $\hat{a}$ and $\hat{a}^\dagger$ are the annihilation and creation operators of the cavity mode, and the coupling parameter is $\eta_c = \kappa_{ex}/(\kappa_0 + \kappa_{ex})$ where $\kappa_0$ is the intrinsic loss of the cavity related to absorption and scattering, $\kappa_{ex}$ is the loss by coupling to a waveguide and $\kappa_0 + \kappa_{ex}$ is the total optical energy decay rate. $m_{eff}$ is the effective mechanical mass of the oscillating mode, $g_0$ is the optomechanical coupling rate and is defined as the change in the optical resonance frequency as a function of displacement $\frac{d\omega_c}{dx}$. The shift in the optical resonance frequency with mechanical displacement is [31] [26],

$$\hat{H}_{opt} + \hat{H}_{int} = \hbar(\omega_c + g_o \hat{x}) \hat{a}^\dagger \hat{a} \tag{2.6}$$

and the radiation pressure force is,

$$F = -\frac{\partial \hat{H}_{int}}{\partial \hat{x}} = \hbar g_o \hat{a}^\dagger \hat{a}. \tag{2.7}$$

### 2.2.3 Cooling fused silica microtoroid resonators

In our experiment, we plan to use fused silica microtoroid resonators. Silicon microtoroids sustain simultaneously ultra-high finesse optical whispering gallery modes (WGM) and radial mechanical breathing modes (RBM). These two degrees of freedom are coupled. The mechanical motion of the microtoroid affects the optical resonance frequency, and the radiation pressure forces of an optical field contained in an optical mode act back on the mechanical motion. Because the lifetime of the intracavity field in the optical cavity is finite, the field amplitude also adjusts to the changing boundary conditions as induced by mechanical displacement in a retarded fashion. This gives rise to an effect known as dynamical backaction, and is the phenomenon allowing for optical cooling of the mechanical mode. Cooling of the resonator is done in the resolved sideband regime where the optical photon storage time exceeds the mechanical oscillation period [26]. Cooling below two thermal quanta gives rise to the quantum-coherent coupling regime, also called the strong coupling regime. In this regime, the optomechanical coupling rate exceeds the optical and mechanical decay rates as well as the mechanical decoherence rate. It is under these conditions that one may observe quantum-state transfer between optics and mechanics [31].

#### Measurement backaction

Fundamental limitations exist on quantum measurements in contrast to classical measurements. In an ideal classical system, no additional noise is added by measurement. However, a quantum mechanical measurement is in the regime of the Heisenberg uncertainty principle. The quantum mechanical measurement of one variable of a non-commuting pair, say the position, gives rise to

increased uncertainty in the other variable of the non-commuting pair, say the momentum. The increased uncertainty in momentum after the position measurement affects the value of the position measurement at a later time. This effect is called measurement backaction. Although this poses a fundamental limitation on measurement accuracy, it is possible to send uncertainty into an orthogonal variable that is not measured using entangled or squeezed states and non-demolition techniques.

Quantum-noise limited interferometry is used to measure mechanical displacement fluctuations of silicon microtoroidal resonators when cooled to the mechanical ground state to obtain accurate temperature measurement. When cooled to the mechanical ground state, measurement precision must be better than the expected zero-point position fluctuations of the mechanical mode.

### 2.2.4 Optical coupling to a micromechanical resonator through a fiber taper

Efficient power transfer from the fiber in the vacuum chamber into the optical waveguide mode of the microtoroid resonator is desired not only to preserve laser power, but also losses allow quantum vacuum into the cavity mode which can cause noise and reduced measurement precision. Efficient coupling rates are achieved using the fundamental spatial mode of a fiber taper and by tangentially approaching the resonator with a tapered fiber leading to a phase matching condition [5]. Fiber tapers can be made using a single-mode optical fiber and heating it with a torch while pulling on either side until the center part of the taper has a diameter on the order of the light's wavelength. The coupling strength of the light into the microtoroid can be adjusted by changing the dis-

tance between the microtoroid and the optical fiber taper. The coupling rate increases exponentially as a function of the distance of the fiber taper away from the microtoroid. Three regimes of coupling are obtained at various coupling distances: undercoupled, critical, and overcoupled. Undercoupling is achieved when the intrinsic loss rate of the microtoroid is greater than the coupling rate to the fiber taper and where the field in the taper is larger than the field coupling into the taper from the microtoroid. Critical coupling occurs with nearly lossless power transfer and is achieved when the cavity loss rate and the coupling rate into the taper are equal. On resonance, the field in the taper and the field coupled back into the taper differ in phase by $\pi$ which leads to destructive interference and the zero-transmission condition. The overcoupled regime occurs when the intrinsic loss rate is less than the coupling rate back into the fiber, and where the field in the taper is less than the field coupling into the taper from the microtoroid [5] [26].

### 2.2.5 Lowest mechanical modes of a microtoroidal resonator

The radially symmetric modes (2, 8, and 14 shown in Fig. 2.2) are most useful for cavity optomechanics. Modes 2 and 8 have displacement mostly in the z-direction and the mode that couples most strongly with the optical waveguide modes is a radial mode called the radial breathing mode (RBM). It has a frequency of about 75 MHz [28] [26].

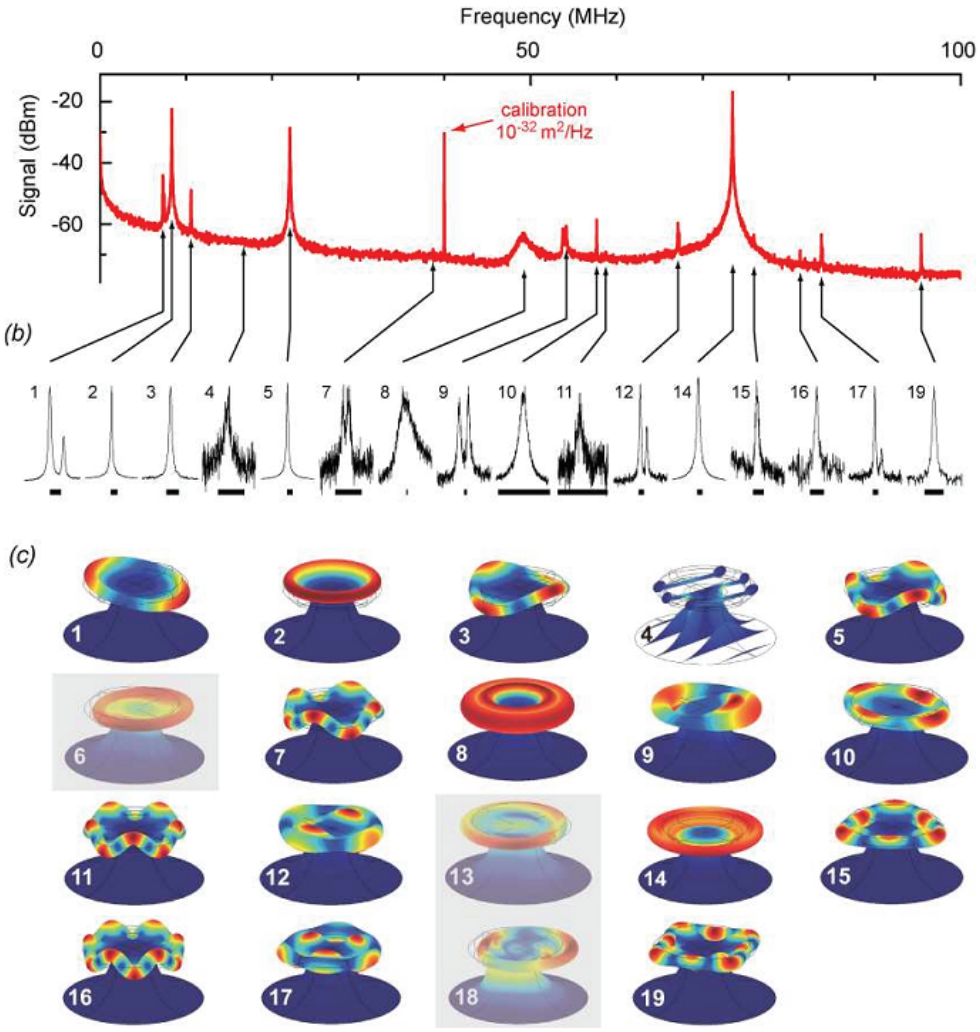


Figure 2.2: Displacement patterns of the 19 lowest frequency mechanical modes of a microtoroidal resonator. More description in text. From [28].

## 2.3 Brief description of cooling techniques

### 2.3.1 Doppler cooling

Doppler cooling is one mechanism that is used to cool hot atoms from the lithium atomic vapor source. The cooling laser light is detuned slightly below the energy required for a resonant transition in the atom. When cooling atoms using Doppler cooling, the photon momentum vector must point in the

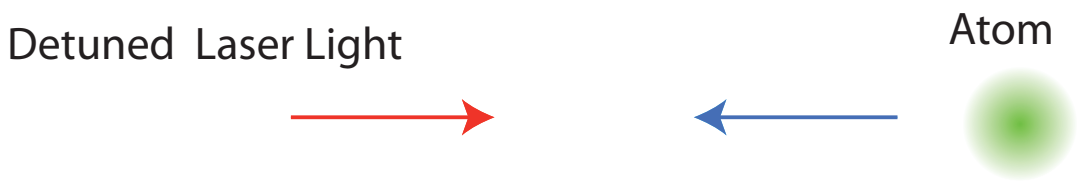


Figure 2.3: Illustration of Doppler cooling. Atoms move in the direction countering the red-detuned laser beam propagation. The detuned light is blue-shifted into resonance with the atomic transition through the Doppler shift.

opposite direction of the atom velocity vector. The light is red-detuned so that atoms moving toward the light source (in the opposite direction of propagation of the laser light wave vector) have a larger probability of absorbing a photon due to the Doppler shift. When an atom absorbs a photon it also absorbs the photon's momentum. After absorption of a photon, the atom spontaneously emits a photon corresponding to the transition wavelength. The momentum of the spontaneously emitted photon is in a random direction, causing a net momentum kick in the direction of the absorbed photon. After many absorption events the atom is cooled to the Doppler cooling limit, which in the two-level treatment, is the minimum temperature attainable through the Doppler cooling mechanism alone. The Doppler temperature limit is given by,

$$T_{Doppler} = \frac{\hbar\gamma}{2k_b}, \tag{2.8}$$

where $\gamma/(2\pi)$ is the natural linewidth of the cooling transition.

### 2.3.2 Polarization gradient (Sisyphus) cooling

Doppler cooled atoms can be cooled further down, to sub-Doppler temperatures, through a mechanism called Sisyphus cooling, also known as polarization gradient cooling. Sisyphus cooling is a result of the polarization gradient created by the standing wave of two counter-propagating laser beams having

orthogonal polarizations. In the case of a $\sigma^+ - \sigma^-$ standing wave, typically used in a MOT, the polarization of the combined field is linear and oriented in a helix around the optical axis. Similar to a particle caught in a harmonic trap, as the atoms move to the potential maximum of the standing wave, they lose kinetic energy to potential energy. Simultaneously, the AC Stark shift increasingly gives rise to energy shifts of the excited state called dressed states. The AC Stark shift is somewhat similar to a Zeeman shift. In Zeeman shifting, the degree of energy separation between the levels is a function of magnetic field, and in the case of the AC Stark shift, the degree of energy separation between the levels is a function of the intensity of the electromagnetic field. Therefore, dressed states have variable energy separation as a function of light intensity which functions as a confining mechanism. This causes the atom's transition wavelength to become increasingly resonant with the wavelength of the laser forming the standing wave as the atom moves to the potential maximum of the standing wave. When the atom's transition wavelength comes into resonance with the laser light, optical pumping moves them to a lower energy state causing them to lose the potential energy they had gained, lowering the atom's total energy. The final temperature of the atoms from polarization gradient cooling is related to the kinetic energy the atom gains through the absorption of one photon. Temperatures orders of magnitude below what is achievable by Doppler cooling can be reached using Sisyphus cooling, and the temperature limit of polarization gradient cooling is the called the recoil temperature. The recoil temperature is the temperature that the atom obtains by absorption of one photon,

$$T_{rec} = \frac{\hbar^2 k^2}{2mk_B} \tag{2.9}$$

where $m$ is the mass of the atom and $k$ is the wavenumber of the laser cooling transition.

Polarization gradient cooling can be effective when the linewidth of the cooling transition is small compared to the hyperfine splitting of the excited state or if there is a large degree of magnetic degeneracy in the ground state [32]. Polarization gradient cooling is efficient for most of the alkali metal atoms (Na, Rb, ad Cs) where MOTs of these typically attain temperatures of about 10 $\mu$K, which is very close to the recoil temperature, $T_{rec}$ [9]. For Li and K, which are often employed in Fermi-gas experiments, sub-Doppler cooling is ineffective in the presence of magnetic fields including those required for a MOT. In both the fermionic and bosonic isotopes of K however, sub-Doppler cooling has been attained by first cooling in a MOT and cooling further using optical molasses [13] [23], but at the expense of density in the case of fermionic K [23] [9]. For Li, sub-Doppler cooling by polarization gradient cooling is prohibited because the hyperfine splitting of the excited state is unresolved, therefore temperatures are limited to about 300 $\mu$K, roughly twice the Doppler limit [9].

### 2.3.3 Optical molasses

Optical molasses is formed using three counter-propagating circularly polarized laser beams. Optical molasses is based on polarization gradient cooling (Sisyphus cooling), and is contrasted with the Magneto-Optical trap (MOT) by the lack of a magnetic field. The optical molasses cooling technique can cool atoms further than a MOT by an order of magnitude.

## 2.4 Magnetic trapping of neutral alkali atoms

Alkali atoms have a sizable permanent magnetic dipole moment primarily arising from the single unpaired valence electron which allows them to be confined in a magnetic trap. The potential energy of a dipole in a magnetic field is,

$$U = -\bar{\mu} \cdot \bar{B} \tag{2.10}$$

where $\bar{\mu}$ is the magnetic dipole moment and $\bar{B}$ is the magnetic field vector. If $\bar{\mu} \parallel \bar{B}$, $U$ is a min when $\bar{B}$ is a maximum. If $\bar{\mu}$ anti-$\parallel$ $\bar{B}$, $U$ is a min when $\bar{B}$ is a minimum. According to Maxwell's equations in free space,

$$\bar{\bigtriangledown} \times \bar{B} = 0 \tag{2.11}$$

$$\bar{\bigtriangledown} \cdot \bar{B} = 0 \tag{2.12}$$

so,

$$\bigtriangledown^2 \bar{B} = 0 \tag{2.13}$$

and $\bar{B}$ satisfies Laplace's equation. (use identity $\bar{\bigtriangledown} \times \left(\bar{\bigtriangledown} \times \bar{B}\right) = \bar{\bigtriangledown}\left(\bar{\bigtriangledown} \cdot \bar{B}\right) - \bigtriangledown^2 B$) This implies,

$$\bigtriangledown^2 |\bar{B}| = \sqrt{\sum \frac{\partial^2}{\partial x_i^2} B_j^2} \tag{2.14}$$

where the sum is over both indices, j and i. The equation,

$$\bigtriangledown^2 |\bar{B}| = \sqrt{\sum \frac{\partial}{\partial x_i} \left(2 B_j \frac{\partial}{\partial x_i} B_j\right)} \tag{2.15}$$

$$= \sqrt{\sum \left[2 \left(\frac{\partial B_j}{\partial x_i}\right)^2 + 2 B_j \frac{\partial^2}{\partial x_i^2} B_j\right]} = \sqrt{\sum 2 \left(\frac{\partial B_j}{\partial x_i}\right)^2} \geq 0, \tag{2.16}$$

shows that there can be no local magnetic field maximum in magnitude, and trapping is limited to a magnetic field minima. Therefore, only dipole moments anti-parallel to the magnetic field are confined.

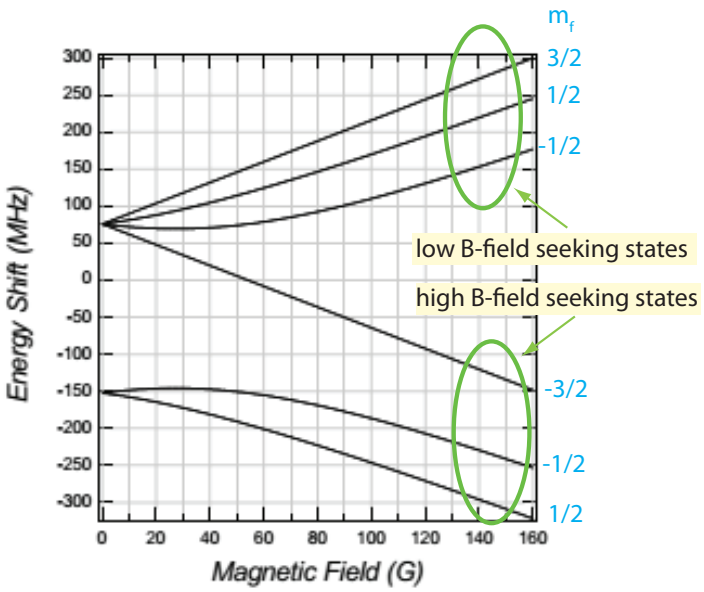


Figure 2.4: Zeeman shift of the $2^2S_{1/2}$ ground state of $^6$Li. Adapted from [11]. In free space, there is no allowed magnetic field maxima in magnitude, therefore magnetic trapping of lithium only confines the higher energy, low B-field seeking, hyperfine ground states.

The hyperfine structure of $^6$Li as a function of magnetic field is shown in Fig. 2.4 which shows that one can only trap higher energy states, as the lowest energy states are high B-field seeking.

At high fields $m_s$ and $m_f$ are good quantum numbers. The low B-field seeking states can be described by $|m_s = 1/2, m_f = 0, \pm 1\rangle$ (spin up), and the high B-field seeking states by $|m_s = -1/2, m_f = 0, \pm 1\rangle$ (spin down). The spin magnetic dipole moment is $\mu = -g\mu_B \bar{S}/\hbar$, where $g$ is the spin g-factor, $\mu_B$ is the Bohr magneton, and $\bar{S}$ is the spin. The energy for spin up (low B-field seeking) states is then given by $U = \mu B$, and for spin down states (high B-field seeking states), $U = -\mu B$. The low B-field seeking states are spin up ($m_s = 1/2$) and the high B-field seeking states are spin down ($m_s = -1/2$). The magnetic trapping potential is dependent on the spin state of the atom as shown in Fig. 2.5. $^6$Li atoms in a magnetic trap have a higher probability of being anti$\|$ $\bar{B}$ and occu-

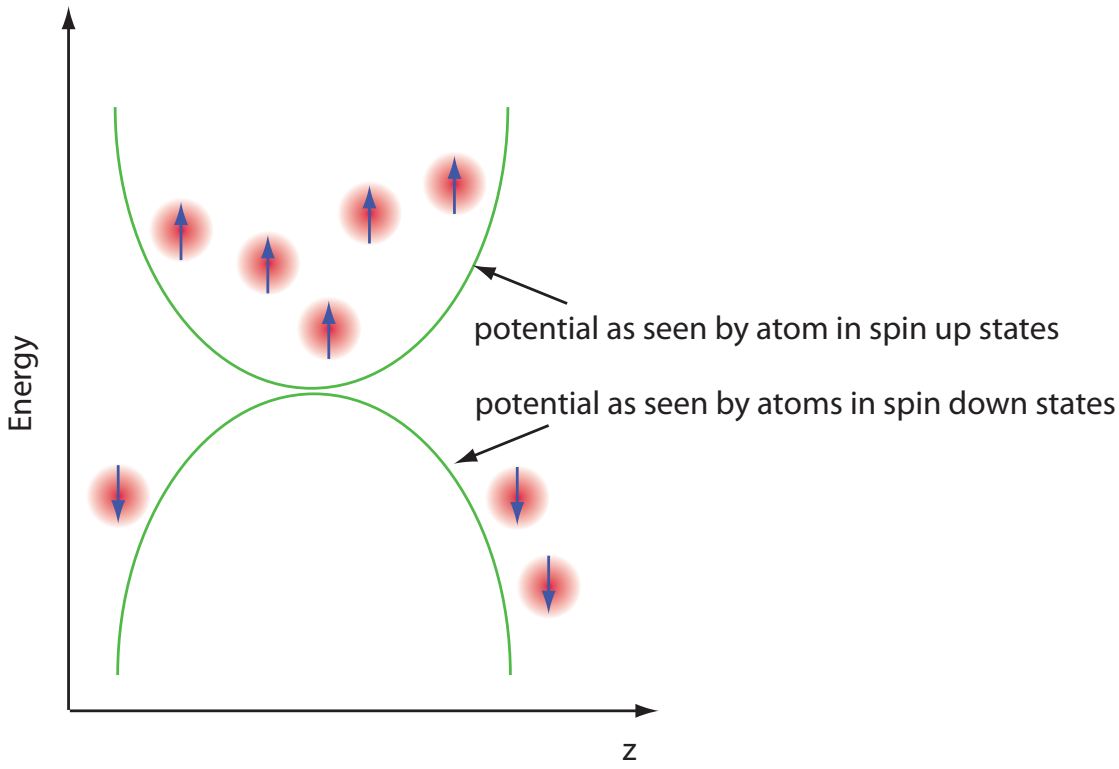


Figure 2.5: Magnetic trapping potential for atoms having opposite spins. Magnetic traps are subject to atom loss from spin-flip collisions.

pying low B-field seeking spin up ($m_s = +1/2$) states. Magnetic traps have this dependence on the internal state of the atom, and are subject to atom loss from spin-flip collisions. However, dipole traps can trap atoms independent of their ground state dynamics. Independence from internal state dynamics of the atom is useful for experiments that rely on interactions between fermions in different states [24].

## 2.5 Ultracold atoms in a magneto-optical trap

A 3D magneto-optical trap can be formed using three counter-propagating circularly polarized laser beams and a magnetic field gradient to trap the atoms. A 3D MOT is formed using 3 counter-propagating beams where atoms move

in three dimensions, a 2D MOT is formed using 2 counter-propagating beams where atoms move in two dimensions, and a 1D MOT with 1 counter-propagating beam where atoms are confined to move in one dimension. In our 3D MOT, the lithium atoms are initially Doppler cooled by the three counter-propagating laser beams and confined in the magneto-optical trap. The combination of the viscous damping force and the spatial restoring force allows the lithium atoms to be cooled directly from the lithium dispensers.

Radiation pressure arises from the absorption of a resonant photon and followed by spontaneous emission. This causes a force on the atom in the direction of propagation of the laser,

$$\bar{F}_{rad} = R_{sc}\hbar\bar{k}. \tag{2.17}$$

An alkali atom in circularly polarized light can be approximated by a two-level system. The scattering rate is given by,

$$R_{sc} = \frac{\Gamma}{2}\frac{\frac{I}{I_{sat}}}{1 + \frac{I}{I_{sat}} + \frac{4(\Delta - kv)^2}{\Gamma^2}} \tag{2.18}$$

$$\frac{I}{I_{sat}} = \frac{2\Omega^2}{\Gamma^2} \tag{2.19}$$

$$I_{sat} = \frac{c\pi h\Gamma}{3\lambda^3} \tag{2.20}$$

where $\Delta = \omega - \omega_0$. The $kv$ term accounts for the Doppler shift so that an atom moving toward the laser beam has a negative velocity and the scattering rate is maximized for red detunings, $\omega < \omega_0$. If the atom is moving away from the laser, the scattering rate is maximized for $\omega > \omega_0$. For red laser detunings, this radiation force is called a *viscous damping force*.

For high laser powers, the scattering rate $R_{sc} = \frac{\Gamma}{2}$ so the radiation force is $\bar{F}_{rad} = \frac{\Gamma}{2}\hbar\bar{k}$. One can find the acceleration of the atom by equating the radiation force to $ma$ where $m$ is the mass of the atom obtaining $a = \frac{\bar{F}_{rad}}{m}$. By using the values in Table 2.1 for the saturation intensity and the lifetime of the transition

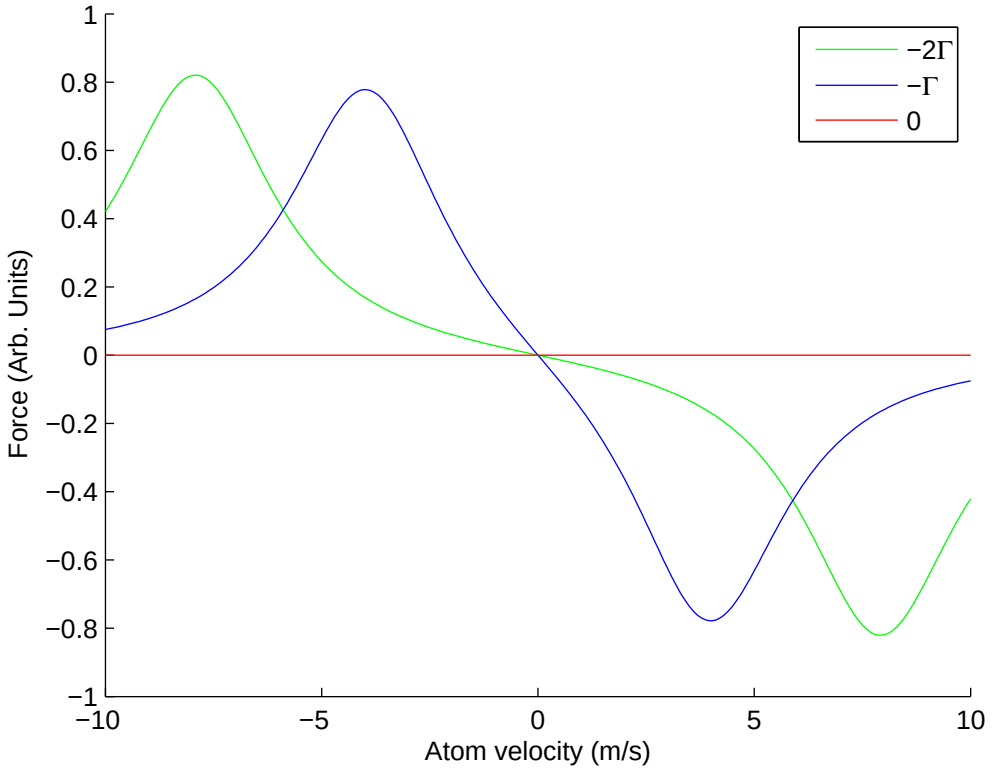


Figure 2.6: Net radiation pressure force as a function of atom velocity and detuning with two red-detuned counter-propagating beams, Eqn. 2.21.

$\Gamma^{-1}$ one finds that the acceleration of the atom by the radiation force is huge, about $10^5$ g's.

At low laser intensities, the radiation forces from the counter-propagating beams act independently,

$$F_{tot} = \hbar k \frac{\Gamma}{2} \left[ \frac{\frac{I}{I_{sat}}}{1 + \frac{I}{I_{sat}} + \frac{4(\Delta - kv)^2}{\Gamma^2}} - \frac{\frac{I}{I_{sat}}}{1 + \frac{I}{I_{sat}} + \frac{4(\Delta + kv)^2}{\Gamma^2}} \right]. \tag{2.21}$$

The sum of the forces is shown in Fig. 2.6.

When the lithium atom is optically excited, it spontaneously decays into one of the two hyperfine ground states. Because only one of the ground state hyperfine levels is resonant with the cooling light, atoms that spontaneously decay into the other hyperfine state cannot be excited. This state is called a *dark state*.

Therefore, we include another wavelength of light into the trap along with the cooling light called repump light. Repump light is resonant with this transition and pumps the atoms out of the lowest ground state causing this state to no longer be dark. Repump light pumps the atoms that spontaneously decays into that state into the excited state so that it may have probability to decay to the hyperfine ground state that is resonant with the cooling light. This process using cooling and repump light, or a cooling cycle with no dark states, is called a *complete cooling cycle*.

Two anti-Helmholtz coils on the z-axis of the MOT create a spatially varying magnetic quadrapole field has a magnetic zero at the center of the trap. As the atoms move away from the center of the trap, they see an increasing magnetic field which increasingly shifts the energy of the magnetic sublevels by the Zeeman shift. The magnetic field is negative on one side of the zero and positive on the other, the magnetic field sublevel Zeeman splittings are antisymmetric about the magnetic field zero, therefore we use $\sigma^+ - \sigma^-$ circularly polarized counter-propagating beams. See a simple example in Fig. 2.7. The magnetic field on the z-axis from anti-Helmholtz coils is,

$$B = \frac{\mu_0 n I R^2}{2}\left[\frac{1}{(R^2+(z-d/2)^2)^{3/2}} - \frac{1}{(R^2+(z+d/2)^2)^{3/2}}\right]; \tag{2.22}$$

and the sign of magnetic field is negative at negative values of z. This is plotted on the left in Fig. 2.7. The magnetic sublevels increasingly Zeeman shifts the magnetic sublevels antisymmetrically about the center of the magnetic trap as a function of magnetic field strength and sign. $\sigma^+$ light can only make $\Delta m = +1$ transitions and $\sigma^-$ can only make $\Delta m = -1$ transitions. Therefore, as the atom moves to the right, the $\sigma^-$ red detuned light propagating toward the left will have a higher probability of absorption than the $\sigma^+$ light. As the atom moves to the left, the $\sigma^+$ red detuned light propagating toward the right will have a

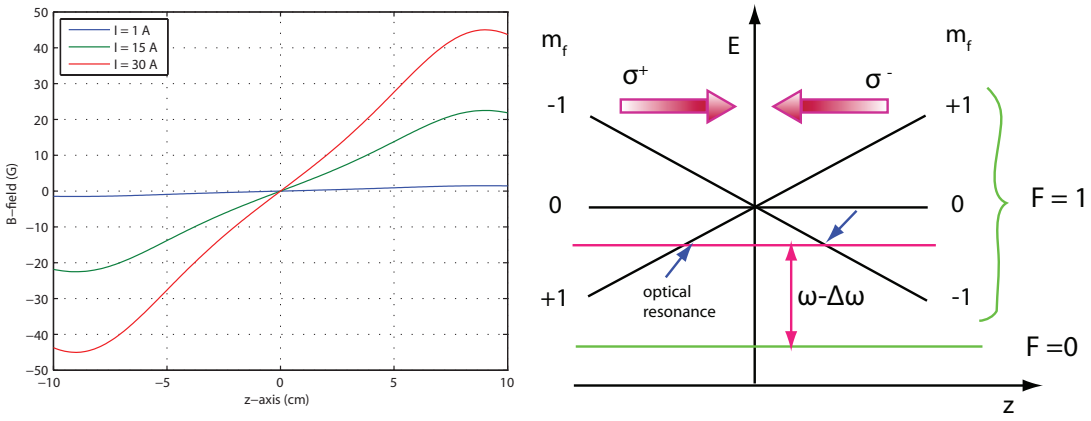


Figure 2.7: Example of spatial restoring force in 1D

greater probability of absorption than the $\sigma^-$ light. This leads to a net force toward the center of the trap called a *spatial restoring force*.

Because the light is detuned, the probability of photon absorption increases with the Zeeman shift. As the atom becomes resonant with the wavelength of the cooling light, it absorbs a photon from the cooling beam and experiences a net momentum kick back toward the center of the trap.

The magnetic field gradient is proportional to the current running through the anti-Helmholtz coils. As the magnetic gradient increases the Zeeman shift is greater for smaller displacements. Therefore, increasing the current running through the anti-Helmholtz coils more tightly confines the atoms and, given the same atom number, increases the density of the atom cloud in the MOT.

The loading rate is the number of atoms loaded into the trap as a function of time, and increases as,

$$\dot{N} = R_{load} - R_{loss}N \tag{2.23}$$

where $R_{loss}$ is the loss rate due to collisions with background atomic gas or impurities in the vacuum chamber. Some mechanisms limiting the max density attainable in a MOT are the reduction of the inward radiation force through

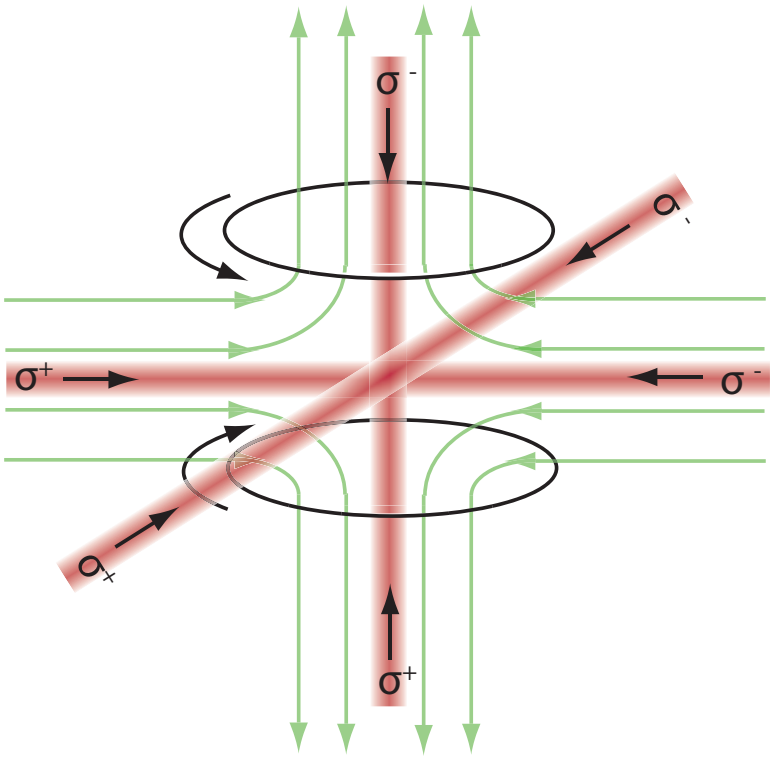


Figure 2.8: Magneto-optical trap

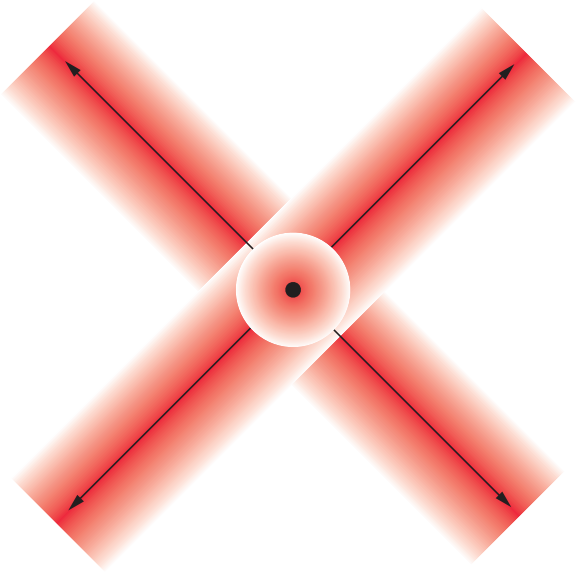

Figure 2.9: Three counter-propagating laser beams in x,y, and z form the optical trap for our magneto-optical trap.

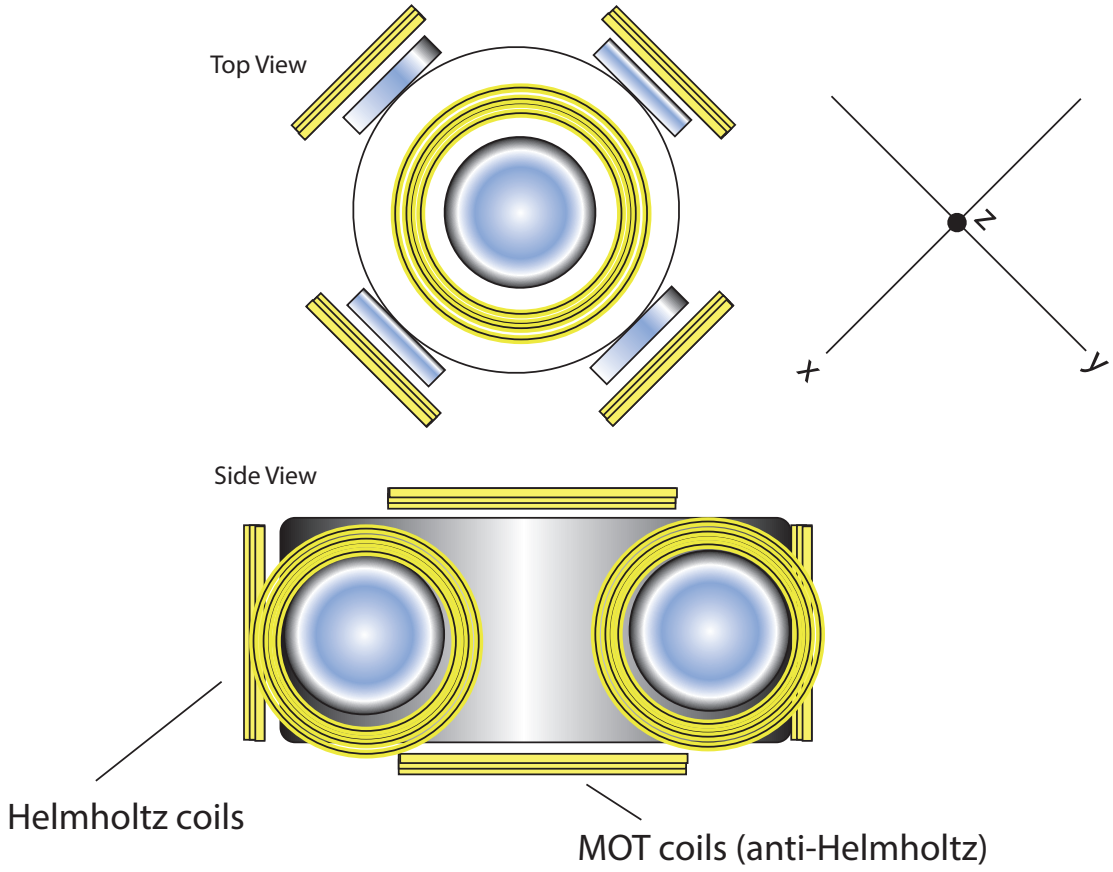


Figure 2.10: Diagram of the lithium magneto-optical trap. The laser beams counter-propagate in the direction x, y, and z as shown in Fig. 2.9

photon absorption by the atoms, and the outward radiation force from the spontaneous emission of photons by the atoms.

### 2.5.1 Phase space density

The phase space density of trapped atoms in a MOT can be calculated using the temperature, T, of the atoms and the density of atoms in the trap $n$. The phase space density is defined by,

$$n\lambda_{dB}^3 = \rho = n\left(\frac{h}{\sqrt{2\pi m k_B T}}\right)^3 \tag{2.24}$$

where $\lambda_{dB}$ is the de Broglie wavelength. The condition for degeneracy is $\rho > 1$.

## 2.6 Ultracold atoms in optical potentials

### 2.6.1 Optical dipole potential

Optical dipole trapping of neutral atoms was first suggested by [1] and first demonstrated experimentally by [7]. The internal ground states of the atoms see nearly identical potentials in an optical dipole trap, which facilitates long coherence lifetimes important for cavity QED and quantum computing applications. Dipole traps pose less restrictions on the internal conditions of the atoms for confinement, as opposed to magnetic traps for example, which rely on the spin magnetic dipole moment of the atom for confinement. Optical dipole traps provide a wide variety of ways to manipulate the atoms. For example, by steering a focused laser beam, cold atoms can be moved around inside of the vacuum chamber and near to surfaces, such as near to the surface of our silicon microtoroid. If the atoms are brought near to the surface of the microtoroid via a 3D dipole trap formed by a focused laser beam, one may be able to adiabatically load the atoms into the evanescent wave dipole trap of the silicon microtoroid.

A light field can interact with atoms both dissipatively and conservatively. Atomic absorption and spontaneous emission of a photon in the light field is a dissipative interaction. Atomic interaction with the light field through dipole interactions is conservative. Optical dipole traps rely on conservative electric dipole interactions using far-detuned light. The result of this interaction is called the optical dipole force and it is the confining mechanism in a dipole trap. Dipole interactions are relatively weak, and typical trap depths range below 1 mK. Because this is a conservative light-atom interaction, light scattering is low and therefore the temperature of the atoms in a dipole trap is not limited by light scattering as is the case in a MOT, optical molasses, or an optical lattice.

If the detuning of the dipole trap from resonance is larger than the fine structure splitting of the excited state ($2^2P_{1/2}$ - $2^2P_{3/2}$ about 10 GHz for $^6$Li and $^7$Li in Fig. 2.18) the transition can be approximated to occur between angular momentum states L=0 and L=1. In this limit of large detunings and linearly polarized light, which can only make m=0 transitions, the dipole force is independent of the particular ground-state dynamics. This allows for trapping of atoms having different spin states and many dipole trap geometries. The interaction potential formed by a classical electric field interacting with an atom is given by [14],

$$U_{dip} = -\frac{\bar{d}\cdot\bar{E}}{2} = -\frac{\mathrm{Re}[\alpha(\omega)]}{2\epsilon_0 c} I \tag{2.25}$$

where $I$ is the light intensity,

$$I = \frac{\epsilon_0 c|E|^2}{2} \tag{2.26}$$

and $\alpha(\omega)$ is the complex frequency-dependent polarizability. Note that the polarizability of the excited state is different than the ground state, and so the atoms are subject to dipole force fluctuations. The dipole force is the negative gradient of the interaction potential, and it is a conservative force [14],

$$F_{dip} = -\bigtriangledown U_{dip}. \tag{2.27}$$

By treating atom as a two-level quantum system interacting with a classical electromagnetic field, the polarizability is calculated by integrating the equation of motion for an electron subject to oscillatory drive. Saturation effects are also neglected, and using the dipole matrix element between the ground and excited state to calculate the damping rate (as opposed to using Larmor's formula) gives,

$$U_{dip}(r) = -\frac{3\pi c^2}{2\omega_0^3}\left[\frac{\Gamma}{\omega_0-\omega}+\frac{\Gamma}{\omega_0+\omega}\right] I(r) \tag{2.28}$$

with the damping rate given by,

$$\Gamma = \frac{\omega_0^3}{3\pi\epsilon_0\hbar c^3}|\left\langle e\right|\mu\left|g\right\rangle|^2. \tag{2.29}$$

From this one can see that for red-detuning the potential is at a minimum at the intensity maxima, and for a blue-detuning, the potential is at a minimum where the intensity is a minimum. Another way to look at this is that the detuning changes the sign of the polarizability such that for positive (negative) polarizability, the atoms oscillate in (out) phase with the electric field are are confined to (repelled from) regions of high intensity. For large detunings this equation simplifies to,

$$U_{dip}(r) = \frac{3\pi c^2}{2\omega_0^3}\frac{\Gamma}{\Delta}I(r) \tag{2.30}$$

where $\Delta = \omega - \omega_0$. The relation between the scattering rate and the dipole potential is,

$$\hbar\Gamma_{sc} = \frac{\Gamma}{\Delta}U_{dip}. \tag{2.31}$$

The dipole potential scales as $I/\Delta$ and the scattering rate as $I/\Delta^2$ so a high intensity and large detunings are used to keep the scattering rate low [14]. Note that the scattering rate is independent of the sign of the detuning. Although the atoms are confined at intensity minima for the blue-detuned dipole traps, the scattering rate is exactly the same for the equivalent magnitude of detuning in a red-detuned trap, where the atoms are confined at the light intensity maxima. From these equations, one can also see that fluctuations in the intensity and position of the lasers creating the trap can cause heating of atoms in the dipole trap.

### 2.6.2 Two-color dipole trap near a dielectric surface

For our hybrid atom-optomechanics experiment, we confine atoms near the surface of the microtoroid in a two-color dipole trap. In a two-color dipole trap, the

dipole interaction potentials add,

$$U_{tot} = U_{\lambda_1} + U_{\lambda_2}. \tag{2.32}$$

Hybrid optomechanical coupling to the microtoroid requires a two-color evanescent wave dipole trap where the blue detuning causes a repulsive potential and the red detuning causes an attractive potential.

Because the atoms must be trapped near the surface of the dielectric, the van der Waals potential must be compensated by the dipole interaction potential formed by the blue-detuned light [19]. The Casimir-Polder interaction (due to quantum fluctuations, and taking the finite speed of light into account and so can be viewed as a retarded van der Waals force [22]) is negligible in the dipole trap region [16]. The total potential now becomes,

$$U_{tot} = U_{\lambda_1} + U_{\lambda_2} + U_{\text{van der Waals}} \tag{2.33}$$

Assuming the surface to be an infinite dielectric, the simplest model for the interaction of a ground state atom and a wall of dielectric constant $\epsilon$ gives the Lennard-Jones potential [21],

$$U_{\text{van der Waals}} = -\frac{\left\langle d_{||}^2 \right\rangle + 2\left\langle d_{\perp}^2 \right\rangle}{64\pi\epsilon_0}\frac{\epsilon-1}{\epsilon+1}\frac{1}{y^3} = -\frac{C^{(3)}}{y^3}\frac{\epsilon-1}{\epsilon+1} \tag{2.34}$$

where $\epsilon$ is the dielectric permittivity, $y$ is the distance from the waveguide surface, and $C^{(3)}$ is the van der Waals dispersion coefficient [3] determined from $\left\langle d_{\parallel}^2 \right\rangle$ and $\left\langle d_{\perp}^2 \right\rangle$ which are the expectation values of the squared dipole parallel and perpendicular to the surface. The dipole matrix element $\bar{d}$ for a two-level system interacting with classical radiation $\langle e_2|\,\bar{r}\,|e_1\rangle = \langle e_1|\,\bar{r}\,|e_2\rangle$ is given by the light-matter interaction coupling constant, $\hbar\Omega_{\text{Rabi}} = qE_o\bar{d}.\hat{n}$, where $\Omega_{\text{Rabi}}$ is the Rabi frequency of the transition.

### 2.6.3 Optical lattice potential

Ultracold atoms in lattice potentials allow for the investigation of many questions in condensed matter physics. An optical lattice is formed by counter-propagating beams which interfere to form a standing wave and periodic intensity pattern. Atoms in the lattice experience an AC Stark shift that varies with the intensity resulting in confinement within the regions of lowest potential. Also, atoms in a standing wave are cooled by the Doppler effect. For example, consider an atom in a slightly red-detuned standing wave. A freely moving atom will experience a stronger radiation pressure from the counter-propagating wave than the co-propagating wave through the Doppler effect. Further cooling of the atoms in the lattice can be achieved by adjusting lattice parameters. Adiabatic expansion of the lattice and evaporative cooling by decreasing the intensity of the beams is one example. The periodicity of the lattice also affects the energy level structure of the lattice. Lattice periodicity can be changed through changing the laser wavelength (using AOMs, for example) or the angle at which the counter-propagating beams intersect. The atoms confined in the lattice can then be cooled to the ground state through Raman sideband cooling.

In a one-dimensional lattice the potential due to the standing wave can be written as,

$$U_{\text{lattice}}(x) = U_o \sin^2(kx). \tag{2.35}$$

Now the Schrödinger equation for a particle in this potential can be written as,

$$\left[\frac{\hat{p}^2}{2m} + U_0 \sin^2(kx)\right] \psi(x) = E\psi. \tag{2.36}$$

The lattice potential is periodic, and the wave function for the particle repeats over the lattice, analogous to an electron in a crystal. According to Bloch's theorem the state for the system can be written as the product of a plane wave and

a periodic function which has the same periodicity as the potential,

$$\psi(x) = e^{ikx}\phi(x) \tag{2.37}$$

where the energy eigenvalues are

$$\epsilon_n(k) = \epsilon_n(k + k') \tag{2.38}$$

The energy values vary continuously vary with $k$ and $n$ denotes the energy band index.

### 2.6.4 Bragg scattering of atoms in an optical lattice

One way to determine the average density of atoms in the lattice is using the Bragg reflection of a far-off resonant probe beam. The lattice field forms a stable potential, trapping the atoms at periodic positions with the separation distance between lattice site determined by the lattice parameter, $\lambda/2$. There are two differences between Bragg scattering in lattices as opposed to Bragg scattering in crystals: the distance between lattice sites is on the order of $\mu$m allowing for Bragg scattering at optical wavelengths (instead of in the x-ray range for crystals). Therefore, through Bragg scattering, one can use a weak optical probe beam at various detunings to determine the average atomic density.

The Bragg reflection intensity is a function of probe detuning and atomic density. At low densities the lineshape is Lorentzian with the natural linewidth, and at larger atomic densities, the lineshape is broadened, and eventually develops a dip at the the atomic resonance [2].

Atoms in a lattice with reciprocal lattice vectors $\bar{K}$ (i.e. $2\pi n/a$ for 1D and lattice spacing $a$) and a probe with wave vector $\bar{k}$ will reflect the probe in the direction $\bar{k} + \bar{K}$ (this is similar to the discussion on AOMs in Section 3.4) when

the Bragg condition is satisfied (from $n\lambda = 2d\sin\theta$ or simply $2k \cdot K = -K^2$). Bragg reflection coefficient is given by [17],

$$R_n = n^2 R f_n(\theta_p, \Delta_p) \tag{2.39}$$

where $f_n(\theta_p, \Delta_p)$ accounts for loss and dispersion and,

$$n^2 R\, \beta N^2 \sigma(\Delta_p)^2 \tag{2.40}$$

where $N$ is the number of atoms per volume, $\sigma(\Delta_p)$ is the absorption cross section, and $\Delta_p$ is the probe detuning. The temperature of the atoms in the lattice can also be determined by the center-of-mass distribution through the time dependent Debye-Waller factor after the lattice light is turned off. The Debye-Waller factor is given by,

$$\beta = e^{-(2\pi\Delta x/d)^2} \tag{2.41}$$

where $d$ is the lattice separation and $\Delta x$ is the RMS width of the atomic center of mass perpendicular to the lattice planes [17].

## 2.7 Raman sideband cooling

Raman sideband cooling is a cooling technique used when atoms are in an optical lattice potential. At sufficient lattice depths, the lattice can be modeled as a harmonic trap. Atoms in the lattice are subjected to a magnetic field which leads to a Zeeman shift of the magnetic sublevels. The energy splitting of the magnetic sublevels and the energy level separation in the harmonic trap must be equal. Raman transitions allow atoms in a high vibrational energy state to move to a lower energy state in a different magnetic sublevel, shown in Fig. 2.11. Atoms in this new magnetic sublevel are optically pumped into the excited state

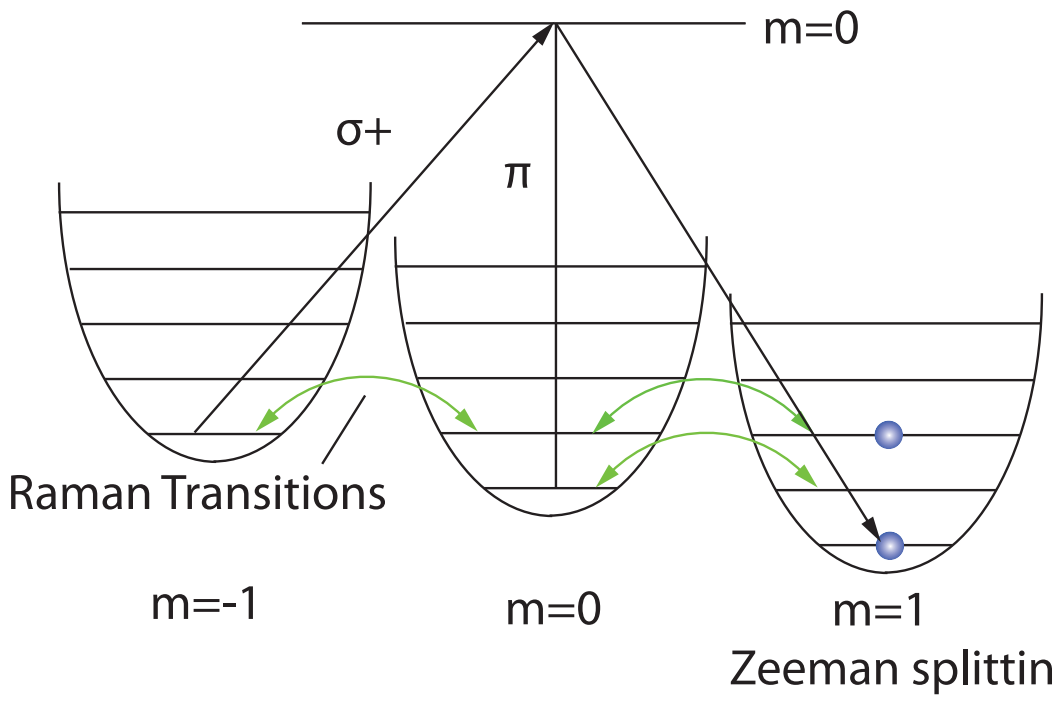


Figure 2.11: Example of Raman Sideband cooling using three m sublevels. $\pi$ light (having zero net angular momentum) pumps the m=0 state to the upper state.

with a photon of appropriate angular momentum for an allowed atomic transition. In the example of Fig. 2.11, an electron in the m=-1 state can absorb a photon having +1 angular momentum. This absorption excites the electron into the m=0 excited state. The electron naturally decays from this excited state into one of the ground state magnetic sublevels. The atom will maintain the same vibrational state upon decay, but depending on which magnetic sublevel it decays into, it will overall remain the same or have lower energy. There are no allowed optical pumping or Raman transitions in the dark state, the m=1 state in example of Fig. 2.11, therefore the atoms remain in this coldest state and are effectively cooled.

## 2.8 Evaporative cooling

Evaporative cooling of fermionic atoms in their ground state is a means for obtaining a dilute degenerate Fermi gas. Evaporative cooling is achieved by trapping the atoms in a dipole potential at high detunings, and adiabatically reducing the height of the potential trapping the atoms. This forces truncation of atoms having higher kinetic energies, shown in Fig. 2.12. After the truncation of atoms having higher kinetic energies the atoms thermalize to a lower average temperature, shown in Fig. 2.12. The key to evaporative cooling is rethermalization by elastic collisions so that the gas obtain a lower average temperature. Fermions are subject to the Pauli exclusion principle, which means that two fermions in the same state cannot occupy the same region of space. The Pauli exclusion principle prevents collisions between fermions having the same quantum state, and these collisions are required for rethermalization during evaporative cooling. There are a few ways around this. One way is to introduce a second, bosonic species where the bosons provide the necessary thermal conductivity between fermions. Or secondly, the fermionic gas can be forced into two different quantum states, giving an antisymmetric spin wave function which symmetrizes the spatial wave function giving rise to allowed atomic collisions [8].

In a degenerate gas of fermionic atoms, where the average temperature of the atom cloud is less than the Fermi temperature, $T < T_F$, the light scattering properties of the gas are different. In a degenerate Fermi gas, the Fermi sea is filled, inhibiting spontaneous emission. When a $^6$Li atom absorbs a photon, the atom occupies a momentum state above the Fermi level. Then when the atom emits a photon, there is a limited number of momentum states it can occupy because the filled Fermi sea reduces available recoil momentum phase space.

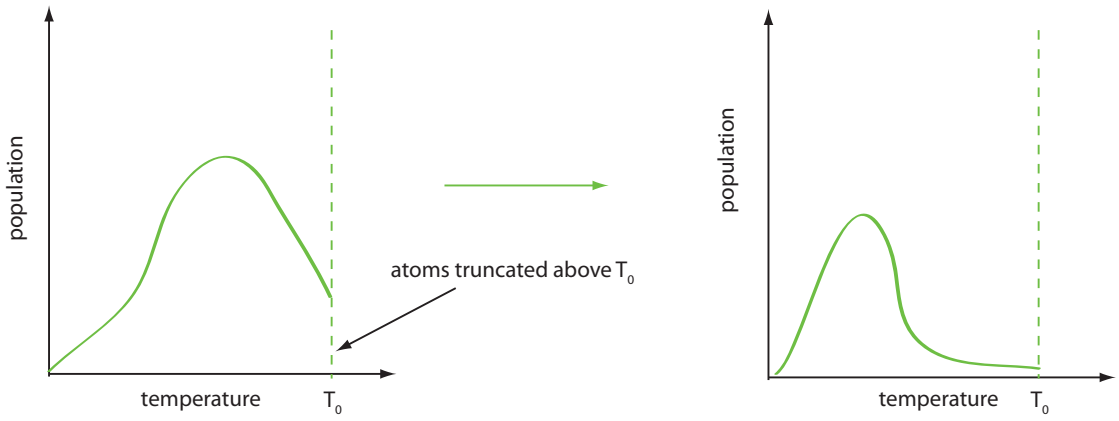


Figure 2.12: Truncation and rethermalization during evaporative cooling of trapped atoms. The high energy atoms are removed from the trap by adiabatically lowering the walls of the potential, followed by rethermalization of the gas to a lower average temperature.

This effect is similar to spontaneous emission enhancement and inhibition when an atom is embedded in a cavity [4]. The change in light scattering properties might be a way to probe a non-interacting Fermi gas for degeneracy.

### 2.8.1 Fermi temperature as a function of trap frequency

To achieve a degenerate Fermi gas, the atom temperature must be below the Fermi temperature. The Fermi temperature is found by through the number of atoms and integrating over the density of states up to the Fermi energy.

$$N = \int_0^{E_F} D(\epsilon) d\epsilon \tag{2.42}$$

The energy of the trap goes as $\epsilon_n = n\hbar\omega$. The energy levels give the coordinates on the surface of the sphere only in the first octant ($\{n_x, n_y, n_z\} \geq 0$). The energies can be thought of as continuous in energy space, and $n$ can be taken as a radius so that $n = \epsilon/\hbar\omega$ and $dn = d\epsilon/\hbar\omega$.

$$dn_x dn_y dn_z = n^2 \sin\theta dn d\theta d\phi \rightarrow \left(\frac{1}{8}\right) 4\pi n^2 dn \tag{2.43}$$

$$D(\epsilon) = \frac{\epsilon^2}{2\hbar^3\omega_x\omega_y\omega_z} \tag{2.44}$$

for an anisotropic trap (which is the case for a focused laser beam). Assuming the trap frequencies are the same in all three dimensions,

$$N = \int_0^{E_F} \frac{\epsilon^2 d\epsilon}{2\hbar^3\omega^3} = \frac{E_F^3}{6(\hbar\omega)^3} \tag{2.45}$$

$$E_F = \hbar\omega(6N)^{1/3} \tag{2.46}$$

The gas is degenerate if the temperature is below the Fermi temperature which is a function of atom number and trap frequency,

$$E_F = k_B T_F \tag{2.47}$$

$$T_F = \frac{\hbar\omega}{k_B}(6N)^{1/3}. \tag{2.48}$$

## 2.9 Saturated absorption spectroscopy for laser frequency locking

We often want to lock our lasers to resonant atomic transitions. Because a gas of atoms at a given temperature is subject to a velocity distribution, the emission spectrum is plagued by Doppler broadening of the linewidth. Saturated absorption spectroscopy is one technique that gives a Doppler-free signal. The setup the lithium-6 lab is using is shown in Fig. 2.13. The master laser which freely operates at a wavelength near 671 nm is launched into free space and split into two beams through two waveplates and a polarizing beam splitter. Waveplates allow us to control the polarization of the master laser to obtain various power ratios of the two output beams of the polarization-dependent (polarizing) beam splitter (PBS). The pump beam is a higher intensity beam which pumps the atoms in the lithium vapor cell into their excited state. A magnetic

field is present in the vapor cell which provides a Zeeman shift of the magnetic sublevels. A lower-intensity probe beam propagates through the lithium vapor cell in the opposite direction of the pump. The atoms are pumped into their excited state by the strong pump beam, and when the atom simultaneously sees a pump and probe beam of equal frequency as the pump, the probe beam photon cannot be absorbed by the atom.

The hot atoms in the vapor cell contain a distribution of velocities called a Doppler profile. To understand how saturated absorption spectroscopy allows for a Doppler-free signal, we first define positive velocity as moving toward the pump beam and negative velocity as moving toward the probe beam, shown in Fig. 2.14. The pump and the probe beams both originate from the master laser, and so they both have the same frequency. With respect to the probe light, atoms traveling toward the probe will see blue Doppler-shifted light and atoms traveling in the opposite direction toward the pump will see red Doppler-shifted light. The absorption process is shown as a function of laser (pump and probe) frequency in Fig. 2.15.

Recall that the magnetic field present in the vapor cell. The magnetic field induces a Zeeman shift and provides resolution of the hyperfine structure, $|1\rangle$ and $|2\rangle$ in the ground state. Hyperfine splittings of the excited state are small and therefore unresolved with respect to the ground state (refer to Fig. 2.18). The saturated absorption process begins in step 1. We begin with a sufficiently low laser frequency which cannot excite stationary, zero velocity, atoms from level $|2\rangle$ or $|1\rangle$ to the excited state. However, atoms with negative velocity, traveling toward the probe beam, will see blue Doppler-shifted light. Blue Doppler-shifted light appears from the atom's perspective to have an adequate energy for excitation to the excited state. The $|2\rangle$ level requires a lower energy for ex-

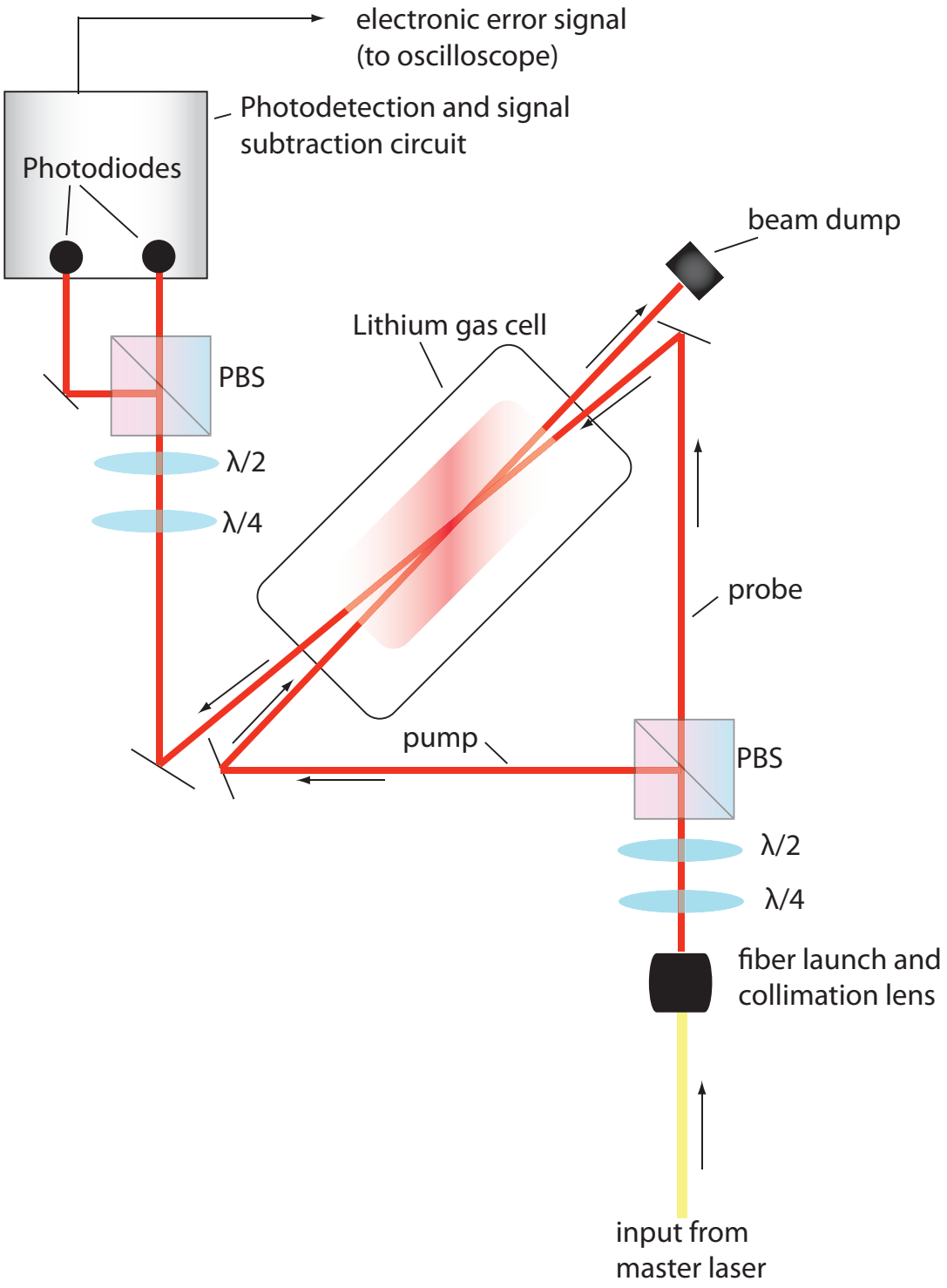


Figure 2.13: Setup used for saturated absorption spectroscopy

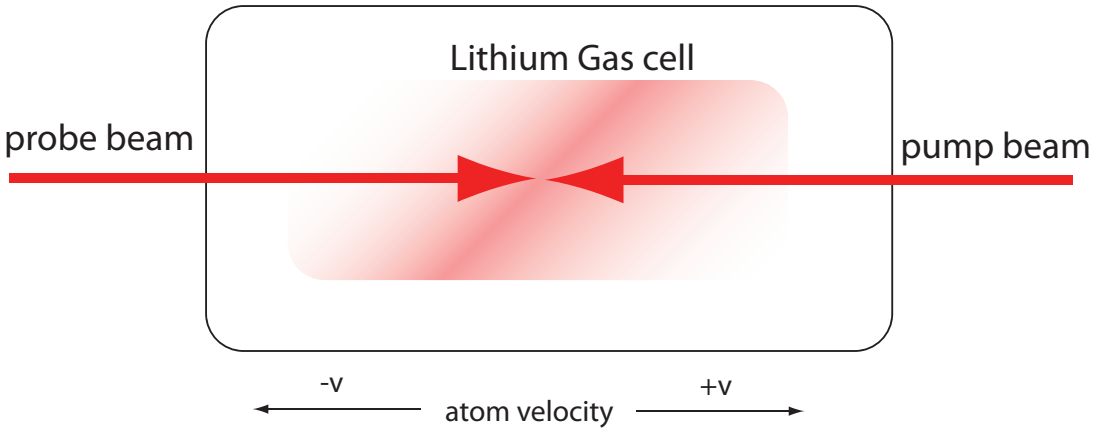


Figure 2.14: Pump and probe in lithium vapor cell. Atoms traveling toward the probe are defined to have a negative velocity and atoms traveling toward the pump are defined to have positive velocity.

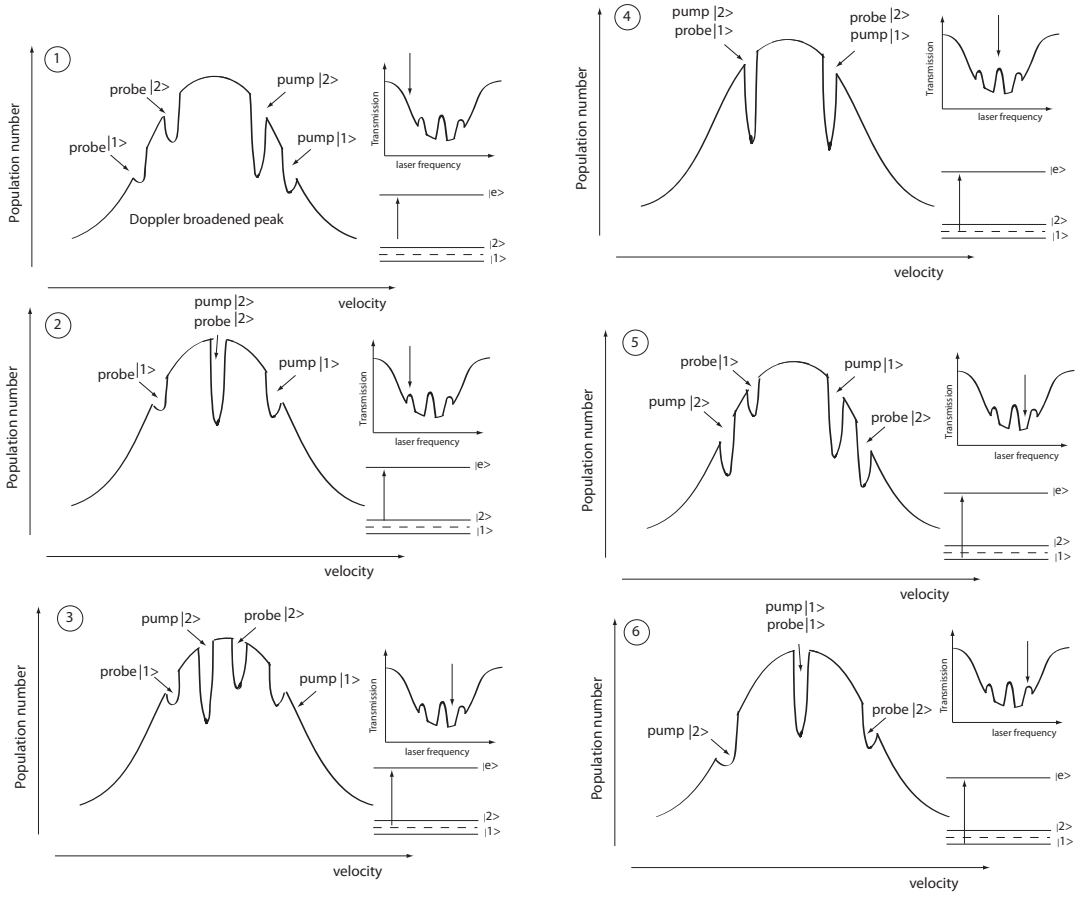


Figure 2.15: Saturated absorption as a function of pump and probe frequency (steps 1-6) Step 4 shows the crossover location.

citation to the excited state than the $|1\rangle$ level. Therefore, atoms traveling at low speeds will be excited from the $|2\rangle$ level and atoms traveling at higher speeds will be excited from the $|1\rangle$ state. As the master laser frequency increases, absorption of the pump becomes overlapped with the probe, shown in step 2. The pump and probe beams are traveling in opposite directions, and therefore we know that atoms in the zero velocity class will be excited. When the pump excites atoms that would normally absorb photons from the probe, the probe is not absorbed and the probe beam will be transmitted and detected on the photodiodes. As we sweep the pump and probe frequency from low to high, the first transmission point of the probe corresponds to $|2\rangle$. As the frequency of the pump and probe increases, the pump and probe frequencies do not overlap in any atomic velocity class giving rise to probe attenuation, shown in step 3. But during step 4, atoms traveling in the negative velocity direction (toward the probe) will see blue-shifted probe light that excites the $|1\rangle$. Those same atoms will see the exact same magnitude of Doppler shift of the pump light but in the opposite direction, giving rise to red-shifted pump light that excites the $|2\rangle$ level. For this particular velocity class of atoms, the pump light is red-shifted by exactly the same amount that the probe light is blue-shifted. This corresponds to an overlap of the pump and probe for those atoms and transmission of the probe. Similarly, this happens for atoms of the same speed but traveling in the positive direction. These atoms will be excited from $|1\rangle$ by the blue-shifted pump light and from $|2\rangle$ by the red-shifted probe light. This case occurs only when the Doppler shift of the atoms corresponds to exactly half of the energy between levels $|1\rangle$ and $|2\rangle$. This is called the crossover, and we lock our lasers to the crossover location which can easily be identified as it is located between the two other error signals.

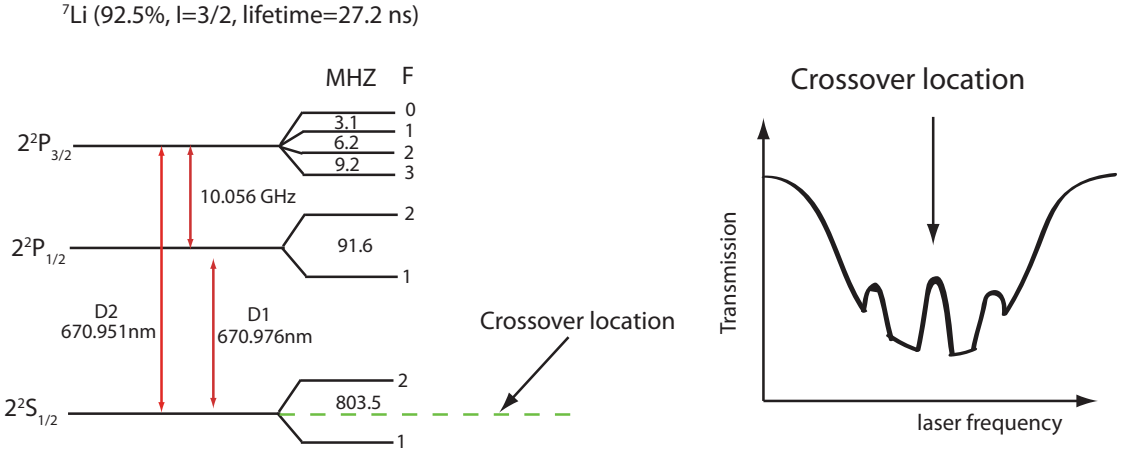


Figure 2.16: Lithium energy level diagram corresponding to the crossover location

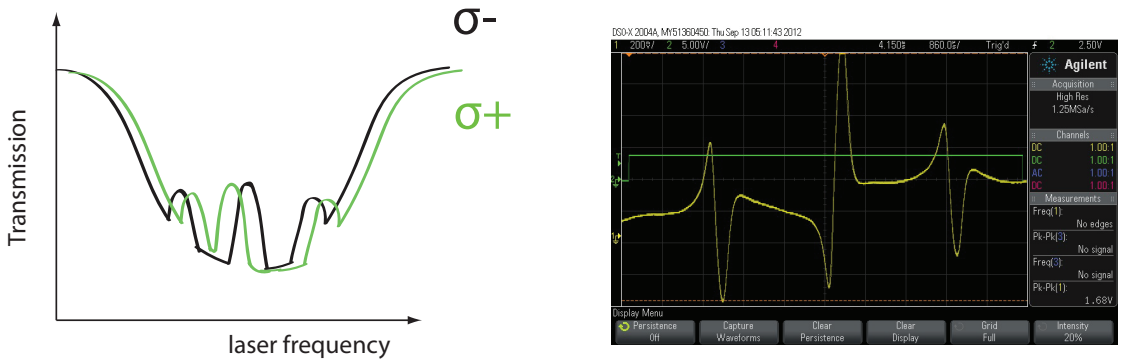


Figure 2.17: The $\sigma+$ and $\sigma-$ signals give rise to an error signal after detection and subtraction through the subtraction circuit.

The error signal is obtained by splitting the probe beam into $\sigma+$ and $\sigma-$ components using a quarter waveplate, a half waveplate, and a polarizing beam splitter. Each beam is detected individually by photodetectors and the two electronic signals are subtracted. A representation of the two signals and the output of the error signal is shown in Fig. 2.17.

### 2.9.1 Locking the laser to the transition wavelength

The laser can be locked to the crossover location using the error signals that are obtained as a function of laser frequency. The laser PZT is subjected to a triangle voltage drive function which changes the laser cavity length and therefore the laser frequency in time. Three error signals are seen as a function of time on the oscilloscope. As the amplitude of the triangle function is reduced, the center of the error signal corresponding to the crossover location must remain close to zero volts. Because the PZT lock circuit is designed to maintain zero voltage of the feedback signal, the ratio of the pump to probe and the splitting of the probe beam via the waveplates to obtain the error signal must be optimized to properly lock the laser to the crossover location. Small offset voltages to the PZT can be used to help zero the error signal if needed. After the amplitude of the triangle drive function to the laser PZT is reduced to zero (and zero volts on the oscilloscope corresponds to the center of the crossover error signal) the PZT lock circuit can be turned on to maintain this zero using PID feedback.

## 2.10 Hyperfine structure and fundamental properties of lithium

The $^7$Li atom has three protons, four neutrons, and three electrons. The $^6$Li atoms three protons, three neutrons, and three electrons. Lithium in the ground state contains 2 electrons in the 1s orbital and a valance electron in the 2s orbital. The nucleus of $^6$Li has a spin $i$ = 1 and a valance electron with a spin $s$ = 1/2. The valance electron and the nucleus spins interact by the hyperfine interaction giving six possible ground states.

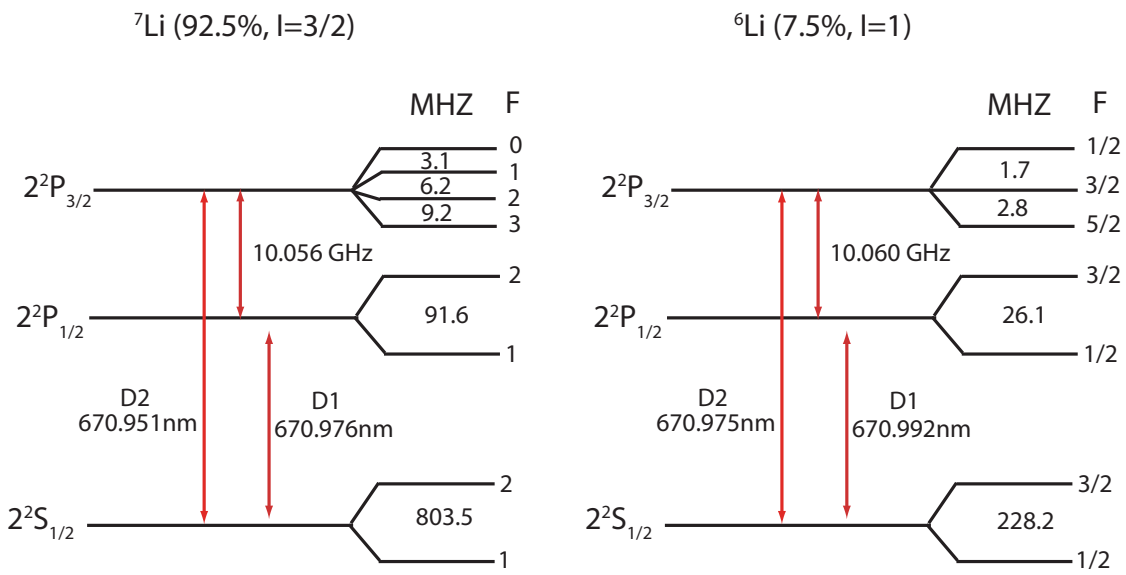


Figure 2.18: Fine and hyperfine structure of $^{6}$Li and $^{7}$Li

Table 2.1: Brief table of fundamental properties of $^6$Li [11]

| Property | Symbol | Value |
|---|---|---|
| Atomic number | A | 3 |
| Nucleons | Z+N | 6 |
| Natural Abundance | | 7.6% |
| Nuclear lifetime | $\tau$ | stable |
| Atomic mass | m | 9.9883414 x $10^{-27}$ kg |
| Total electronic spin | S | 1/2 |
| Total nuclear spin | I | 1 |
| Density (300 K) | | 0.534g·cm$^{-3}$ |
| Melting point | | 453.69 K |
| Heat of fusion | | 2.99 kJ·mol$^{-1}$ |
| Boiling point | | 1615 K |
| Heat of vaporization | | 134.7 kJ · mol $^{-1}$ |
| D1 vacuum wavelength | | 670.992421 nm |
| D1 vacuum wavenumber | | 14903.298 cm$^{-1}$ |
| D1 vacuum frequency | | 446.789634 THz |
| D1 lifetime | | 27.102 ns |
| D1 natural linewidth | | 5.8724 MHz |
| D1 atomic recoil velocity | $v_{rec}$ | 9.886554 cm·sec$^{-1}$ |
| D1 recoil temperature | $T_{rec}$ | 3.53565256 $\mu$K |
| D2 vacuum wavelength | | 670.997338 nm |
| D2 vacuum wavenumber | | 14903.633 cm$^{-1}$ |
| D2 vacuum frequency | | 446.799677 THz |
| D2 lifetime | | 27.102 ns |
| D2 natural linewidth | | 5.8724 MHz |
| D2 atomic recoil velocity | $v_{rec}$ | 9.886776 cm·sec$^{-1}$ |
| D2 recoil temperature | $T_{rec}$ | 3.53581152 $\mu$K |
| Electron spin g-factor | $g_s$ | 2.002319 |
| Electron L = 1 orbital g-factor | $g_L$ | 0.99999587 |

CHAPTER 3

# LITHIUM LASER SYSTEM

## 3.1 Laser light at the $^6$Li D2 transition by injection locking

Injection locking is a technique used to force a slave laser diode to laser at a desired wavelength. A seed laser runs at the desired wavelength, and a portion of the power from the seed is injected into a slave laser. Injection of the seed can be thought of as taking the place of laser feedback, which forces the slave to lase at the wavelength of the seed laser.

Our slave laser diode is an AlGaInP, 650 nm band, 120 mW, Ø5.6 mm (HL 6545 MG) Opnext laser diode that we wish to lase at 671 nm. Several parameters control the output: diode temperature, current, and seed injection power. By heating the diode, the diode physically expands. Heating the diode imposes several risks including shorter diode lifetime and reduced output power. Ideally, the diode should be operated as close to 25$^o$C as possible to increase lifetime.

First, we collimate the slave laser. The free-running slave laser diode is set to run at 25$^o$C and at a pump current above the lasing threshold. The output beam is set to propagate along the entire length of the lab. The output is collimated using a collimation lens located in the TCLDM9 ThorLabs TEC-cooled diode mount. An additional lens is mounted on the diode mount in front of the collimation lens to increase the length of collimation. The resulting beam spot should be Gaussian. Deviation from a Gaussian beam shape could imply poor collimation or damage to the diode.

After the beam is satisfactorily collimated, the beam is then launched into an optical fiber and into a wavemeter. The wavemeter is similar to a Fabry-Pérot

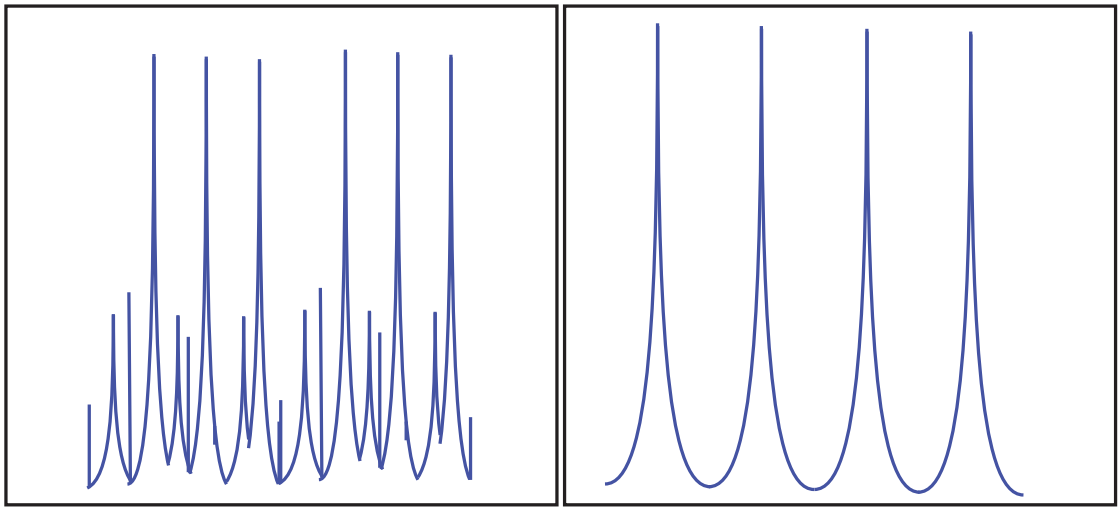

Figure 3.1: Example of the output of a wavemeter. Image on the left shows a multi-mode signal and the image and the example on the right is single-mode.

cavity. The wavemeter spectrum reveals the degree of single-mode behavior and the wavelength. Examples of the output of the wavemeter are shown in Fig. 3.1.

For this particular diode, operation at 58.85$^{o}$C and 138.7 mA results in a free-running wavelength of 670.79 nm. Diode output power is also a function of temperature and is shown in Fig. 3.2.

The injection lock setup, based on the same design that the laboratory has previously implemented in its other experiments, is shown in Fig. 3.3. The master laser is launched into freespace through a fiber coupler. Half and quarter waveplates adjust the polarization of the master laser to attain maximum throughput through the rejected light path of the optical isolator and into the laser diode. A portion of the master laser beam is reflected by a glass slide into a confocal Fabry-Pérot cavity. The output of the slave diode laser passes through an optical isolator and into a fiber coupler. A portion of the slave light is reflected by a glass slide and into the Fabry-Pérot cavity along with the master laser light.

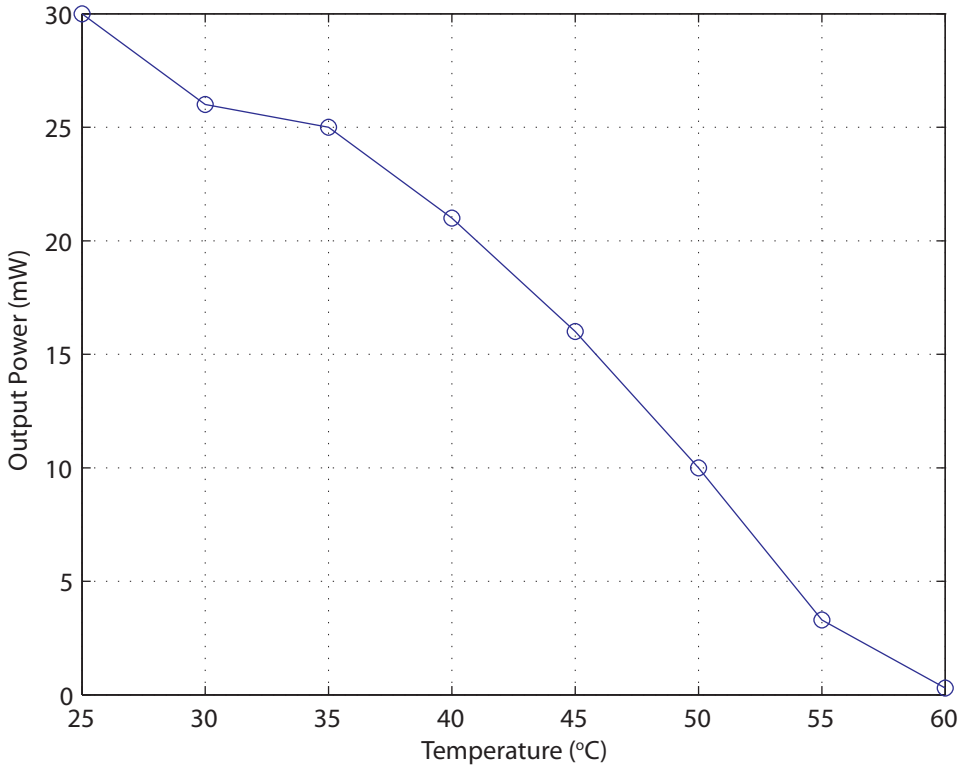


Figure 3.2: Measurements of the free-running diode above the lasing threshold at 90 mA of pump current show that the output power is reduced as a function of increasing internal temperature.

Frequency resolution of the Fabry-Pérot cavity is determined by the free spectral range (FSR), c/(2L). Two 10 cm focal length partially-reflective spherical mirrors in a confocal configuration give a FSR of 1.5 GHZ. A piezoelectric transducer is mounted behind one of the mirrors which changes the cavity length on the order of microns. The piezo is chosen by how many microns it changes per volt. For this setup, the piezo changes by about 140 nm/V and for a wavelength of 671 nm will give an intensity peak in the Fabry-Pérot every 3 V. When driven by a ramped voltage signal up to 10 V, it will cross several intensity peaks. The drive frequency of the piezo much be chosen to be within the bandwidth of the photodiode, which is responding to the change in transmitted intensity of the

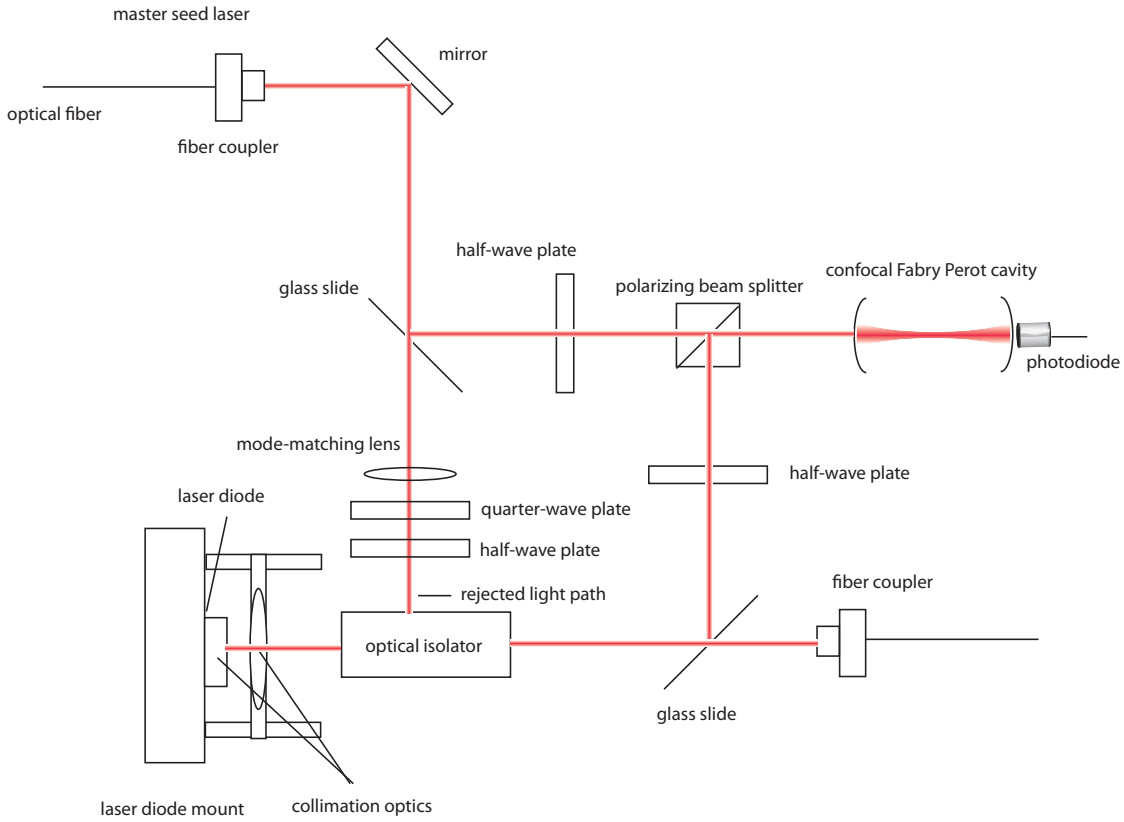


Figure 3.3: Schematic of injection locking scheme. Refer to text for details.

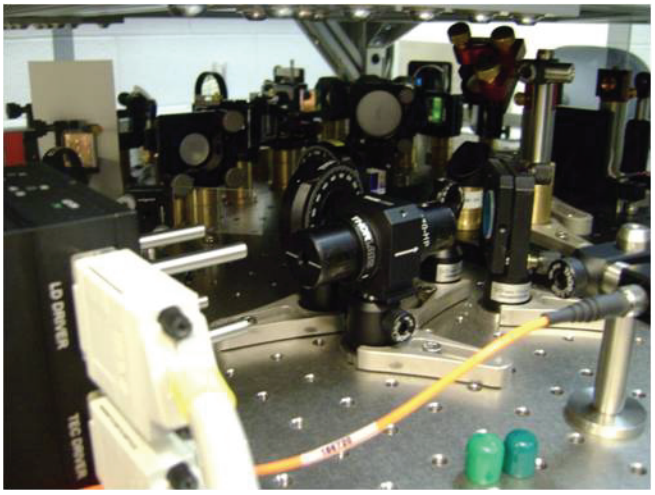

Figure 3.4: Real injection lock setup.

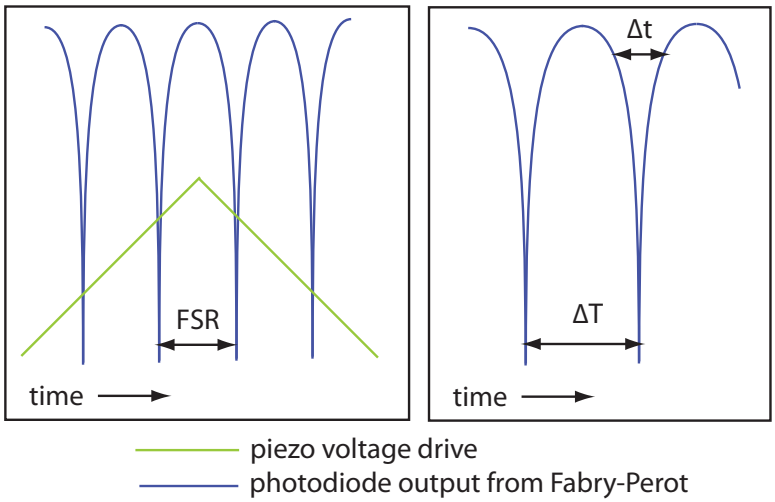


Figure 3.5: Example of the output from the Fabry-Pérot cavity as a function of the piezo drive voltage. The linewidth of the laser can be roughly determined by $\frac{\Delta t}{\Delta T}$*FSR.

Fabry-Pérot as the piezo sweeps through the transmission peaks. Here, we are using an unbiased photodiode (photodiode bandwidth is a function of reverse bias, and typically unbiased photodiodes have lower bandwidth), and so we choose to sweep the piezo at a frequency of 10 Hz. The Fabry-Pérot cavity can also be used to roughly determine the linewidth of a laser beam by its fraction of the FSR, $\frac{\Delta t}{\Delta T}$*FSR. An example of this is shown in Fig. 3.5. A coherent signal results in sharp, narrow transmission peaks through the Fabry-Pérot, and conversely, a continuous spectrum of frequencies present in the beam will cause an increase in the minimum of the null. Therefore, some measure of the quality of the slave laser can be determined by the ratio of the peak to the null of the transmitted intensity.

The master laser is set to lase at a wavelength near 671 nm with a measured input power of 50 $\mu$W into the optical isolator rejected light path. The frequency of the master laser is controlled by a triangle wave voltage input from a signal generator into the PZT inside of the laser which repeatedly sweeps the lasing

frequency.

A lock occurs when the output of the diode follows the frequency sweep on top of the master laser. The master laser and slave laser diode signals are aligned together into the Fabry-Perot cavity, and so the output of the cavity shows the relationship of the two beams. If the two lasers are operating at slightly different frequencies, the output of the Fabry-Pérot will display two peaks. If the frequencies are the same, the output spectra will overlap. An overlap in the peak of the two beams is not sufficient to determine an injection lock. A better test is to sweep the frequency of the master laser while simultaneously observing the slave frequency. Only if the frequency of the diode laser follows the master laser can the locking condition be verified.

A lens located before the optical isolator mode-matches the master laser beam to the diode. The laser diode is first set to run with low pump current (near 50 mA). Lenses of several different focal lengths are inserted into the master laser beam path before the optical isolator. Given the correct lens focal length and position, the slave laser will lock to the master laser by following the sweeping frequency of the master laser. The slave laser diode current is then gradually increased while observing the frequency locking condition at the output of the Fabry-Pérot. Locking conditions were found at 57$^{o}$C and 66 mA of current; at higher currents, the locking condition is lost.

## 3.2 Homemade external cavity diode lasers

Two types of External Cavity Diode Lasers (ECDLs) are needed for our setup: one free running laser near 671 nm for the optical lattice and one locked laser for Raman sideband cooling. To lock the laser to the atomic transition, active feedback is provided by a PZT behind one of the mirror mount adjustment screws to

actively control the horizontal angle. The setup of the laser has a design similar to that which the laboratory has previously implemented, the general measurements are in a computer file drawn by Yogesh Patil, and it is illustrated in Fig. 3.7. A laser diode sits inside of the ThorLabs TCLDM9 temperature controlled laser diode mount. The laser diode mount contains a TEC and provides electrical connections to the TEC and laser current controls through DB9 connections on the case. A collimating lens is placed into the collimation lens mount which is then screwed directly into the mount. The external cavity is formed by a poorly reflecting dispersive grating near 671 nm and is angled at roughly the correct angle by an aluminum mount machined at the appropriate angle. A poorly reflecting grating at the wavelength of interest is used so that the diode does not burn out with too much feedback power. The angle of the grating can be found using the formula,

$$d\left(\sin\theta_{\text{max}} + \sin\theta_{\text{incidence}}\right) = m\lambda \tag{3.1}$$

where $d$ is the distance between each slit in the grating (look this up on the manufacturer's data sheet, given in # slits/mm), $\theta_{\text{max}}$ is angle of the maxima, $m$ is an integer, and $\lambda$ is the wavelength of the incident light. We want the reflection from the grating to go exactly back into the laser diode. To do this we set the angle of the reflected light equal to the angle of incidence giving,

$$\theta_{\text{max}} = \arcsin\left(\frac{m\lambda}{2d}\right). \tag{3.2}$$

This is the angle that the grating needs to be rotated by so that the reflected light from the grating provides feedback to the laser. The aluminum mount must be machined to this angle. We do this by simply rotating the block up by the desired angle and milling across the top and is illustrated in Fig. 3.6. (The best way to do this is to use the machine angle tool in the shop, shown in the Fig. 3.6, for accuracy.) The grating angle is controlled more precisely than the aluminum

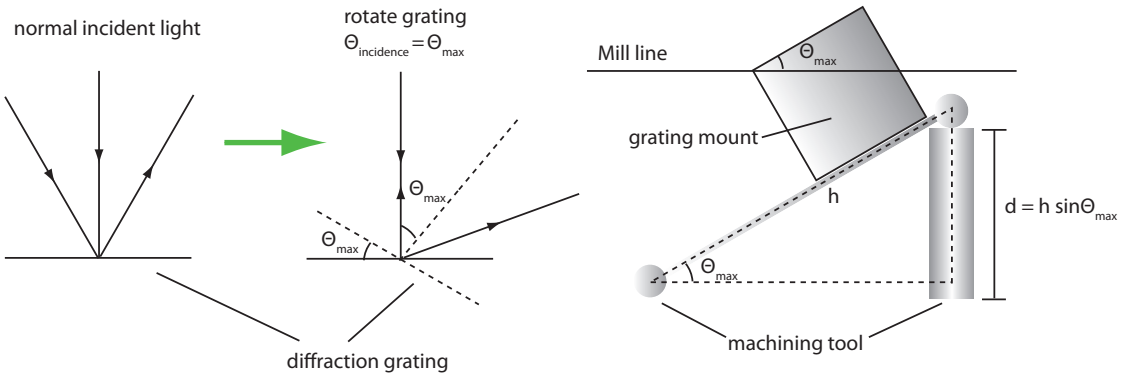


Figure 3.6: We wish for the reflected light from the grating to reflect back into the diode. Set the incident angle $\theta_{\text{incidence}}$ equal to the location of the diffraction maxima $\theta_{\text{max}}$ to find Eq. 3.2. The grating will be flush to the grating mount and so the mount must be machined at the correct angle. Using the mill machine and the machining tool illustrated will help to obtain an accurate angle of rotation. The machine tool is useful for any angles because the distance between the centers of the two circles of equal radii is constant at any angle, so only the height must be calculated.

angle mount by the Thorlabs mount adjustment screws on the mount that supports the aluminum mount. A heat sink, included with the mount package, is located on the back of the laser diode mount for heat dissipation. Both the laser diode mount and the grating mounts are attached directly to a brass base. The brass base helps to mitigate vibrational instability. *Heavy mechanical construction reduces mechanical vibration.* The brass base also increases laser portability as it is screwed down to any optical table or breadboard. The grating is very delicate, and if imprinted with oils from fingerprints it cannot ever be cleaned. Therefore, it is important when handling and mounting the grating to use a nitrile glove to prevent subjecting the grating to damage. The mounts are enclosed inside of an acrylic cage which has holes for adjustment screws on the back of the mount and exiting laser light. Any current controller and TEC controller can be used with the mount provided the pins on the mount and controllers correspond. If one is using current and temperature controllers having different pinouts than

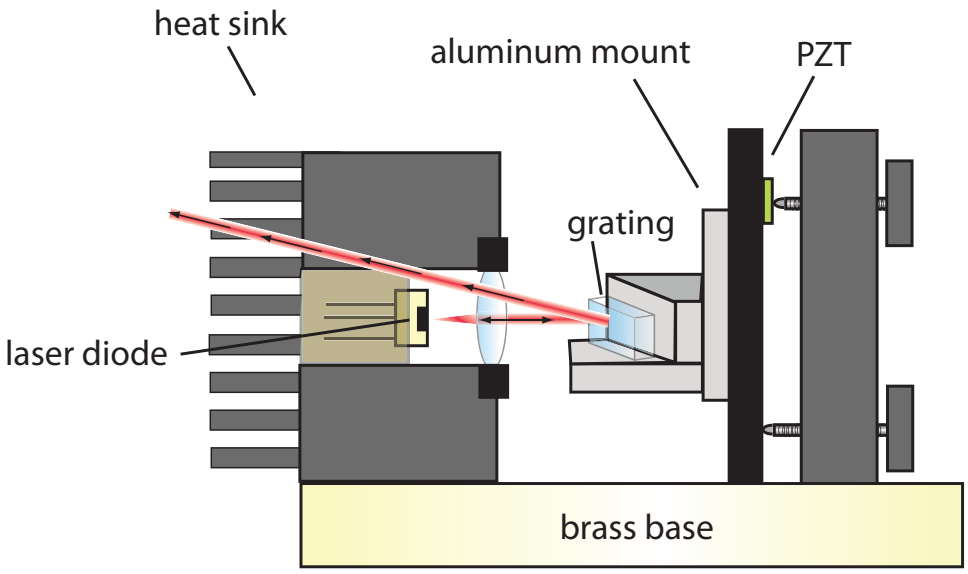


Figure 3.7: Schematic of our homemade ECDL laser, having a design similar to others previously implemented in our laboratory

those specified by the manufacturer, simply construct custom cables to bridge the two units. The TEC and laser current controllers directly provide the mount with current, so one must choose the appropriate gauge of wire which is rated for the intended amount of current.

After turning on the TEC controller and insuring proper temperature control of the laser diode, the laser current is ramped up very gradually to avoid temperature fluctuations which could in turn limit the lifetime of the diode or ultimately destroy the laser diode. After the laser is operating slightly above threshold, the free-running laser light is collimated across the lab by varying the distance between the collimation lens and the laser diode. The shape of the outgoing beam should look approximately Gaussian. Variations of the Gaussian shape of the beam could be indicative of a problem with the laser diode or setup, such as a break in the glass window protecting the laser diode. The grating (on the mounts) is then placed in front of the laser. With the temperature of the laser diode constant, the lasing threshold of the diode is reduced

by adjusting the angle of the grating. A reduction in the lasing threshold ensures that the laser diode is getting feedback from the grating. The laser current is turned down just below threshold and the reflected beam power is monitored by a photodiode outside of the ECDL. As the grating angle is adjusted, the power detected on the photodiode is maximized. The threshold current is reduced further, and the process is repeated until no lasing can be observed. By reducing the lasing threshold, we know that the laser is getting feedback. Now the lasing wavelength must be optimized. Because the grating angle has been adjusted for optimal feedback conditions at the natural wavelength of 650 nm, the grating angle will need to be adjusted further. The emitted beam from the ECDL is fiber coupled and detected by the wavemeter to provide a measure of the quality (multi-mode vs. single mode) and wavelength of the laser light. As the angle of the emitted laser light is adjusted, the light must be continuously fiber coupled into the wavemeter. The lasing wavelength is a function of laser current, temperature, and grating angle. These parameters must be adjusted by trial and error until the desired wavelength is achieved and stable for several days. The wavemeter can record the behavior of the laser as a function of time to determine laser stability. After the stability of the laser is verified, active feedback via the PZT can then be used to lock the laser to the atomic transition.

### 3.2.1 PZT driver

Piezoelectric transducers require a range of voltages, and high voltage PZTs require a power source and driving circuit. The PZT used to stabilize the ECDL requires a high voltage power source and therefore driving circuit. The high voltage power supply is bought as one separate unit and is placed in its own box which is then connected through a BNC to the PZT driving circuit. The PZT

circuits constructed use the same design as the circuits previously implemented in our other labs.

## 3.3 Homemade tapered amplifier

Higher power lasers are desired for laser cooling because they can increase the number of atoms in the MOT. As laser beam size is increased, having the same intensity, one can capture more atoms through a greater the capture volume and solid angle of capture. A large capture volume is useful for capturing atoms from a hot diffusive source, such as the lithium dispensers which give off atoms at a large angle. One way to increase the available laser power to the MOT is to build a laser amplifier. A tapered amplifier compensates for the increase in laser power as the beam propagates through the gain medium by increasing width as a function of length to maintain the same intensity (reducing effects such as self-phase shifting due to the intensity-dependent Kerr nonlinearity). Intensity-dependent nonlinear effects in the medium could affect the spectrum and quality of the output beam. The schematic of the homemade TA, originally designed by my lab partner in M4, Yogesh Patil, is shown in Fig. 3.8. Two lens mounts contain mode-matching lenses. The first lens is used to reduce the waist of the beam to the width of the TA medium which serves to increase the output power and gain efficiency. The second lens collimates the beam. The beam shape out of the TA is naturally elliptical, and requires a cylindrical lens which magnifies along one axis and helps to get back a Gaussian beam shape. A TEC is sandwiched between the heat sink and the copper base and is secured through screws that tighten down the heat sink directly to the copper base. The TA gain medium requires a pump current, and the highly conductive copper base is connected to a power supply. The copper base is insulated from

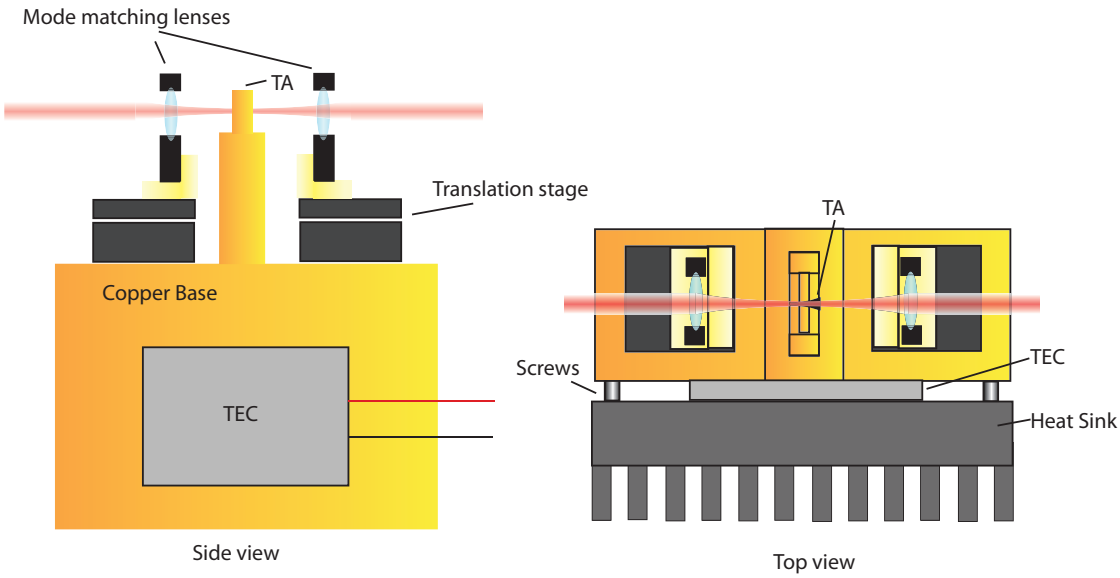


Figure 3.8: Schematic of the homemade tapered amplifier. Left: side view. Right: top view.

the optical table through a non-conductive plastic ring fastened between the brass mount and the copper base. The insulating plastic ring tightened down using an insulating nylon screw which directly connects the copper base to the brass optical base through the insulating plastic ring. Two translation stages are connected directly to the base and a brass adapter is used to connect the lens mounts to the translation stage. Dust and air drafts are detrimental to the stability of the TA and so the entire TA is enclosed in an acrylic cage attached to the heat sink. The translation stages can be adjusted using a hex key outside of the acrylic cage, and therefore adjustments to the beam can be made without opening the cage.

Two TA control circuits are fastened directly to the inside of the acrylic cage. One of these circuits is a TA protection circuit which senses the input seed power of the TA using a photodiode. The calibrated photodiode voltage corresponds to a certain level of input seed power. The photodiode voltage output is connected to one input of a comparator and the second input to an offset voltage. When

the photodiode output voltage goes below the offset voltage, the TA protection circuit opens the switch connecting the TA to the pump current. This prevents the TA from being ruined by being pumped with current without enough seed power. The second circuit simply connects the TEC, thermistor, and TA current to the TEC and laser current controllers. It is composed of two connectors on the front which solder directly to the wires of the TEC, thermistor, and TA current.

## 3.4 Achieving desired frequency detunings from the atomic resonance

### 3.4.1 Double pass AOMs

We lock our lasers to the crossover location of the D2 line, exactly between the hyperfine splittings $|1>$ and $|2>$ of $2^2S_{1/2}$ in 7Li (the most abundant isotope) as shown in Fig. 2.17. The laser will not interact resonantly with the atoms at this frequency, and so we must shift the laser frequency. An acousto-optic modulator (AOM) shifts the laser frequency through the acousto-optic effect. Photoelasticity is the phenomenon responsible for the change in the material's electric permittivity as a function of mechanical strain. As seen in Fig. 3.9, a PZT which oscillates at a given drive frequency is attached to a material (tellurium dioxide in our case) which creates standing waves within the $TeO_2$ medium. Planes of compression and expansion change the index of refraction inducing Brillouin and Bragg scattering of the incoming light leading to wave mixing interactions between the phonons and photons. The shift in energy of the photon is called the Brillouin shift, and it is equal to the energy of the interacting phonon. The incident light interacts and scatters according to the periodicity of the standing

wave and Bragg's law, which gives the angles for the coherent and incoherent scattering angles. Constructive interference occurs when the extra distance that one beam traverses and is an integer multiple of the wavelength, $2d\sin(\theta) = n\lambda$, where $d$ is the spacing between density peaks and $\theta$ is the incident angle. Theoretically, the diffracted angle $\theta$ is dependent on the laser wavelength ($\lambda_l$) and the sound wavelength, which in this case is the wavelength ($\lambda_d$) of the PZT drive,

$$\sin(\theta) = \left(\frac{m\lambda_l}{2\lambda_d}\right). \tag{3.3}$$

The order of diffraction is given by $m$. In practice, one must refer to the manufacturer's data sheet for the calculation of the Bragg angle and proper beam waist taking into account experimental parameters of the device. In our case, the Bragg angle is 19.8 mr ($1.13^o$). The laser output energy is a function of the diffraction order,

$$\omega_{out} = \omega_l \pm m\omega_d \tag{3.4}$$

where $\omega_l$ is the laser frequency and $\omega_d$ is the frequency of the PZT drive. We often want the first order diffraction where $m$ is $\pm 1$. The output modes diffract at different angles, and the beam separation of the orders can be easily calculated (which is often useful for the physical design of the experiment).

Manufactured AOMs are specified to operate within a given wavelength range, but some can be used at wavelengths outside of this range. Here, we use a tellurium dioxide AOM which has a center frequency of 200 MHz, and a rise time on the order of 10 ns. The energy splitting between the hyperfine sublevels in $2^2S_{1/2}$ is 803.5 MHz, and so we need to shift the laser by 401.75 MHz. Because the AOM cannot shift the light by 401.75 MHz, we must pass the light through the AOM twice, in a double-pass configuration as shown in Fig. 3.10.

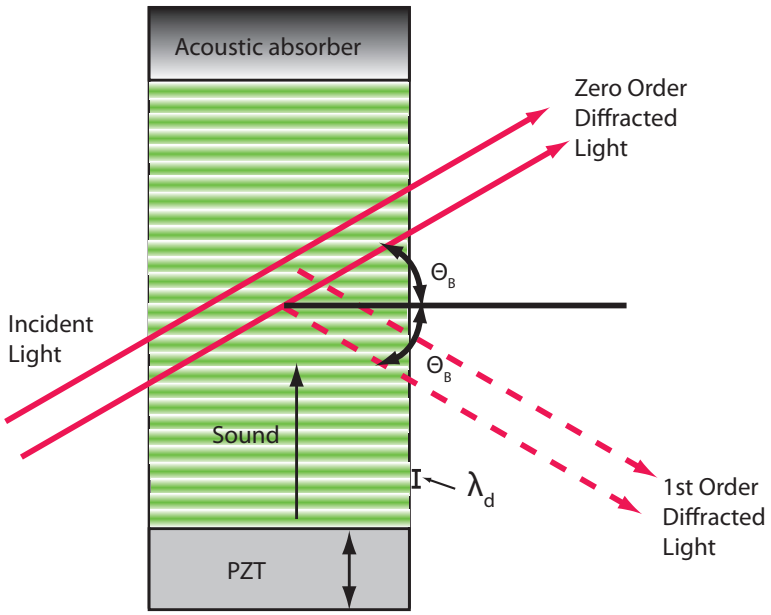


Figure 3.9: Diagram of Bragg scattering in a photoelastic material resulting in optical frequency shifting through the acousto-optic effect. A PZT is driven by an RF signal, and as the PZT oscillates it creates a standing sound wave that travels upward and is absorbed by an acoustic absorber. The compression of the medium affects the index of refraction of the material through the photoelastic effect. The frequency of the light is shifted by energy quanta of the phonons. This momentum transfer is through a photon-phonon interaction called the Brillouin shift. Incident light that is scattered at the Bragg angle is $1^{st}$ order diffracted light and is shifted in frequency by the PZT modulation frequency.

### 3.4.2 AOM efficiency

Efficiency of the AOM is of particular interest in experiments where laser power must be preserved. AOM efficiency is a function of several parameters: RF drive level, RF frequency (into the PZT), laser angle of incidence. The efficiency of the AOMs as a function of these parameters can be exploited and used in optical techniques. It is later shown how we use RF drive level to control the optical power going into the MOT as a part of a scheme to measure atom temperature.

The voltage standing wave ratio (VSWR) takes into account transmission line properties and is one effect on the efficiency of the AOM. We desire a VSWR

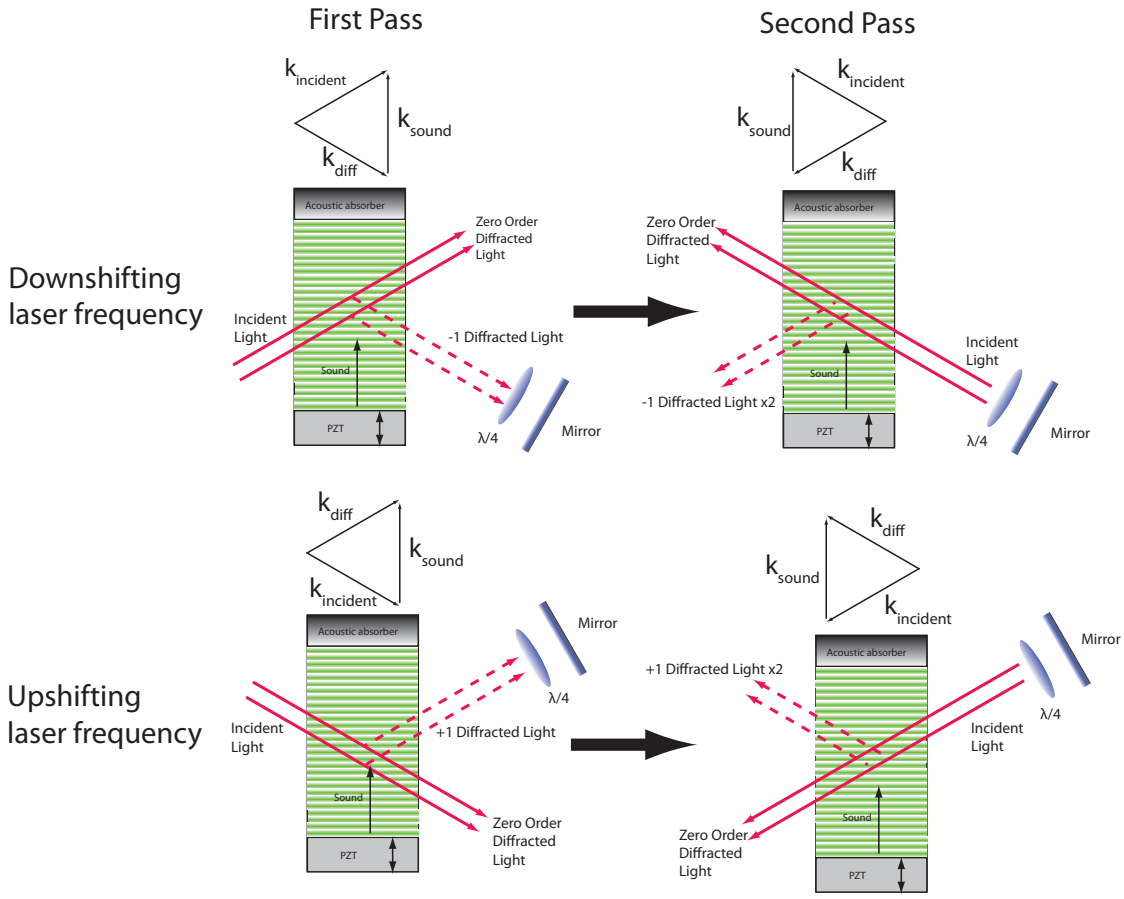


Figure 3.10: Double-pass AOM configurations. The top row shows how to downshift the laser frequency through a double-pass configuration and similarly, the bottom row shows how to upshift the frequency. On the first pass, the laser frequency is shifted by the frequency of the sound wave, and is diffracted into the first order mode. If the direction of propagation of the incident light is along the propagation direction of the sound wave, addition of the momentum vectors results in downshifting the light frequency. This process is shown in the top row of the figure. Similarly, if the light propagation vector is opposed to the direction of propagation of the sound wave, addition of the momentum vectors results in upshifting the light. This process is shown in the bottom row of the figure. After a single pass, the light is rotated in polarization and sent through the AOM again at the same angle. During the second pass, the light is again shifted by the frequency of the sound wave and diffracted into the first order mode. The quarter waveplate at $45^o$ and mirror are used to effectively rotate the linear polarization of the incoming light by $90^o$ (the handedness of the circularly polarized light reverses upon reflection, y flips to -y). The frequency-shifted light traveling along the same light path as the incident light, but in the opposite direction, and can be separated from the incident light using a polarizing beam splitter.

close to unity,

$$VSWR = \frac{V_{max}}{V_{min}} = \frac{1 + \frac{V_r}{V_f}}{1 - \frac{V_r}{V_f}} \tag{3.5}$$

where $V_r$ is the amplitude of the reflected wave and $V_f$ is the amplitude of the forward wave. The VSWR is a way to characterize impedance matching. Proper impedance matching gives a VSWR close to unity, and one can easily measure the VSWR or calculate it from an S11 trace on the network analyzer.

Optical angle alignment is another contributing factor for obtain maximum efficiency. The first order beam at the output of the AOM is separated from the zero order beam, and they each have different intensities and beam shapes. Ideally the zero order beam should look something like a second-order spatial mode (two beam spots) and the first order beam should look similar to a first-order spatial mode (single Gaussian beam spot). This is illustrated in Fig. 3.11.

### 3.4.3 Homemade AOM drivers

Driving our particular AOM takes about 2 W of RF power at about 200 MHz. The AOM driver consists of two pieces, a voltage-controlled oscillator (VCO) circuit and an RF amplifier. The VCO circuits constructed have the same design that our laboratory has previously implemented, and provide voltage-controlled frequency and power which can be either controlled manually by dials on the face or by a computer/function generator. Each VCO contains an oscillator with a range of output frequencies: max range up to 150 MHz or 300 MHz. Here, we show a voltage-to-frequency and voltage-to-power calibration of the 300 MHz VCO in Fig. 3.12.

Nonlinear characteristics of the VCO are measured directly on a spectrum analyzer as a function of power, Fig. 3.13.

We wish to operate the VCO for an extended period of time and any fre-


Figure 3.11: A few common examples of correct and incorrect beam alignments at the output of the AOM. Correct alignment occurs when the zero order beam splits into two equal components that are oriented directly above the first order beam.

quency drift of the VCO corresponds a shift in the laser frequency out of resonance with the atoms. Power drifts correspond to a change in the AOM efficiency. We measure the drift of the VCO at maximum output power of 8.40 dBm and a frequency of 220 MHz over the time period of about one week. Over this time, typical drifts are of the order of 60 kHz. The linewidth of the VCO is about 8 kHz 40 dB down from the peak using a RBW of 1kHz.

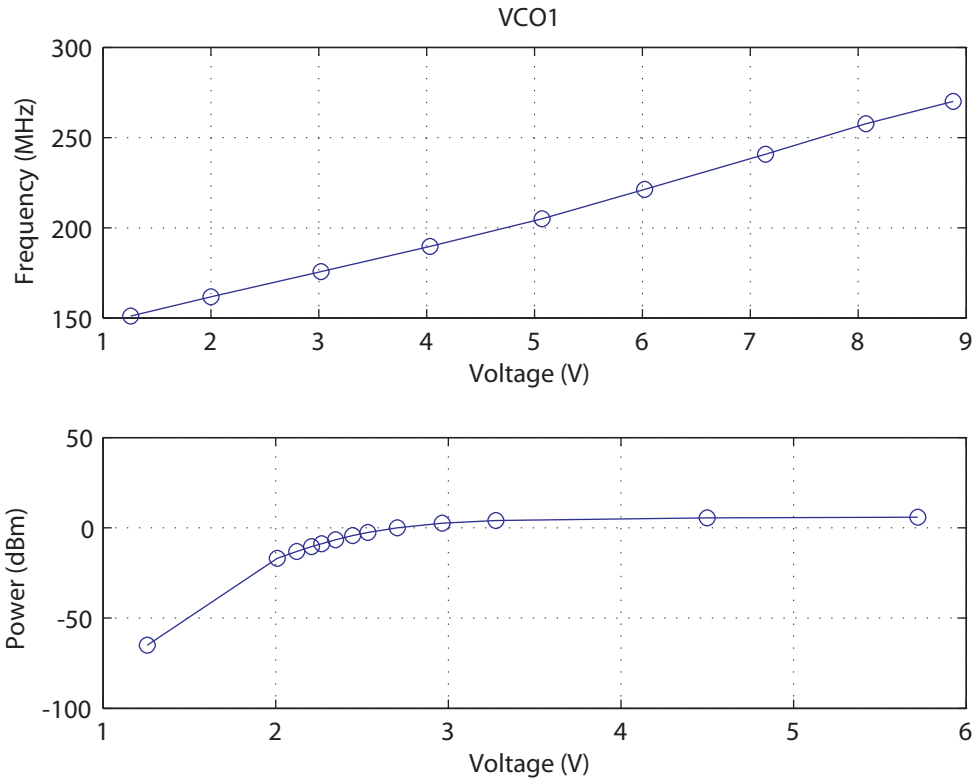


Figure 3.12: We often desire a frequency with an upper limit of 150 MHz or 300 MHz. This figure shows an example of a 300 MHz VCO which we use with the AOM to shift the laser frequency that is locked to the lithium crossover location.

## 3.5 Optical system for the magneto-optical trap

The 3D optical trap is formed by three counter propagating beams with 1 inch diameters. Laser light from the master laser is locked to the crossover frequency, amplified by the tapered amplifier, and passes through an optical isolator. The beam is rotated into a linear polarization where a small portion of the beam is split by a polarizing beam splitter and coupled into fiber which is sent back to the saturated absorption lock circuit. The remainder of the beam is split into two polarizations. One polarization passes through a downshifting double-pass AOM configuration and the other passes through an upshifting double-pass AOM configuration. They recombine through a polarizing beam splitter (PBS)

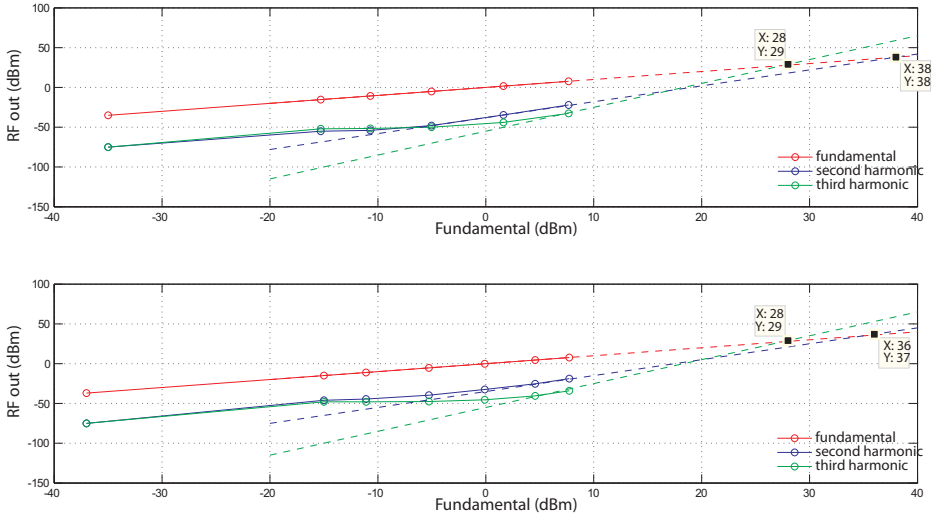


Figure 3.13: The nonlinearity characteristics are measured directly on the spectrum analyzer with a 20 dB pad and DC block in the RF path. The data shown takes into account the 20 dB of attenuation. The intersection shows the points where the fundamental frequency equals the second and third harmonic. Second and third harmonic frequencies are present beyond 0 dBm. We typically operate the VCO at 6 dBm. The RF signal is sent through an RF amplifier that contributes its own additional nonlinearities and amplifies the VCO harmonics. These nonlinearly characteristics are useful to note for reference, but in application the higher frequency harmonics are out of range for the AOM. The AOM is essentially acting as a filter that protects the laser light from losing energy to higher order frequency shifts from atomic resonance.

and together pass through a telescope which expands the beam diameter to 1 inch. The expanded beam is split into three beams of equal intensity by four PBSs. The first PBS splits the horizontal and vertical polarizations (there is no rotation needed here because the beam is already composed of orthogonal polarizations from the double-pass AOM stage). One beam with p polarization is rotated $33^o$ by a half-waveplate so $1/3$ of the power is reflected and $2/3$ is transmitted. Another half waveplate rotates the beam by $45^o$ so the last $2/3$ of power is split in half so that the total power ratio is $1/3$ of the total. Similarly, the other polarization is initially reflected by the first beam splitter and rotated so that

one-third of the power is reflected and two-thirds is transmitted. A $45^o$ rotation allows the remaining power to be split equally. If the initial ratio of downshifted light and upshifted light is equal at the output of the AOM split, this configuration results in equal powers of downshifted and upshifted light of orthogonal polarizations in each beam. The ratio of downshifted light to upshifted light can be easily controlled by adjusting the waveplate before the AOM split. Two beams are periscoped up to the second tier of the optical table where the vacuum chamber sits. Each beam is reflected back onto itself after passing through the vacuum chamber giving three orthogonal counter-propagating beams in x, y, and z. One quarter waveplate is placed on each axis before the beam enters the vacuum chamber so that circular polarization, providing angular momentum, propagates through the vacuum chamber. Because the handedness of the light reverses upon reflection (right circularly polarized goes to left, and vice versa) another quarter waveplate at $45^o$ must be present in front of the second mirror on each axis. This is to ensure that an atom propagating away from the trap and toward the counter-propagating beams will always see the same angular momentum vector and be kicked back into the trap. The schematic of the optical component of the Magneto-optical trap is shown if Fig, 3.14.

## 3.6 Optical lattice laser system

The AC Stark shift is used to confine the atoms and is given by,

$$\Delta E = \frac{-\hbar}{8\delta}\frac{I}{I_{sat}}\Gamma^2 \tag{3.6}$$

where $\delta$ is the detuning of the lattice light, $\Gamma$ is the natural linewidth, I is the intensity of the light, and $I_{sat}$ is the saturation intensity. We would like the lattice depth to be at least ten times the average thermal energy of the atoms confined

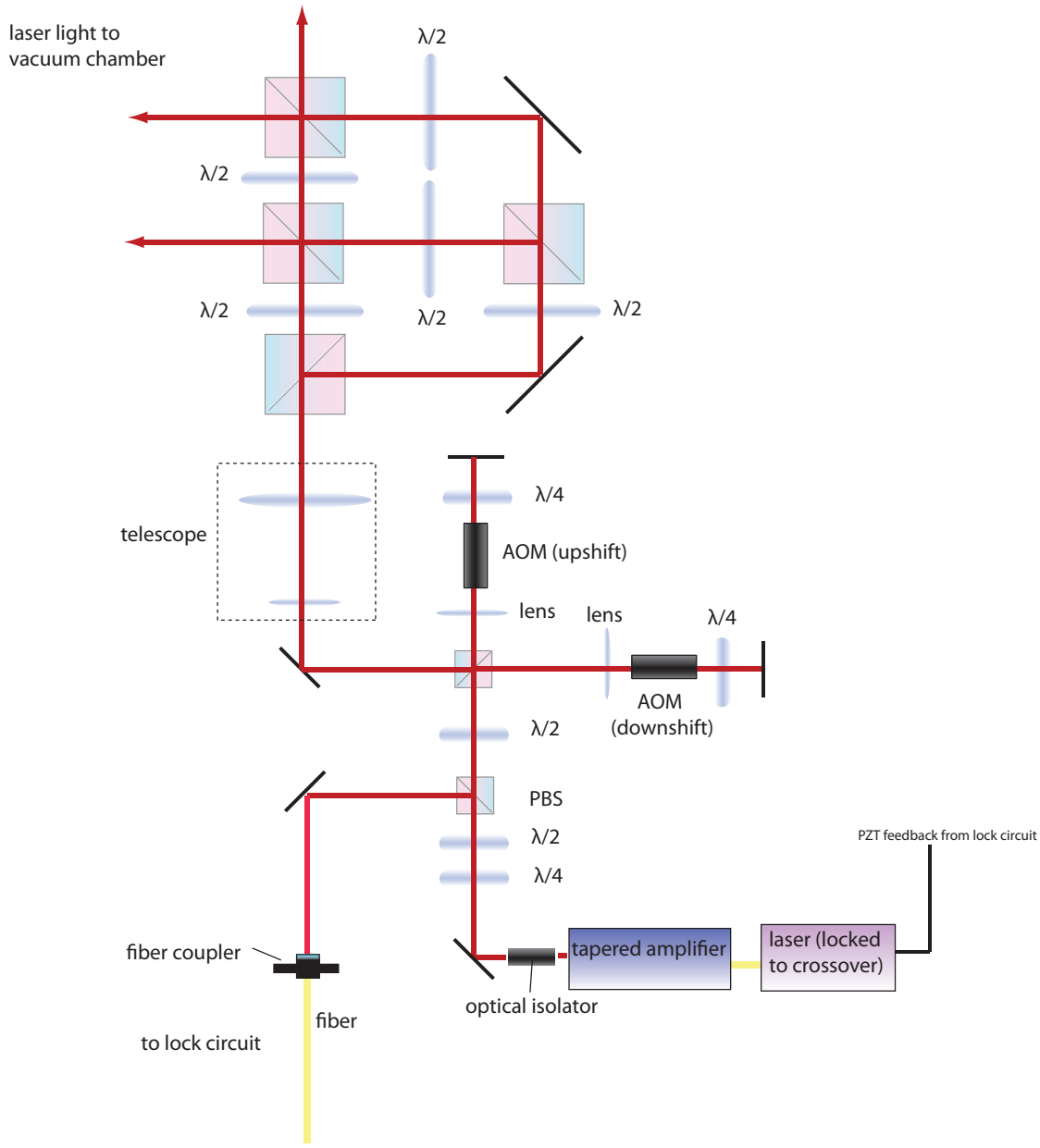


Figure 3.14: Schematic of the optical system for the lithium magneto-optic trap.

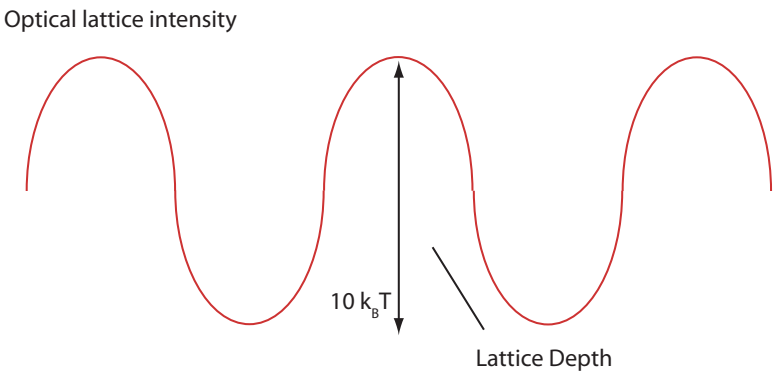


Figure 3.15: Depth of the lithium lattice is chosen to be ten times the average thermal energy of the atoms.

in the MOT,

$$\Delta E_{\text{lattice}} = 10 k_B \text{T}. \tag{3.7}$$

Equating the desired lattice depth to the AC Stark shift,

$$\frac{-\hbar}{8\delta}\frac{I}{I_{sat}}\Gamma^2 = 10 k_B \text{T} \tag{3.8}$$

$$I = \frac{-80 k_b \text{T} \delta I_{sat}}{\hbar \Gamma^2}, \tag{3.9}$$

we find the needed intensity of laser light needed to achieve the desired optical lattice depth as a function of detuning. We set the following parameters: $\text{I}_{sat}$ = 7.59 mW/cm$^2$, T = 0.5 mK (recall that lithium does not experience effective polarization gradient cooling and is therefore limited to temperatures comparable to the Doppler limit as opposed to the recoil limit), $\Gamma = 2\pi$ 5.85 MHz, and find the desired lattice depth as a function of intensity.

The lattice light scatters with the atoms resulting in a heating rate based on the scattering rate. The scattering rate,

$$R_{sc} = \frac{\Gamma}{2}\frac{\frac{\text{I}}{\text{I}_{sat}}}{1 + \frac{\text{I}}{\text{I}_{sat}} + \left(\frac{2\delta}{\Gamma}\right)^2}, \tag{3.10}$$

is related to the heating rate by [12],

$$\frac{dE}{dt}(J/s) = \frac{\hbar^2 k_l^2}{2m} R_{sc}. \tag{3.11}$$

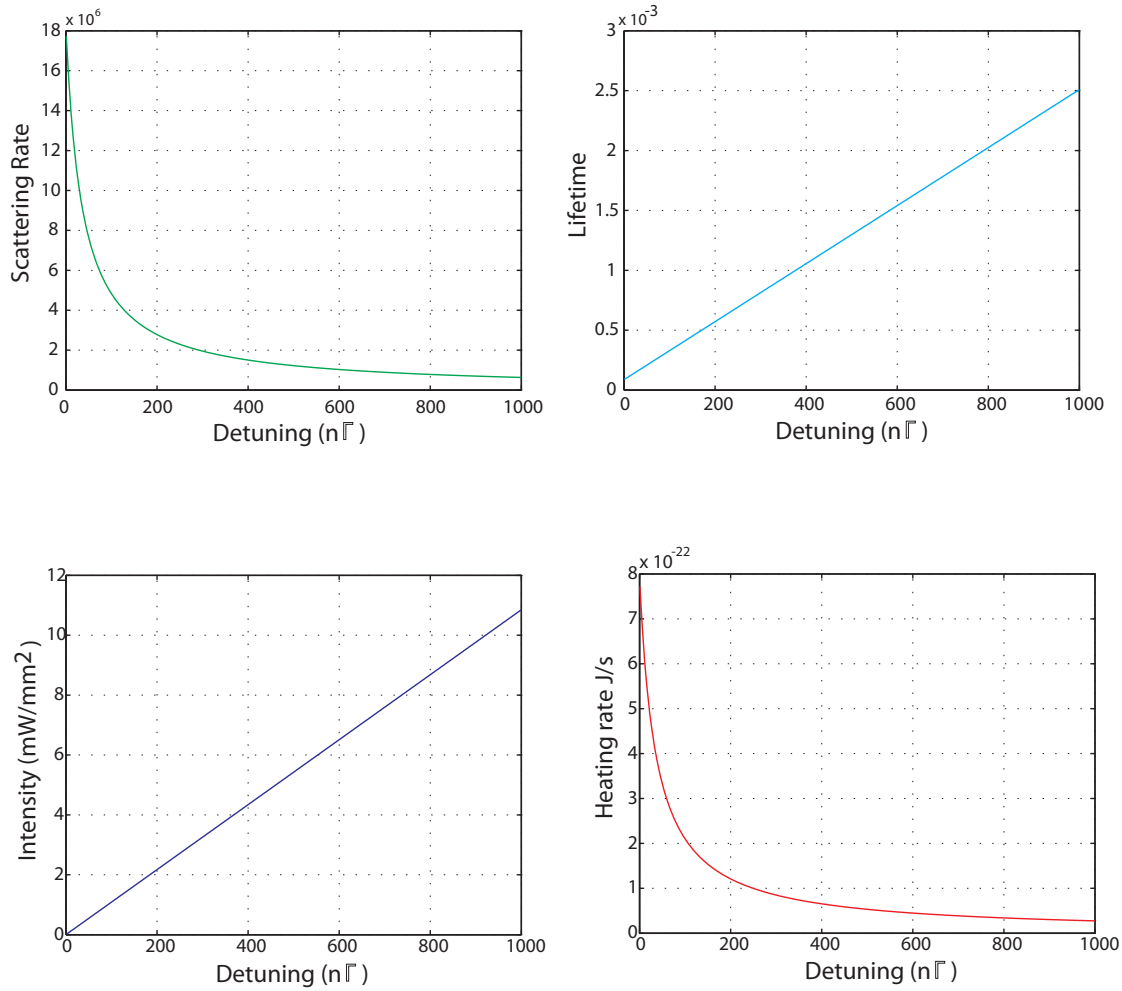


Figure 3.16: Calculated laser light intensity, scattering rate, atomic heating rate, and average atom lifetime in the lattice for the given lattice depth of $10k_B$T.

where $k_l$ is the laser wavenumber. The average lifetime is approximated from the heating rate and the lattice depth,

$$\Delta E = \frac{\hbar^2 k_l^2}{2\mathrm{m}} R_{sc} \Delta t = 10 k_B \mathrm{T} \tag{3.12}$$

$$\Delta t = \frac{20 k_B m T}{\hbar^2 k_l^2 R_{sc}}. \tag{3.13}$$

Results are calculated for a lattice depth of $10k_BT$ with $T$ = 500 $\mu$ K and summarized as a function of detuning in Fig. 3.16. The lattice potential is formed by the interference of two beams, and is subject to instabilities and shaking from laser

frequency shifts, mirror movement, etc. The lattice instabilities due to intensity fluctuations are controlled by an intensity stabilization feedback circuit.

CHAPTER 4

# LITHIUM MAGNETIC FIELD SYSTEM

The magnetic fields for the ultracold lithium apparatus are generated from Helmholtz coils and anti-Helmholtz coils. In our system, the Helmholtz coils have 20 turns and the anti-Helmholtz coils have 17.75 turns.

## 4.1 Magnetic quadrapole trap

The anti-Helmholtz coils form a magnetic quadrapole trap. Two current loops having opposite currents create opposing magnetic fields that result in a magnetic field gradient for atom confinement in the magneto-optic trap. As the atoms move from the center of the trap, they experience increasing magnetic strength in all directions. The increasing magnetic field causes an increasing splitting in the atom's magnetic sublevels, eventually bringing the atom into resonance with the counter-propagating laser beams. The atoms absorbs a resonant photon and by doing so receives a momentum kick in the direction of laser propagation back toward the center of the trap.

The magnetic field gradient in the z-direction can be calculated using,

$$\frac{\partial B}{\partial z} = \frac{3}{2}\mu \mathrm{nIR}^2 \left( \frac{z + d/2}{(R^2 + (z + d/2)^2)^{\frac{5}{2}}} - \frac{z - d/2}{(R^2 + (z - d/2)^2)^{\frac{5}{2}}} \right) \tag{4.1}$$

where $\mu$ is the magnetic permittivity, R is the radius of the coils, I is the current, and d is the coil separation. Using the parameters for our system: d = 9.4 cm, R = 3.375 in, and n = 18, the magnetic field gradient as a function of current is shown in Fig, 4.1.

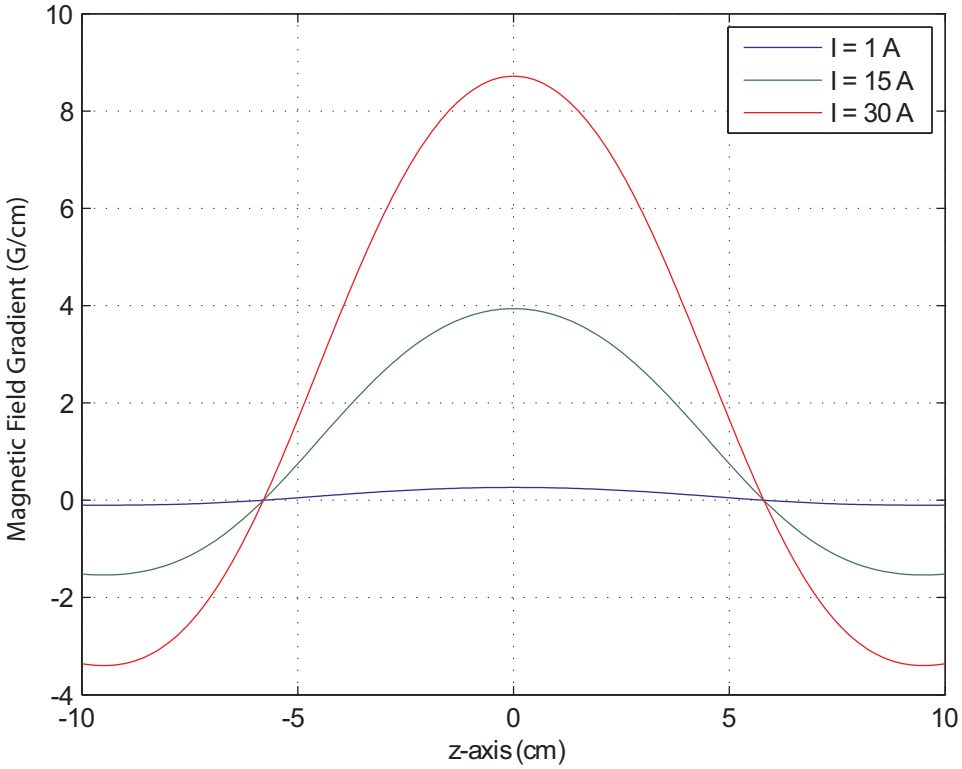


Figure 4.1: Calculated magnetic gradient in the z-direction as a function of current for the lithium magneto-optic trap by Eqn. 4.1.

### 4.1.1 Power dissipation of anti-Helmholtz coils

Current running through the anti-Helmholtz coils is relatively high, up to 30 A as shown in Fig. 4.1. The coils may need water-cooling for increased power dissipation. The anti-Helmholtz coils are hollow and coated with an electrically insulating, polyimide film called Kapton, that is stable across a wide range of temperatures (-450 to 752 $^{o}$F) and has a low outgassing rate (so we can use it in the ultra-high vacuum chamber). Slightly pressurized water from the lab's faucet is sent through the coils, so the water flows through the coils which are mounted on the vacuum chamber and back out to the faucet. We measure the flux of water through the coils by finding the time it takes for a beaker to fill to

100 mL. About 75 mL/min is good enough to dissipate 1 kW of power.

### 4.1.2 Helmholtz coils

Helmholtz coils are oriented orthogonally to create uniform, constant magnetic fields in two directions which cancel Earth's magnetic field and other stray magnetic fields. These stray magnetic fields could change the location of the MOT center causing misalignment of the optical and magnetic centers. The magnetic zero can be found by sweeping the current through the coils and performing a time of flight measurement. The Helmholtz coils are also used to generate the Zeeman shift for Raman sideband cooling.

## 4.2 Current control of Helmholtz coils

### 4.2.1 Magnetic field and current from lattice energy level spacing

Raman sideband cooling of lithium requires a magnetic field to induce a Zeeman energy shift in the lithium atoms. The energy level spacing between the magnetic hyperfine levels are equal to the energy level spacings in the harmonic optical lattice trap. We now must calculate the current we need for the Helmholtz coils to provide the Zeeman shift for Raman sideband cooling. The diagram for the calculation is given in Fig. 4.2. The magnetic field corresponding to the lattice energy level spacing is given by,

$$U = -\mu \cdot B \tag{4.2}$$

$$h\nu = g\mu_B B \tag{4.3}$$

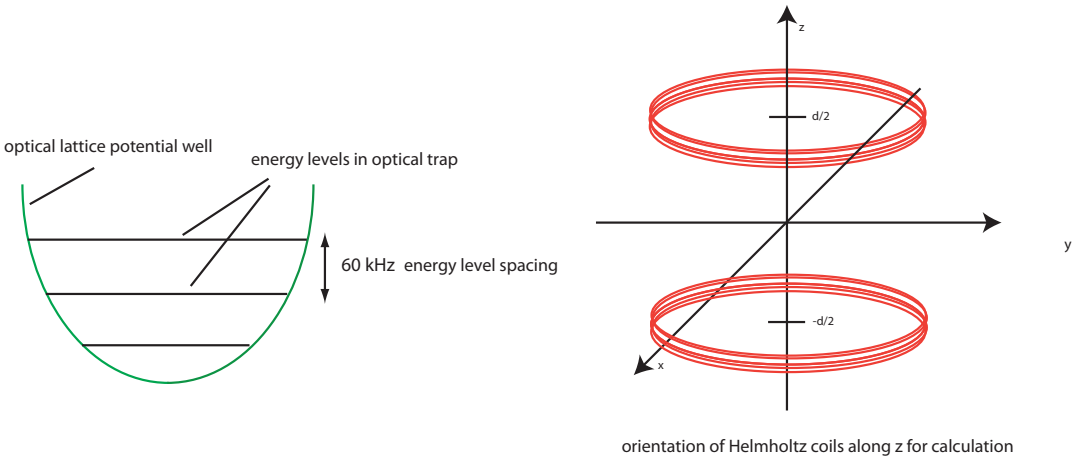


Figure 4.2: An energy level spacing of 60 kHz is estimated, requiring a magnetic field which is controlled to 1/100 accuracy using a current control circuit. The image on the right shows the orientation of the Helmholtz coils related to the current calculation.

$$B = \frac{h\nu}{g\mu_B} = \frac{f}{700kHz/G} \tag{4.4}$$

The lattice spacing is estimated to be 60 kHz giving,

$$B = \frac{60kHz}{700kHz/G} = 85.7mG \tag{4.5}$$

In order to get a lattice spacing of 60 kHz, we need a magnetic field of 85.7 mG. Our resolution requirement is $\frac{1}{100}$ of the field, and so we must be able to control the magnetic fields up to a resolution of 0.857 mG.

The magnetic field generated from the Helmholtz coils in the z-direction is,

$$B_z = \frac{\mu_0 I R^2}{2}\left[\left(R^2 + \left(z - \frac{d}{2}\right)^2\right)^{\frac{-3}{2}} + \left(R^2 + \left(z + \frac{d}{2}\right)^2\right)^{\frac{-3}{2}}\right]. \tag{4.6}$$

At the center between the coils, z = 0, and with each coil having 20 turns,

$$B_z = \frac{20\mu_0 I R^2}{\left[R^2 + \left(\frac{d}{2}\right)^2\right]^{\frac{3}{2}}}. \tag{4.7}$$

Solving for the current gives,

$$I = \frac{B_z}{20\mu_0 R^2}\left[R^2 + \left(\frac{d}{2}\right)^2\right]^{\frac{3}{2}}. \tag{4.8}$$

The radius of the coils is $R = 7.15$ cm, the distance of the coils from z = 0 is $\frac{d}{2} = 8.89$ cm. To get a magnetic field of 85.7 mG we need a current of 1.98 A and a resolution of 19.8 mA. Our Hall probe is calibrated at 3.5 A/V and we therefore need control of the voltage within,

$$V = \frac{I}{3.5A/V} = \frac{990\mu A}{3.5A/V} = 283\mu V. \tag{4.9}$$

### 4.2.2 Current control for Raman sideband cooling

Precise control of the Helmholtz coils is needed for Raman sideband cooling, where the energy levels of the lattice must be equal to the energy splitting of the hyperfine sublevels. The magnetic field generated by the Helmholtz coils induces a Zeeman shift, and so noise in the current within the Helmholtz coils equates to noisy fluctuations in the magnetic field and hyperfine energy level separations.

We also wish to switch the magnetic field on and off as quickly as possible, but because the magnetic field is generated by current running through a coil geometry, the shortest risetime of the magnetic field is inductance-limited.

The experimental setup is shown in Fig. 4.3. A solid state relay (high power MOSFET) is used to open and close the current loop containing the Helmholtz coils. After switching on the relay, current begins to flow through the coils according to,

$$V = L\frac{dI}{dt} \tag{4.10}$$

where V is the voltage across the inductor, L is the inductance, and I is current through the inductor.

The current through the coils spikes and oscillates until equilibrium is reached. Current oscillation results in oscillating magnetic fields that dynamically change

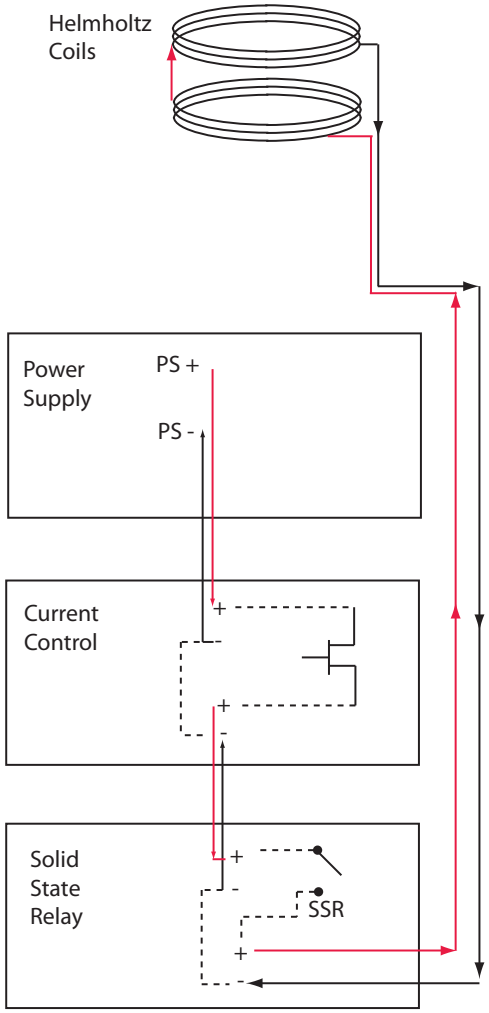


Figure 4.3: Experimental setup of the Helmholtz coils control circuit. The high current power supply is connected to the source of the MOSFET and the drain connected to the solid state relay. The solid state relay opens and closes the current loop to the Helmholtz coils; they are individually voltage-controlled. The drain of the relay is connected to the Helmholtz coils and back to the negative terminal of the high current power supply by way of passive wiring through the circuits.

the energy splittings of the atoms, knocking them out of the trap. To achieve Raman sideband cooling, we must also control these current oscillations through a PI circuit.

In summary, the current control circuit for the Helmholtz coils must provide control and magnetic noise within 0.857 mG, inductance-limited rise time, and mitigation of current oscillation and spiking from the sudden increase of current through the coil from a square pulse.

The current control circuit constructed uses the same board design that the laboratory has implemented previously in other experiments, and basic operation of the current control circuit is as follows: A PI loop compares the set voltage (set manually of using a function generator) and the feedback voltage obtained from the Hall probe (around the wire containing current to the Helmholtz coils) to control the gate voltage of a water-cooled MOSFET. A calibration of our FW Bell (CLSM-200LA) Hall probe is shown in Fig. 4.4. The drain and source of the MOSFET are connected to a high current power supply which is the source of current to the Helmholtz coils. For example, when a square pulse is sent into the current control circuit, the circuit will detect an error between the set voltage and the voltage obtained from the Hall probe. It will increase or decrease the gate voltage of the MOSFET according to the PI parameters. We optimize the parameters such that the current oscillations due to the inductance are minimized. Ground isolation between the circuit and the MOSFET is achieved by through a virtual ground generated by a Zener diode with a precision unity gain differential amplifier (INA105). We first test the circuit using a single test coil which is almost identical to one of the coils in the Helmholtz configuration installed on the lithium apparatus. An example of the current control operation is shown in Fig. 4.5.

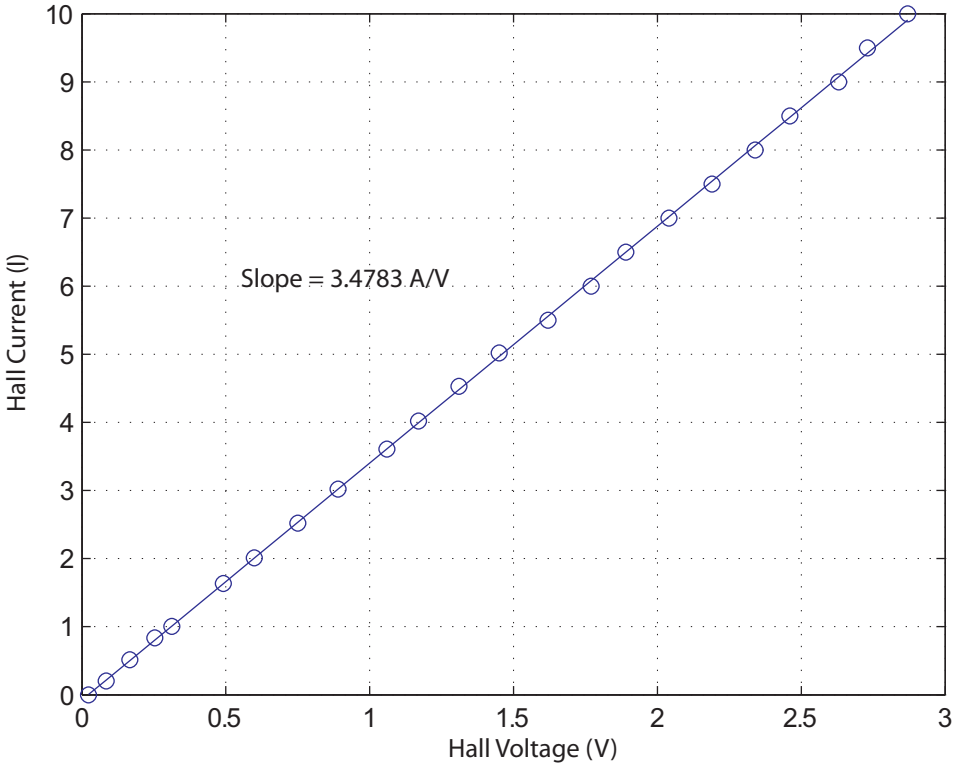


Figure 4.4: The Hall probe is calibrated by measuring the voltage as a function of known current. In our setup, the calibration is about 3.5 A/V. Note that the Hall resistor can be changed from the values specified by the manufacturer as long as the power consumption remains within the maximum power dissipation of the Hall probe.

**Crosstalk between current control circuits**

Crosstalk between the current control circuits causes current noise in one coil due to influence of the other coil. The crosstalk we are concerned about occurs inside of the current control circuit when a circuit influences the gate voltage control in a nearby circuit. Crosstalk is tested between three different circuits at the same time. Each circuit is controlled with a different set voltage functions via function generators. Hall voltage signals from each of the three coils are individually measured on an oscilloscope. If crosstalk is present, the pattern from one of the coils will be seen in the measured spectrum. Results of this test

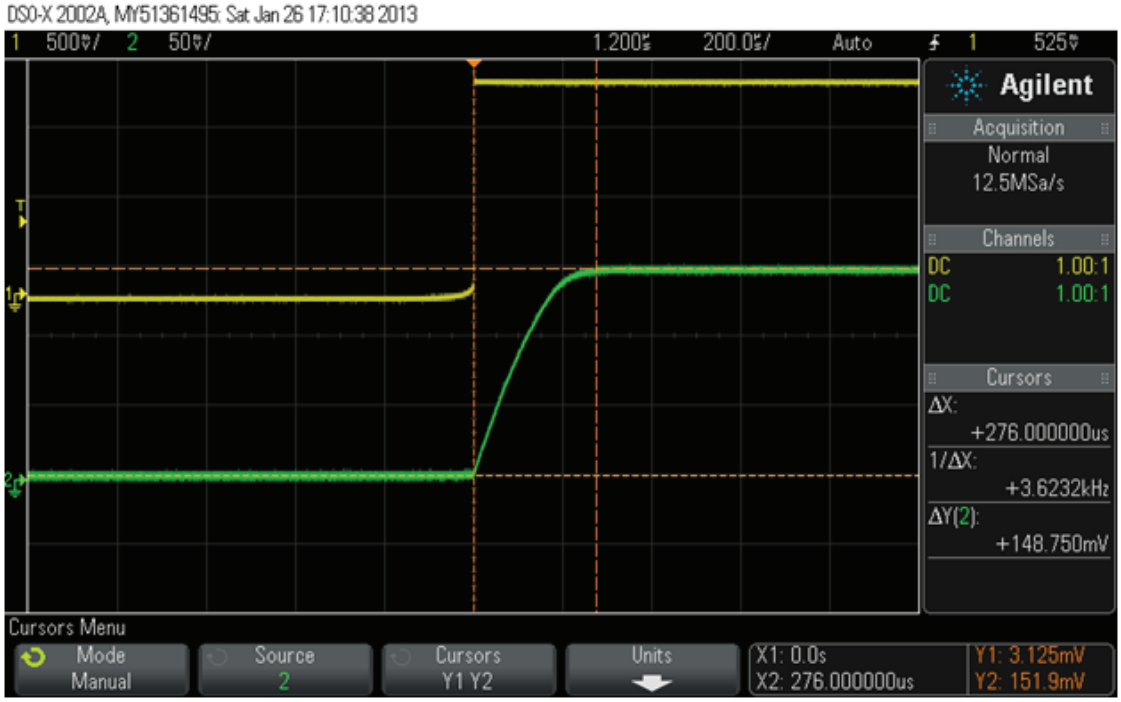


Figure 4.5: Example of the operation of the current control circuit used for Raman sideband cooling. A control voltage pulse (yellow) is sent from a function generator to the voltage set-point of the PI circuit. Voltage feedback is obtained from the Hall probe monitoring the current loop. The voltage feedback from the Hall probe subtracts from the set point providing an error signal to the PI portion of the current control circuit. A voltage dependent on the error signal and PI parameters is sent to the gate of the MOSFET controlling the current through the Helmholtz coils. Peak voltage is measured from the Hall probe (green) having a calibration of 3.5 A/V giving a max current of 0.518 A.

for our circuit is shown in Fig. 4.6.

### Reduction of risetime

One way to reduce the risetime is to increase the voltage across the inductor. In this case the voltage across the inductors is the same voltage as the drain-source voltage across the MOSFET. The inductance of the test coil is approximately,

$$L = \frac{\mu_0 \mathrm{n}^2 \mathrm{A}}{\mathrm{l}} \tag{4.11}$$

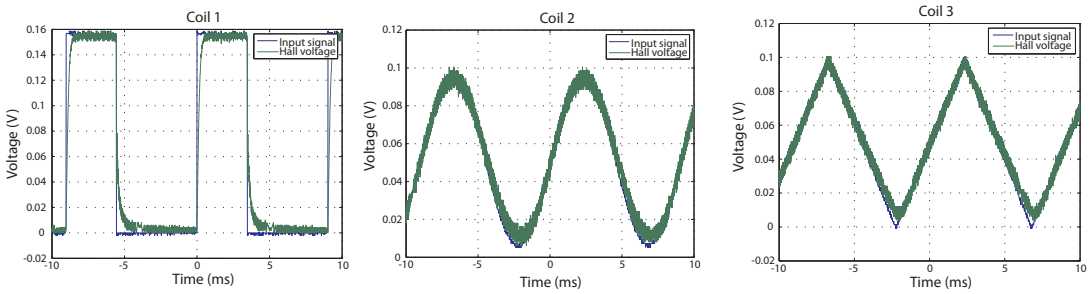


Figure 4.6: Crosstalk measurements using Hall probes on three simultaneously-running inductors, each controlled by individual current control circuits in close proximity.

where n is the number of turns, A is the area of the coil, l is the length of the coils and $\mu_0$ is the vacuum magnetic permittivity. Using the parameters for our test coil, n=18, l = 2 cm, A = (5.75cm)$^2\pi$ = 103.9 cm$^2$, the inductance is approximately 211 $\mu$H. We find the inductance-limited risetime by,

$$\partial t = \frac{L}{V}\partial I. \tag{4.12}$$

The measured risetime and the calculated risetime (based on our estimate of the inductance of the coil) as a function of drain-source voltage is shown in Fig. 4.7.

**Reducing low-current noise**

We wish to control the magnetic field to 1/100 of the total magnetic field. To control this current to 1/100, we optimize all parameters which can reduce noise. At low currents we detect sawtooth oscillations as shown in Fig, 4.8. The sawtooth oscillations are reduced by placing a resistor before the gate which functions to impedance match the current control circuit to the MOSFET.

The circuit has an intrinsic bandwidth which can act as a low-pass filter for higher frequency noise. The bandwidth of the filter is determined by measuring the 3dB point. A sinusoid of increasing frequency is sent into the control input

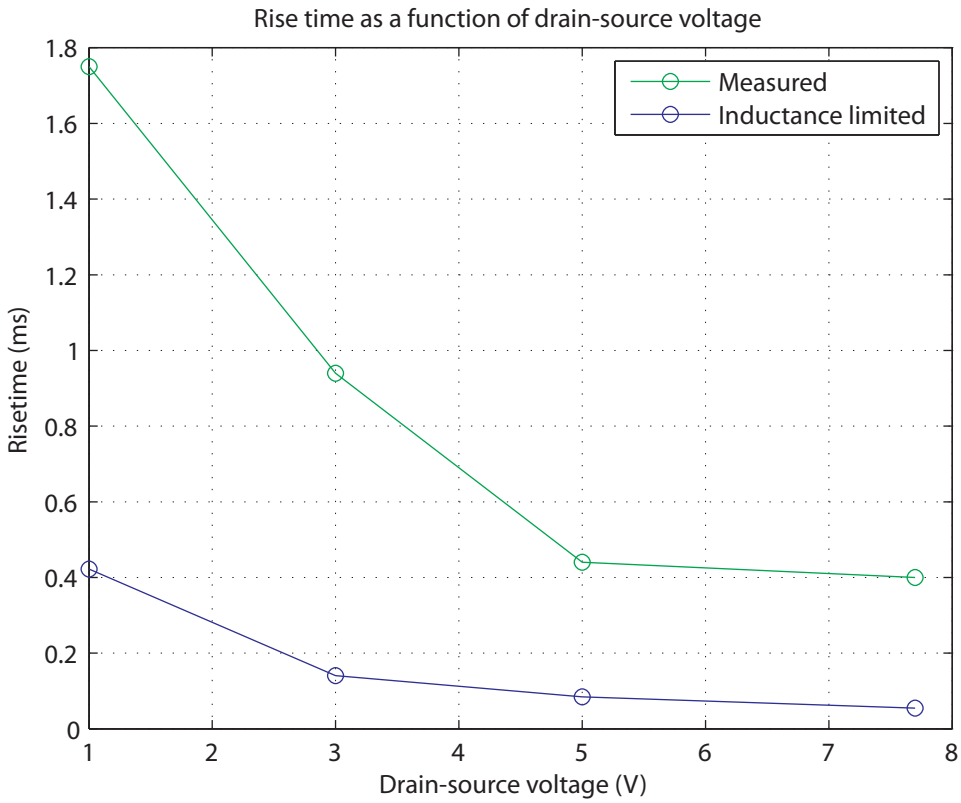


Figure 4.7: Risetime of the controlled current across the test inductor as a function of MOSFET drain-source voltage. The inductance limit is calculated by Eqn. 4.12 and uses an estimation of the inductance of our test inductor.

which creates an oscillating current in the inductor. The frequency at which the amplitude of the received signal is reduced by $1/\sqrt{2}$ corresponds to the 3 dB point. The measurement is shown in Fig. 4.9. The bandwidth of the circuit is also a function of the PI parameters, and the bandwidth range is well within 1 kHz - 5 kHz.

Current noise can be reduced further by adding a preamp circuit in the Hall probe feedback. The preamp reduces ground loop noise through the wires carrying the Hall voltage to current control circuit board. The bandwidth of the preamp circuit is important to consider because it is in the Hall feedback loop. The corner frequency of the preamp circuit is 6.32 kHz, which is greater than

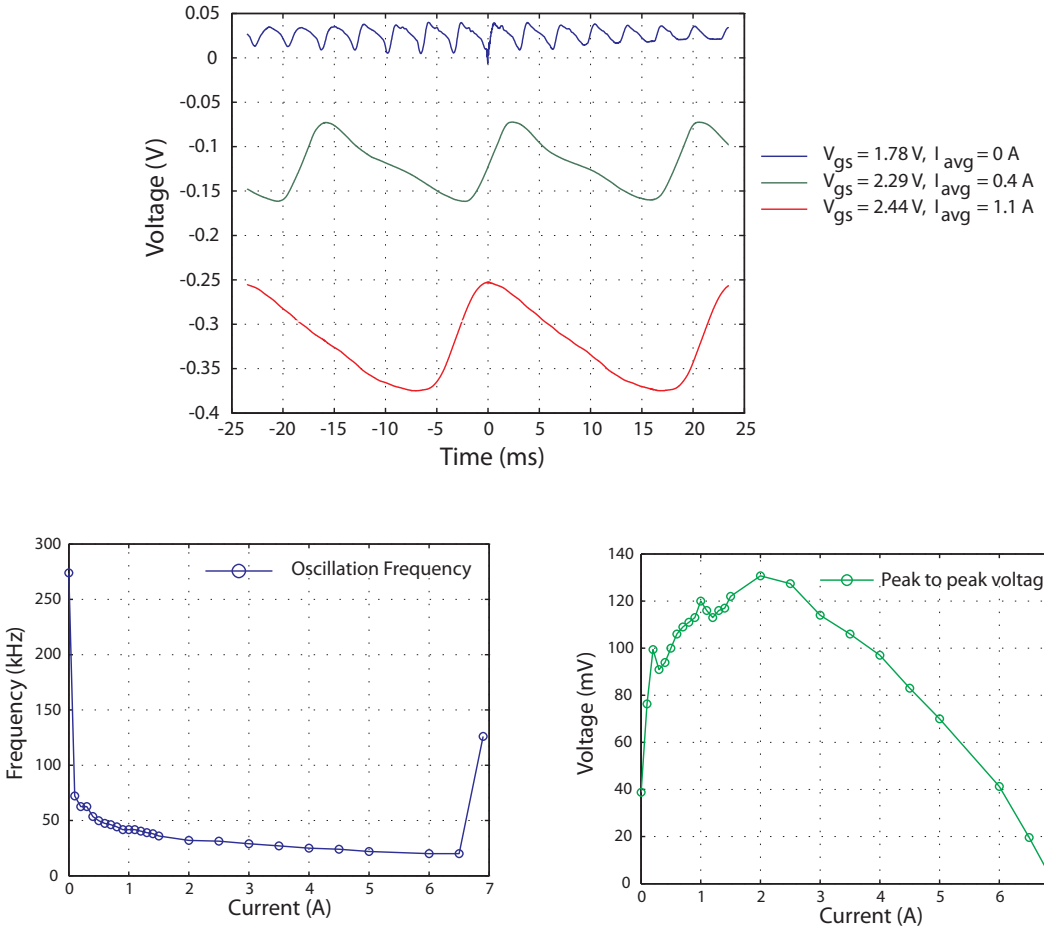


Figure 4.8: Sawtooth oscillations in the current from the impedance mismatch of the MOSFET gate and circuit. The frequency and amplitude of these oscillations change as a function of current. $V_{gs}$ is the gate-source voltage which controls the current running through the MOSFET drain-source path. $I_{avg}$ is the average current running from the drain to the source. The bottom two figures show how the amplitude and frequency of the oscillations change with current.

the bandwidth of the current control circuit at all PI parameters.

From the setup in Fig. 4.10 to measure current noise on the spectrum analyzer, we obtain the current noise spectrum shown in Fig. 4.11.

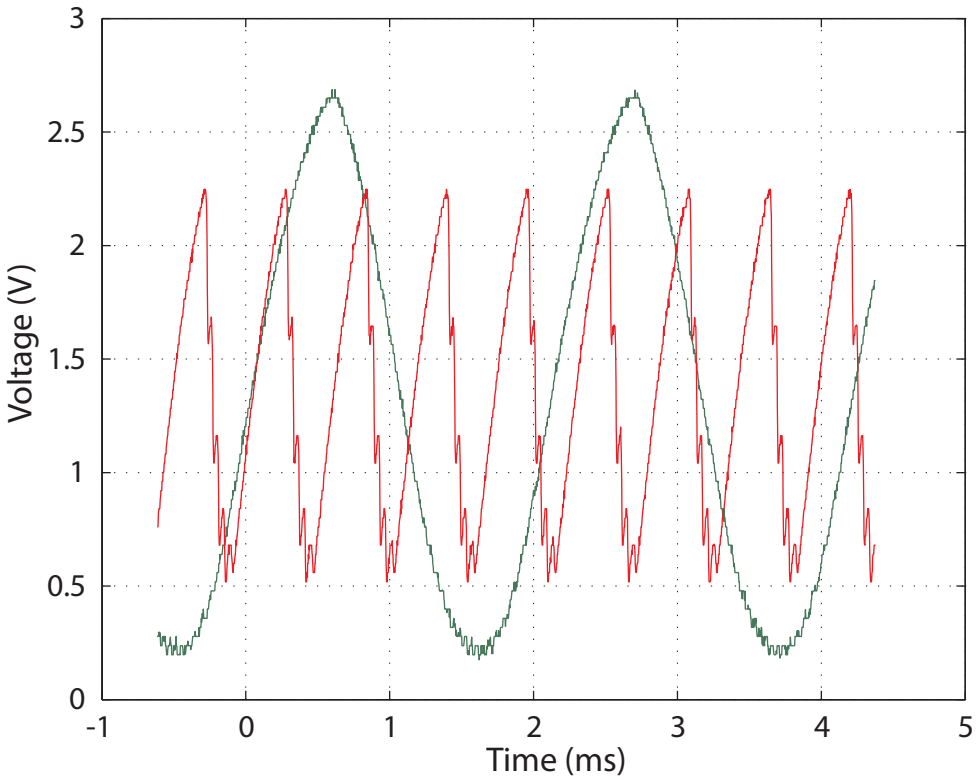


Figure 4.9: The bandwidth of the current control circuit functions as a high frequency noise filter. The 3 dB point of the circuit is determined by measuring the frequency at which the voltage reduces by $1/\sqrt{2}$ and is found from this figure to be 1.8 kHz.

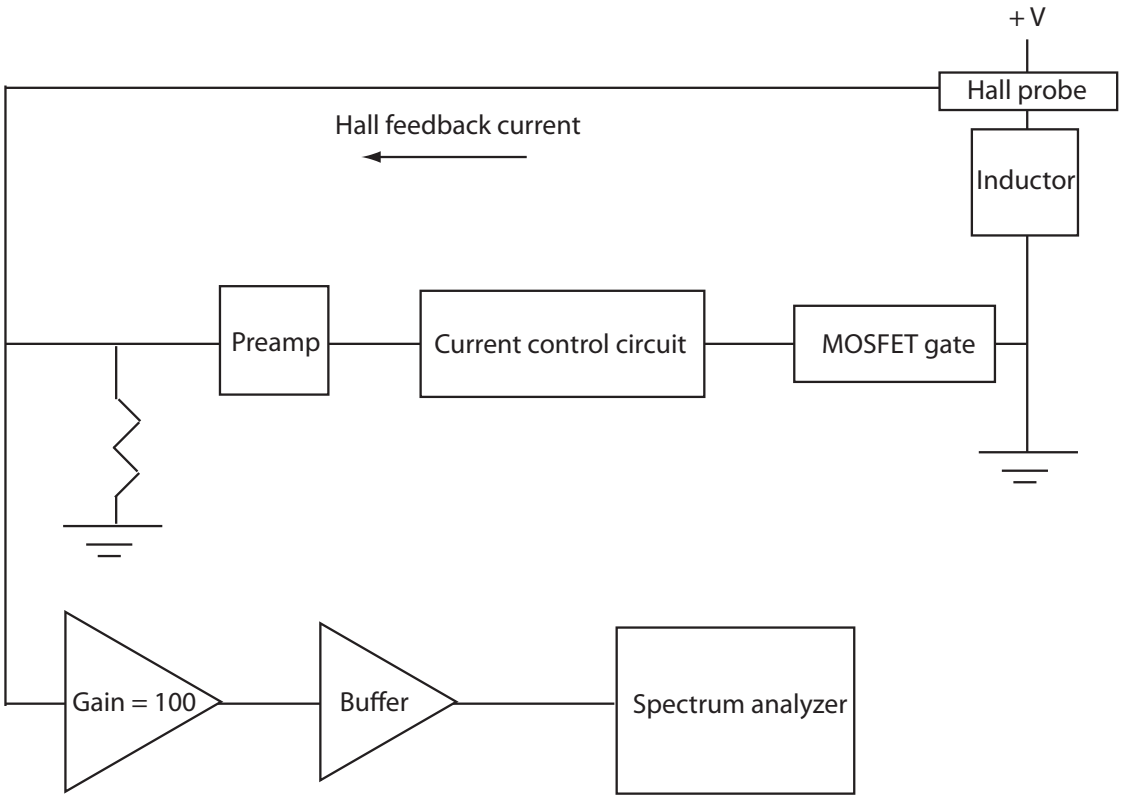


Figure 4.10: Schematic of the current noise measurement system. A preamp is located in the Hall feedback loop. The Hall voltage is used to control the gate voltage on the MOSFET. Noise in the Hall feedback will result in voltage noise at the gate and therefore current noise in the inductor. Amplification of the noise above the noise level of the spectrum analyzer is done by an amplifier and the buffer provides adequate current to the spectrum analyzer.

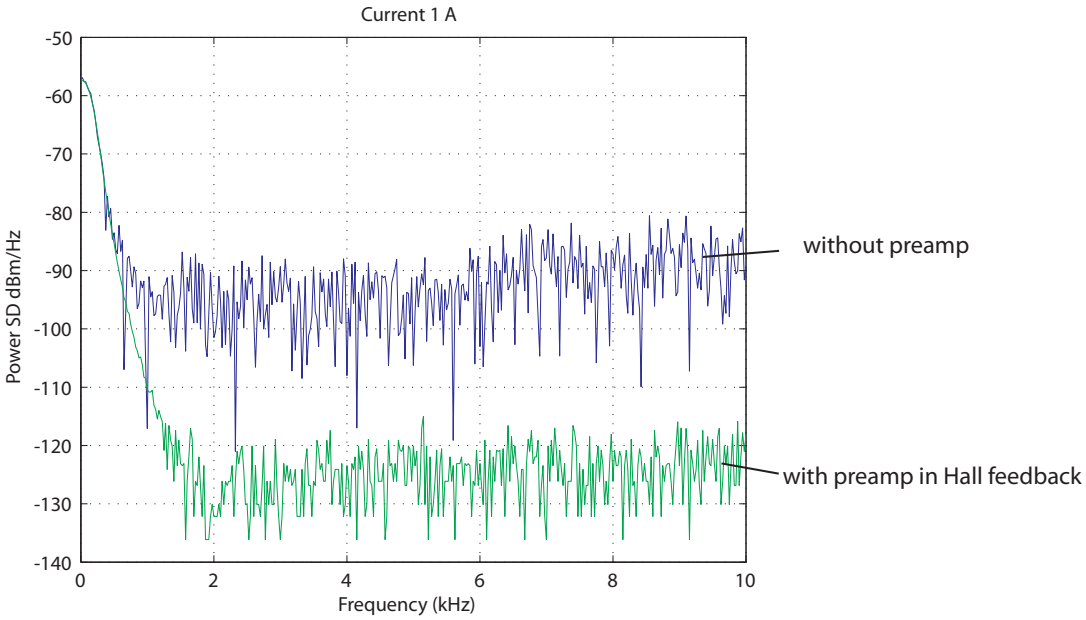


Figure 4.11: Spectrum of the current noise. The noise decreases significantly with use of the preamp in the Hall feedback loop.

CHAPTER 5

# COMPUTER CONTROL OF ATOMIC EXPERIMENT

We often need precise timing control of the instrument system in the atomic experiment. Timing and sequencing control is required for the magnetic fields, laser frequency and intensity, and imaging of the atoms. There are many ways to synchronize an atomic experiment. We use PXI modules developed by National Instruments. PXI modules are essentially signal generators controlled by a computer and have different functions. We often use PXI modules to create pulsed waveforms or arbitrary analog waveforms. All of our labs currently control the PXI modules using interface and server software developed in 2007 by MIT called CICERO and ATTICUS.

## 5.1 CICERO and ATTICUS

Atticus is a server program that establishes the connection from the instrument to the computer. Cicero is a user interface which allows each PXI module to be programmed individually in time steps with the other instruments. Each time step in Cicero is common to all of the PXI modules activated. An example is shown inf Fig. 5.1. Electrical isolation between the instruments running the experiment and the PXI modules is required and serves to protect the expensive PXI modules. Our PXI modules are often of either the analog or digital type, and we have developed homemade circuits for each type to provide electrical isolation.

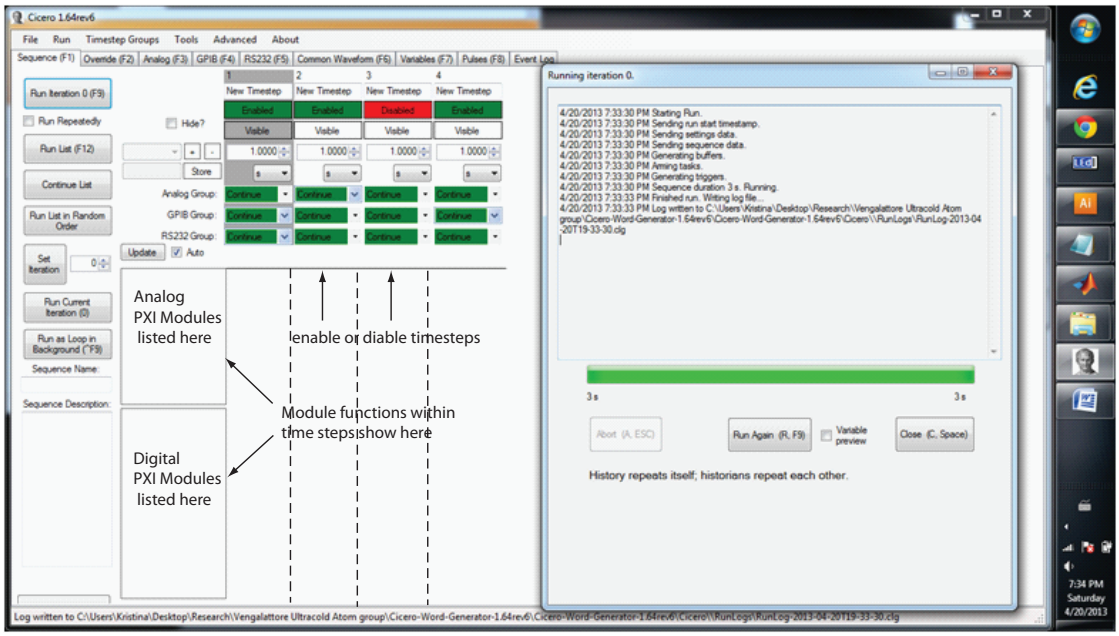


Figure 5.1: Example of the Cicero interface.

## 5.2 Homemade digital input-output electrical isolators

Digital input-output electrical isolator circuits, based on the same design previously implemented in our other labs, provide electrical isolation between the digital PXI modules and the instruments through optoisolation. The TTL signal sent from the digital PXI modules travels through an optoisolator and a SPDT switch. One of the inputs of the SPDT switch is connected to a potentiometer that, when adjusted manually, sets the output voltage of the switch. This gives a range of digital output voltages which can be controlled manually. The signal is then sent through a buffer which provides up to 250 mA of current to an output BNC connector. The schematic for the updated board currently in use is located in the Appendix. Each circuit board contains eight of these DIO circuits and is equipped with a serial connector. The serial connector on the board is attached to a serial fanout board connected to the PXI module. The serial fanout board splits the PXI serial connector into four smaller serial connectors attached

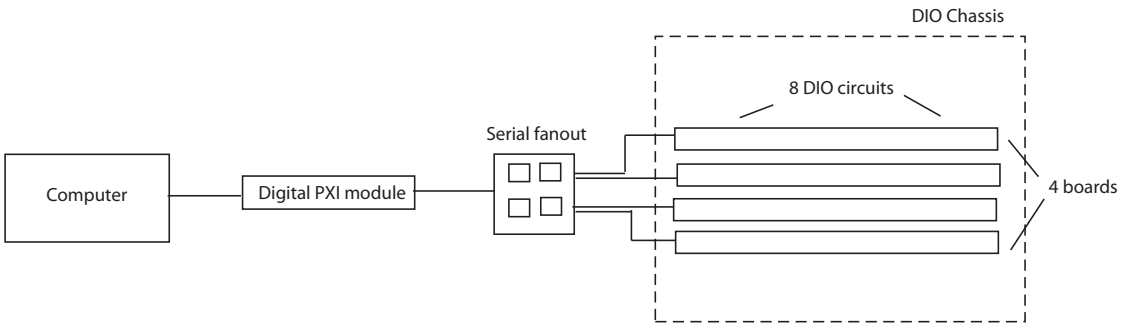


Figure 5.2: Layout of the PXI and digital input-output electrical isolators.

to four different DIO boards, controlling a total of 32 DIO circuits as shown in Fig. 5.2.

### 5.2.1 Digital channel-to-channel crosstalk

Crosstalk between the eight DIO circuits on one board is important to measure so that we know one instrument is not affected by the operation of another. We measure the crosstalk by running a PXI digital signal to one circuit and listening to all other circuits. We also vary the variable output voltage from the minimum to maximum values (0 to 8 V). An example of one of these measurements is shown in Fig. 5.3. Crosstalk between circuits must not be great enough to flip the SPDT switch of the other circuit to a logical high. Crosstalk is well within 5 mV peak-to-peak and does not cause a logical high on the SPDT switch (which has a threshold greater than 1 V).

The rise and fall time of these circuits can be measured simultaneously. The rise times are typically 150 ns and the fall time about 8 ns.

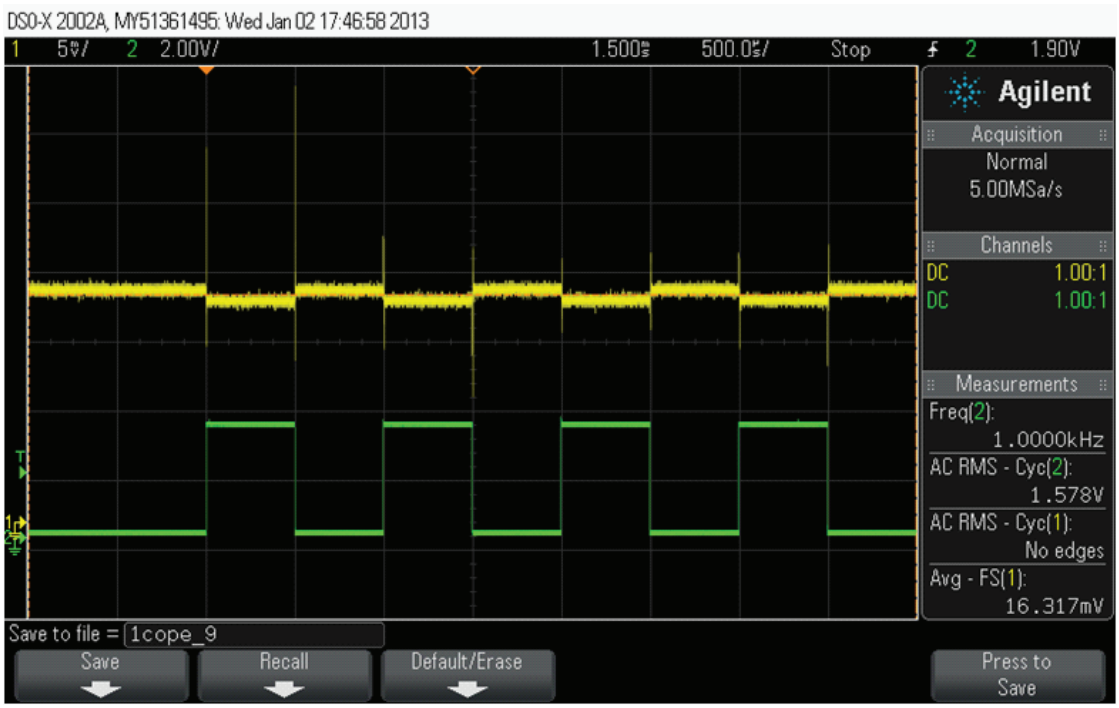


Figure 5.3: One example of a crosstalk measurement of the DIO circuits. The running DIO circuit (green) affects another circuit (yellow) on the DIO board.

## 5.3 Homemade analog electrical isolators

Electrical isolation is also required for the analog PXI modules, and for this we use our homemade analog electrical isolators. The isolators take an input analog signal from the PXI and have the functionality to either output an isolated signal equal to the input or divide the input amplitude by an order of magnitude. A DC output signal can also be generated and controlled manually by a potentiometer. The DC signal level may also be divided by an order of magnitude.

One problem with the analog isolators is voltage instability over the long-term. To ensure that the ground of the analog isolator output is matched to the output ground, a voltage divider provides a voltage offset at the signal input. Another voltage offset is present in the divide by 10 portion of the circuit

to compensate for the op amp configuration providing the dividing function. These potentiometers providing the voltage offset have a tendency to drift over time and as a function of temperature. To minimize the drift as a function of temperature we maximize air cooling between the units. To reduce the effects of the mechanical movement of the potentiometers over time, we minimize the range over which the potentiometer can be adjusted by placing static resistances on both supply voltage extremes. This reduces drifts from occurring over several hours to several weeks. A suggested improvement on this design is to use a high-bandwidth analog optoisolator to provide physical separation between the PXI and the instruments.

CHAPTER 6

# VACUUM SYSTEM

## 6.1 Evolution from 3D to 2D/3D chambers

The lithium vacuum chamber has evolved from a 3D MOT to a 2D/3D MOT combination. At first, we obtained a 3D MOT in the large chamber. Atomic data in this thesis is taken using the 3D chamber. A glass cell was later added to increase the atom number by precooling the atoms in a 2D MOT and pushing them over to the main chamber already at a lower temperature with a push beam directed toward the main chamber. The vacuum of the cell containing the 2D MOT is maintained by an additional vacuum pump. A nozzle maintains the pressure gradient between the lower pressure 3D MOT chamber and the 2D glass cell by limiting the conductance between the two regions. The nozzle assembly consists of a copper tube about 6 in long having an inside diameter of about 1/4 in and is mounted to a solid copper gasket. The tube and gasket assembly is installed on the system in place of a standard gasket. The lithium vacuum chamber design is shown in Fig. 6.1.

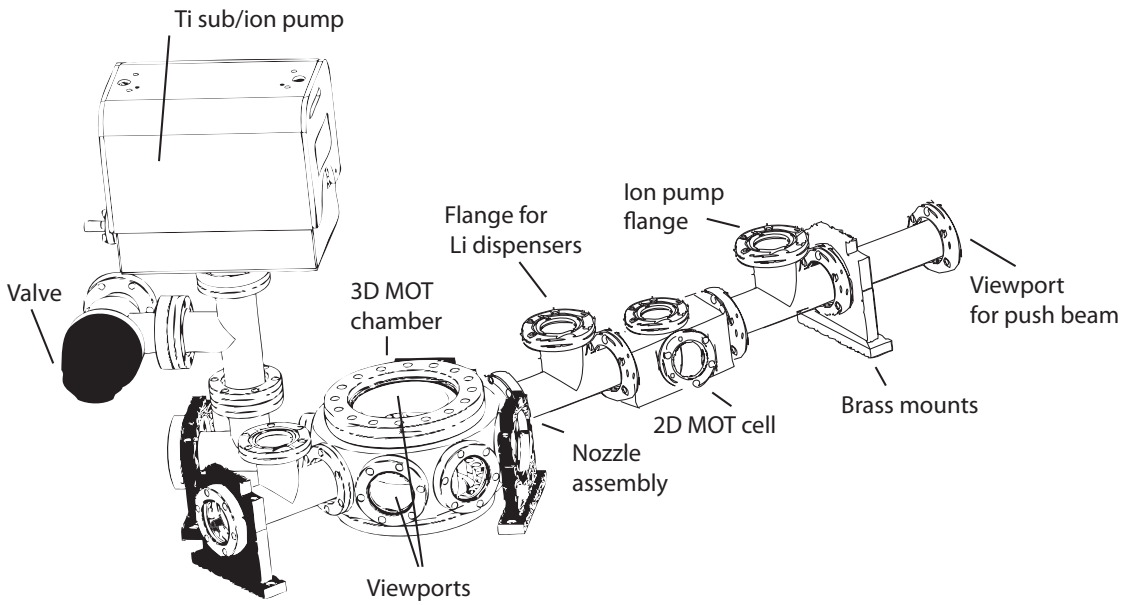


Figure 6.1: Diagram of the 2D/3D MOT lithium vacuum system.

## 6.2 Modifying an ultra-high vacuum chamber

Maintaining ultra-high vacuum is important because atom trap loss and heating rates are often limited by residual background atomic gas or impurities in the vacuum chamber. Background atoms in the chamber are about 300K, and well depths of a dipole trap, for example, are often on the order of $<$ 1mK, and even glancing angle collisions between residual gas atoms and the trapped atoms is enough to cause trap loss. The lowest attainable vacuum pressure also places limits on the lowest number of trapped atoms that can be measured as well as the lowest measurable temperatures [32].

Because the capability of maintaining an ultra-high vacuum must be preserved, modification of the lithium apparatus is often a delicate procedure. The vacuum chamber design described in Section 6.1 and the implementation of this modification requires the involvement of several persons, and through participating in this and other vacuum chamber modifications, some procedural observations and cautions are summarized below.

Pumping down the chamber to an ultra-high vacuum takes place in several stages. When vacuum components are exchanged and vacuum must be broken, the chamber is first flooded with high purity dry nitrogen or argon gas to pressures slightly above atmosphere. The nitrogen gas must be dry because any water content in the gas will condense to the walls of the chamber. Water is an extremely difficult substance to remove from the vacuum chamber walls because the vacuum chamber then needs to be 'baked' or heated over the course of several days or weeks depending on the level of water. Argon gas can be bought ultra-pure having with lower water content, but one must have a vacuum pump that is compatible with noble gases.

The ion pump ionizes atoms and uses a current to move and confine the atoms at its electrodes. Noble gasses do not ionize easily. The Ti sublimation pump operates by heating a titanium filament to the sublimation point of titanium. this coats the nearby walls with pure titanium. Pure titanium is very reactive; when residual atoms come into contact with the titanium coated walls they react with the titanium and form a stable reaction product on the walls. Certain elements such as Helium are not reactive with titanium but can be effectively pumped by the ion pump. The pumping speed of the titanium film degrades as the titanium on the walls reacts with impurities to form stable bonds. The speed can be replenished by the application of another monolayer of titanium onto the walls. The titanium sublimation filaments must be located away from viewports such that there is no line of sight between them. This ensures that the viewports re not subject to titanium deposition. The advantage of using ion and titanium sublimation pumps is that they operate without mechanical vibrations that can limit the lifetime of trapped atoms through optical beam vibrations, for example.

High purity gas is introduced into the vacuum chamber so that air we breathe cannot flow into the chamber while we are replacing vacuum parts. Turbo pumps are equipped with a valve that allows gas flow into the chamber. The turbo pump is mounted onto a flange equipped with a valve. The valve connects the pump to the chamber and is controlled by a manual knob. The chamber must be also closed off from the Ti sublimation pump by a valve to prevent high pressure from destroying the pump. The turbo pump is connected to a roughing pump, and after the turbo pump is connected to the flange near the valve that shuts off the chamber from the turbo pump, the roughing pump begins to pump down the other side of the valve through the turbo pump. Once the valve pressure reaches below 100 milliBar, the turbo pump is turned on and pumps down the valve to about $10^{-7}$ Torr. At the same time, the valve (and everything else exposed to air) must be baked. There runs a risk that impurities on the walls of the components exposed to air might be introduced into the chamber. The turbo pump is turned off and gas may then be introduced into the main chamber.

After filling the chamber with gas to slightly above atmospheric pressure, the vacuum ports can be removed and the components replaced. Upon removing the vacuum ports, one should feel a slight air pressure out of the chamber. The viewports are designed to handle outward pressure, but not inward pressure. It is easy to break the viewports with too much pressure from the gas being introduced into the chamber. During vacuum component replacement, it is useful for one to accomplish all switching processes as quickly as possible to reduce risks to the chamber. After the components are replaced, one shuts off the gas flow and begins the rough and turbo pumping sequence for the valve. The Ti sublimation pump can only be turned on when the lowest pressure of

the turbo pump is achieved. Baking the chamber is necessary if it is exposed to air or cannot reach the desired pressure. Caution must be exercised when baking near ion pumps because the higher temperatures can threaten to partially demagnetize the internal permanent magnets. The temperature is measured by a thermocouple inside of the electric tape which is wrapped on the outside with aluminum foil. The turbo pump stage might need to run overnight to as long as several days. When the system reaches in the region near $10^{-7}$ to $10^{-8}$ Torr, we can terminate the bake-out and switch on the ion pump to reach the region of $10^{-10}$ Torr or lower.

## 6.3 Sonicating ultra-high vacuum components

The process for cleaning ultra-high vacuum components is called sonification. All parts after machining in general are first cleaned with soap and water, then acetone then methanol. The acetone and methanol cleaning sequence is also standard for removing oils from optical components. Acetone first breaks oil bonds and then methanol dissolves the oil residue. After this the vacuum part is sonicated. A sonicator contains a bath of water where ultrasonic compression waves are sent. One must use ear protection. A beaker is filled with a cleaning substance at the same level as the water in the bath, the component is placed in the beaker and the beaker placed in the bath for 8 mins. Alternate the cleaning solution between scientific-grade soap and water twice, and then alternate with acetone and methanol twice. The component must dry completely and be placed in aluminum foil if to be stored.

CHAPTER 7

# CONTROLLING AND CHARACTERIZING ULTRACOLD ATOMIC LITHIUM

## 7.1 Measuring temperature of the ultracold lithium atom cloud

Measuring the temperature of the atom cloud confined in the MOT is a precursor for further steps in the atomic cooling process- the atoms must be at a temperature adequate for confinement in a lattice and subsequent cooling via Raman Sideband Cooling.

### 7.1.1 Atom number from atomic fluorescence imaging

We use a lens and an iris to collect a known amount of light from the fluorescence of the atom cloud. Light from the atom cloud emits uniformly in all directions. Detection of light at a given distance away from the power source corresponds to an approximate detected power,

$$\text{power detected} = \text{total source power}\frac{(\text{area of detection})}{(\text{total surface area of emission})} \tag{7.1}$$

where the amount light collected can be estimated by Fig. 7.1. If the area of detection just corresponded to the area of the photodetector, we would detect very little light, so we use a lens with a large diameter. We place an iris having a diameter that we can control precisely to collect a known fraction of the emitted light.

The scattering rate for lithium is $10^6$ photons/s, and the energy per photon at 671 nm is 2.96x$10^{-13}\frac{J}{s}$. The distance of the iris and lens from the atoms is $8$ cm, and the iris diameter is 2.54 cm. Using these numbers we find the total

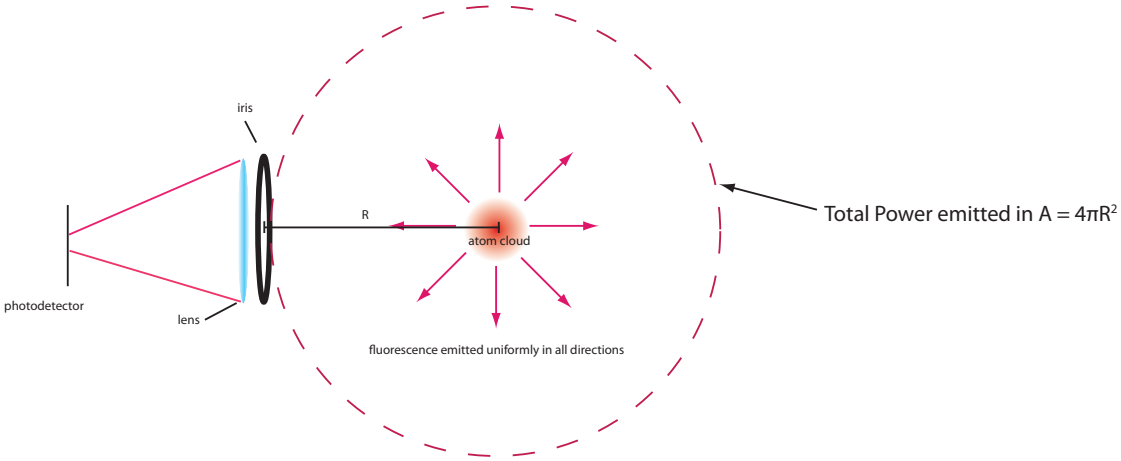


Figure 7.1: The fluorescence from the atoms is emitted in all directions. A fraction of this intensity is collected by the iris and focused by a lens onto the photodetector.

power incident on the photodetector,

$$\left(2.96\text{x}10^{-13}\frac{J}{s}\right)(\#\text{ atoms})\,\frac{2.03\text{x}10^{-3}\text{m}^2}{4\pi\,(.08\text{m})^2} \tag{7.2}$$

$$= 7.47\text{x}10^{-15}\text{W}\,(\#\text{ atoms})\,. \tag{7.3}$$

Relating the power detected to the total photocurrent received, the total photocurrent is,

$$\text{Total photocurrent} = (\text{Power detected})\,R\left[\frac{A}{W}\right](\text{Gain of detector}) \tag{7.4}$$

so,

$$\#\text{ atoms} = \frac{\text{Total photocurrent}}{7.47\text{x}10^{-15}\text{W x}R\left[\frac{\text{A}}{\text{W}}\right]\text{x Gain of detector}}. \tag{7.5}$$

### 7.1.2 Time-of-flight

Time-of-flight is a very common method used for measuring the average temperature of atoms in a MOT. Atoms are released from a magneto-optic trap by turning off the laser power and they expand ballistically, with the hottest atoms

escaping first. As the atom cloud expands, resonant lasers are flashed periodically providing a fluorescence image of the atoms in-situ. The time that the lasers are on must be short enough not to re-trap the atoms, and this time can be determined experimentally after a few trials by observing the size of the atom cloud. (If the lasers are on too long then they will serve to trap and confine the atoms, resulting in a cloud that stays the same size.) The expansion rate of the cloud as a function of time is used to determine the average velocity of the atoms and from this, the average temperature of the cloud.

**Imaging for time-of-flight measurements**

Imaging for time-of-flight measurements requires time synchronization between the camera trigger and lasers that cause atom fluorescence. We know that the efficiency of the AOMs vary as a function of RF drive, so we can use the AOMs to control the cooling and repump laser intensities by controlling the RF drive. The RF drive level is controlled by a voltage signal to the VCOs which is synchronized with the camera trigger. The two signal generators are synchronized to each other through the trigger output. The synchronized signals are sent together through a logic circuit and individually calibrated according to the requirements for each VCO/AOM. Both AOMs can then be triggered simultaneously at maximum and minimum efficiencies. The logic circuit also passes one function generator pulse to trigger the camera in time with the lasers. Fig. 7.2 shows the logic scheme. The images obtained from time-of-flight data show that our MOT has too few atoms to image using this method by fluorescence imaging. Our problem is that the lasers must be on for a long time period (>100 ms) to obtain the fluorescence image, and this time period is long enough for the lasers to trap the atoms again, preventing in-situ imaging of atom cloud

expansion.

### 7.1.3 Release and recapture

Another way to image the atoms is through a technique called release and recapture. This technique is somewhat similar to time-of-flight. Instead of watching the atoms expand we allow them to ballistically expand and escape from the trap, outside of the capture volume. We then turn on the lasers for as long as we need to obtain a fluorescence image and atom number. The delay time between the release of the atoms in the trap and recapture corresponds atom temperature. Shorter delay times correspond to the escape of hotter atoms and longer delay times correspond to the escape of increasingly cooler atoms. Repeated measurements allow us to estimate the average velocity of atoms in the MOT and and the average temperature of the atom cloud.

#### Imaging and fitting release and recapture data

Images of the atom cloud are obtained using a photodiode array (the Grasshopper charge coupled device (CCD) camera) that is triggered externally by a pulse generator; the schematic for the imaging scheme is seen in Fig. 7.2. Data for this section is acquired using the 3D magneto-optical trap where atoms are cooled directly from Li dispensers. A function generator outputs a square pulse longer than 7 seconds, which is greater than the MOT loading time. At the falling edge of the long square pulse, the pulse generator is triggered which outputs a pulse at a manually chosen delay time and pulse duration. The signal from the pulse generator also controls the camera trigger. Because the lasers must be triggered on at exactly the same time and duration as the camera, both signals are sent through an XOR gate that logically combines the signals from the function gen-

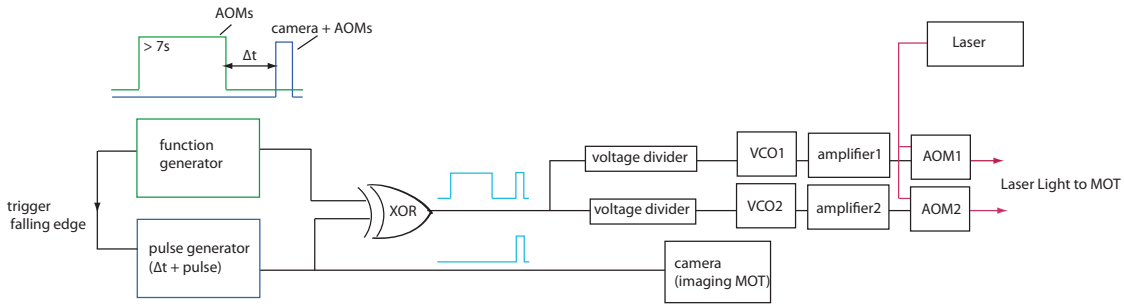


Figure 7.2: Diagram of laser and camera electronic control for obtaining release and recapture data.

erator and the pulse generator. After the voltage signal split to each AOM out of the XOR gate, we place a voltage divider in each line. This allows us to individually maximize the efficiency of each AOM through the RF power level generated by the VCO and amplifier. Using the control setup in Fig. 7.2, we obtain reverse images (where dark spots correspond to bright atom fluorescence), Fig. 7.3. The top image shows a delay $\Delta t$ of 80 $\mu$s, the second 1 ms, and the third at 10 ms. The darkness of the reverse image of atom fluorescence corresponds to the number of atoms. (This is discussed further in the section below.) The first image of the cloud, corresponding to the shortest release time, is visibly darker than clouds taken at 1 ms, and the cloud at delay time of 1 ms is much darker than the cloud at 10 ms. The fluorescence from the MOT is easily seen by eye, and one can also visually see loss of atom number as a function of various delay times. Our Igor program, directly borrowed from and currently utilized in our other laboratories, analyzes the value and distribution of the pixels in these images to calculate atom number. From this, we can calculate the velocity and temperature through using the well-known formula,

$$\sigma_x^2 = \sigma_0^2 + (vt)^2 \tag{7.6}$$

which is the equation governing the ballistic expansion of the atom cloud where $\sigma_0$ is the initial Gaussian radius of the cloud, $\sigma_x$ is the radius at a later time, $v$ is

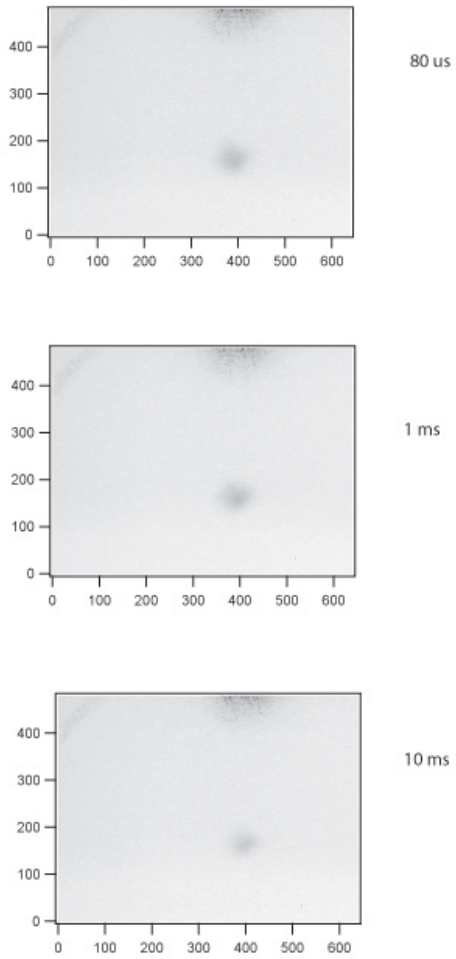


Figure 7.3: Three images of the lithium atom cloud as a function of delay between the time of release and recapture. The atom cloud is located near the center of the images, and residual laser light reflecting from the vacuum chamber appears at the top and near the borders of the image. The axes indicate the number of pixels. The first image is taken with a delay of 80 $\mu$s, the second at 1 ms, and the third at 10 ms.

the average velocity of the atoms, and $t$ is a time. We also know that the atom numbers in the volume are approximately related by,

$$N_x = N_0 \left(\frac{\sigma_0}{\sigma_x}\right)^3 \tag{7.7}$$

so that,

$$\left(\frac{\sigma_x}{\sigma_0}\right)^2 = \left(\frac{N_0}{N_x}\right)^{2/3}. \tag{7.8}$$

Using Eqn. 7.6 we find,

$$N_x = \frac{N_0}{\left[1 + \left(\frac{vt}{\sigma_0}\right)^2\right]^{3/2}}. \tag{7.9}$$

Now we can fit the atom number as a function of time to get an approximate temperature of the atom cloud. An example of one of these measurements is shown in Fig. 7.4. The fit determines c = $v^2/\sigma_0^2$. With $\sigma_0$ = 1/8 in., this corresponds to a temperature of 45 $\mu$K. The temperature should not vary as a function of detuning and capture volume. The measurements gave a temperature variation over an order of magnitude and the analysis must be revisited to determine a reliable atom cloud temperature.

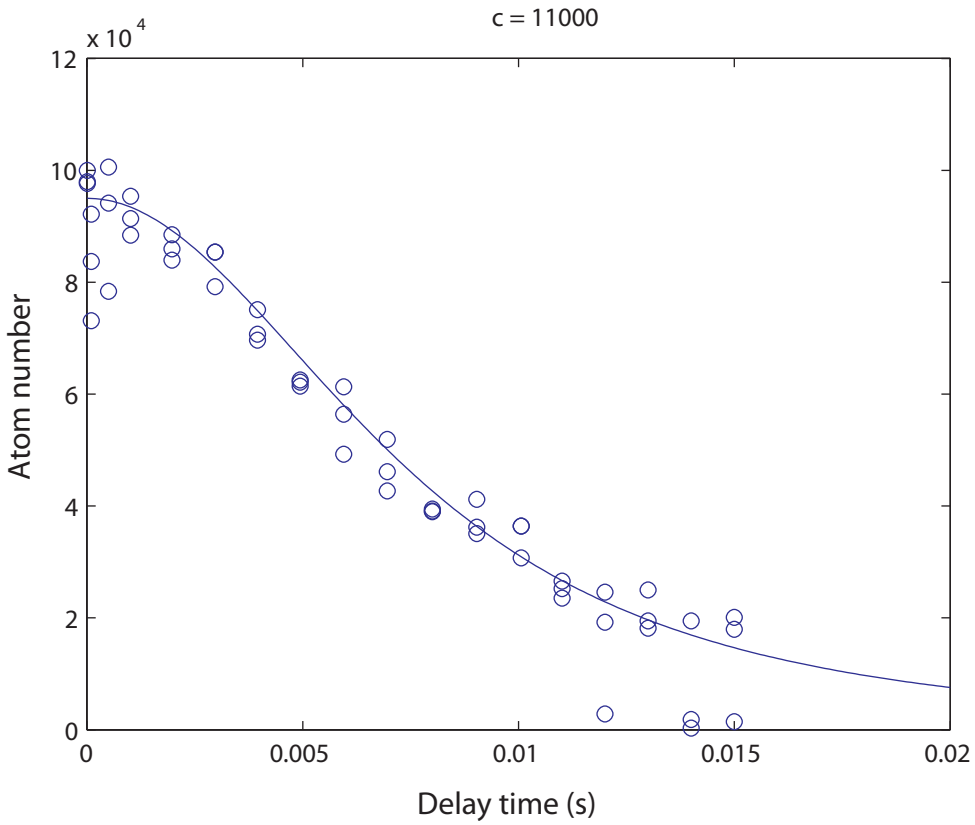


Figure 7.4: Fit of the atom number as a function of time to obtain the temperature of the atom cloud.

APPENDIX A

# IMPROVEMENTS TO THE EXPERIMENT

In the near future, we wish to substantially increase the number of atoms loaded into the 3D MOT. We are hopeful that the 2D MOT paired directly cooling atoms from the lithium oven will serve to initially cool the atoms so that we can obtain a larger number of atoms while maintaining the same low atom temperature in the 3D MOT given the available laser power.

From Eqn. 2.21 and Fig. 2.6, the optical radiation force increases as a function of laser intensity. It also increases at larger atom velocities as a function of greater detunings. However, the heating rate is proportional to the radiation pressure force according to Eqn. 3.11. This implies that transient techniques could also be used to increase the atom number by using a high intensity, large detuning loading stage followed by a low intensity, small detuning cooling stage.

APPENDIX B

# CIRCUIT DIAGRAMS AND SCHEMATICS

## B.1 Digital input-output circuit diagrams

### B.1.1 Updated DIO circuit diagrams

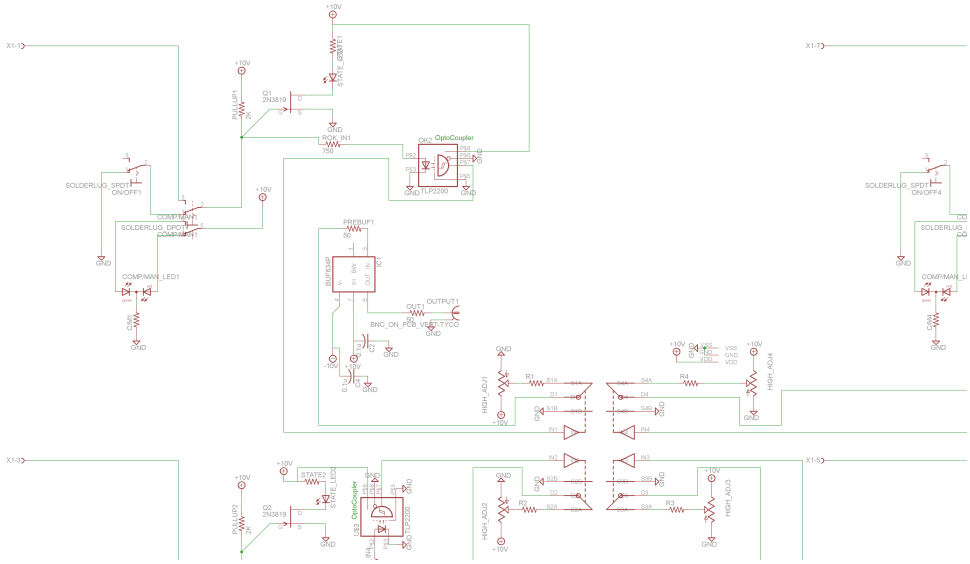

Figure B.1: Schematic of the new digital input-output boards.

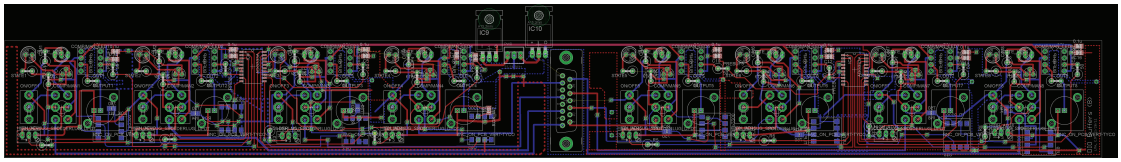

Figure B.2: Board layout of the new digital input-output boards.

### B.1.2 Suggested improvements to DIO board

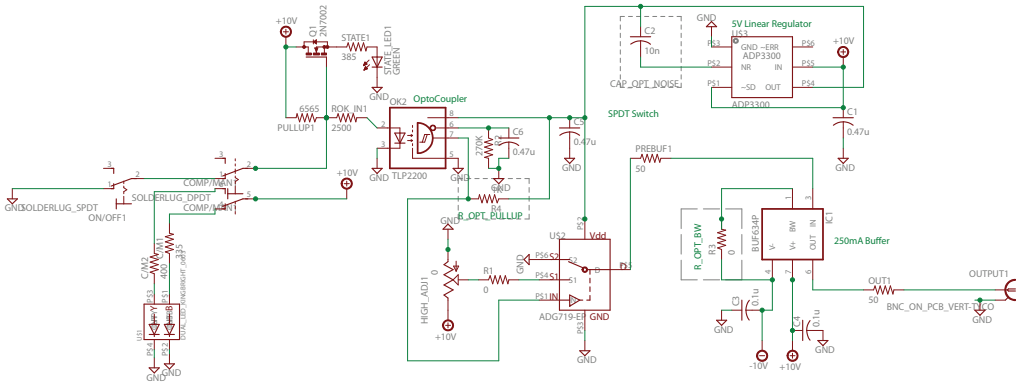


Figure B.3: Suggested improvements to the digital input-output schematic. Each circuit (of the eight circuits on the board) has its own SPDT switch. This allows for a board layout where each channel is independent of the next, it also provides increased electrical isolation between channels through the switch. The optoisolator has its own voltage regulator.

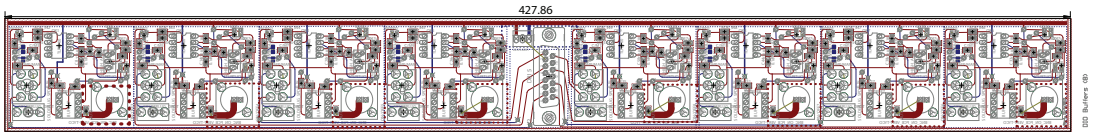


Figure B.4: Suggested improvements to the digital input-output board layout. Each circuit (of the eight circuits on the board) has its own SPDT switch, providing increased electrical isolation between channels. The circuits are wired independently and are not co-located. The output is also better impedance-matched to 50 Ohms through a lower-resistance trace.

## B.2 Helmholtz current control circuit diagrams

### B.2.1 Current control testing diagram and box layout

Current control circuit schematic

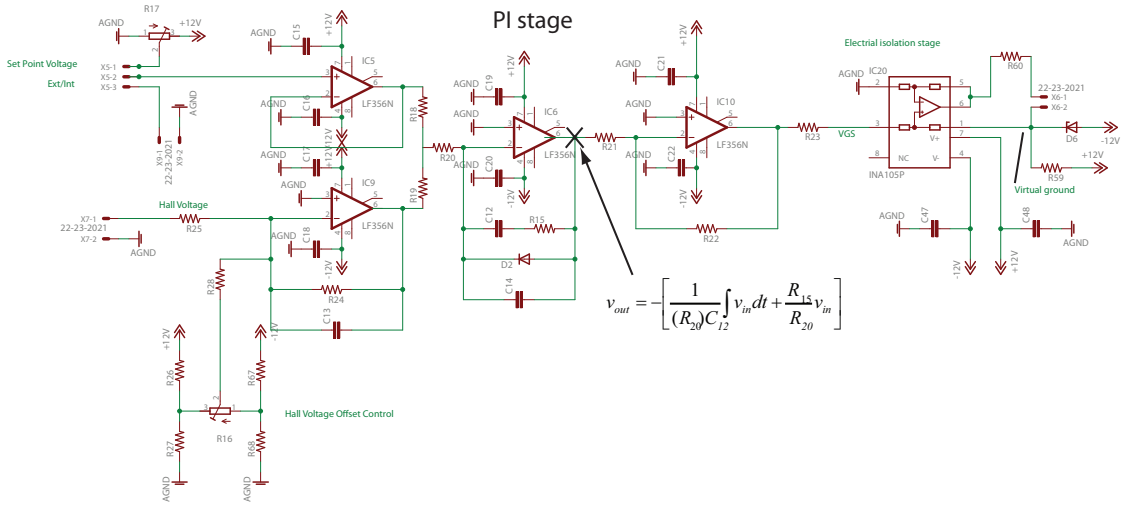


Figure B.5: Schematic of the current control circuit having the same design previously implemented in the other labs. The P and I stages are lumped together and can be adjusted using two resistors and the capacitor in the op amp feedback loop.

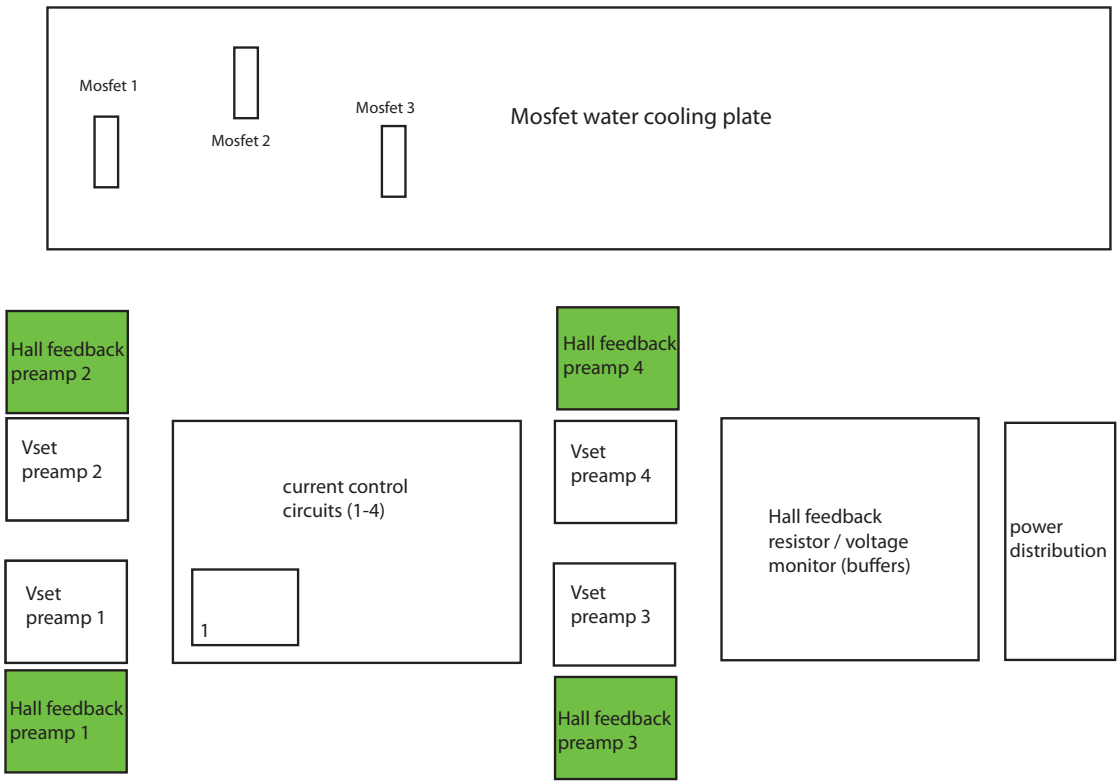


Figure B.6: Diagram of the current control circuit layout.

### B.2.2 Suggested improvements to current control circuit

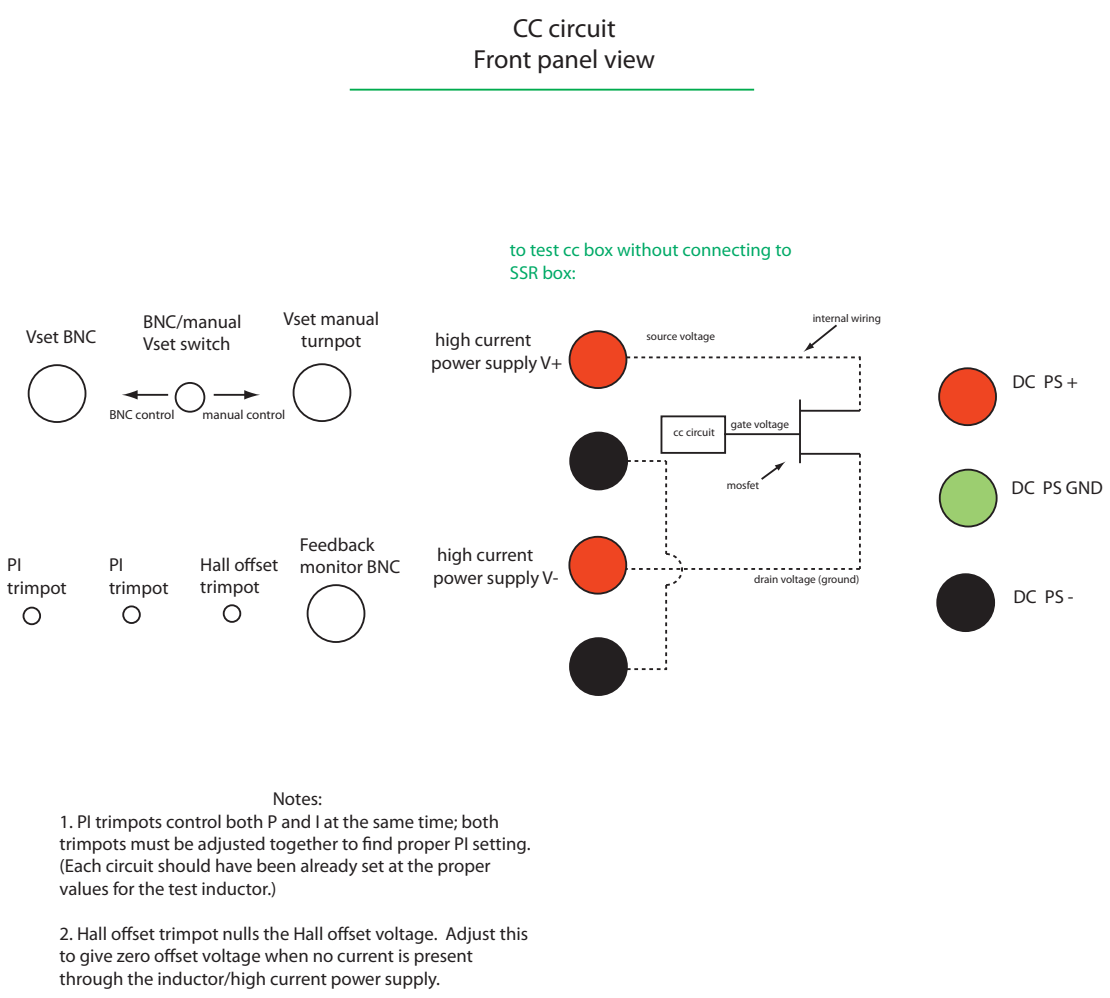


Figure B.7: Diagram of the current control circuit. Shows how to run the current control circuit without connecting to the solid state relay box.

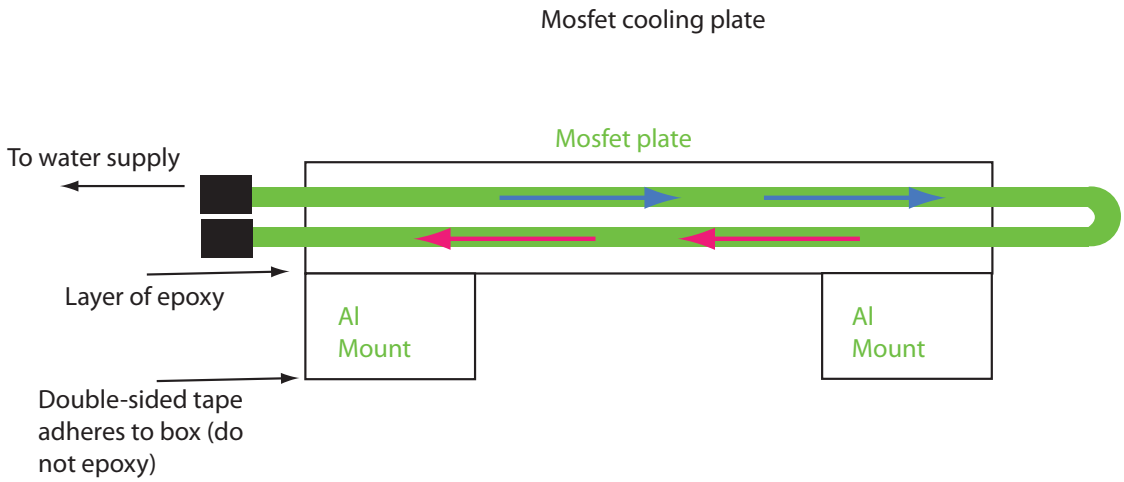


Figure B.8: Diagram of the MOSFET water-cooling plate for mounting inside of circuit box.

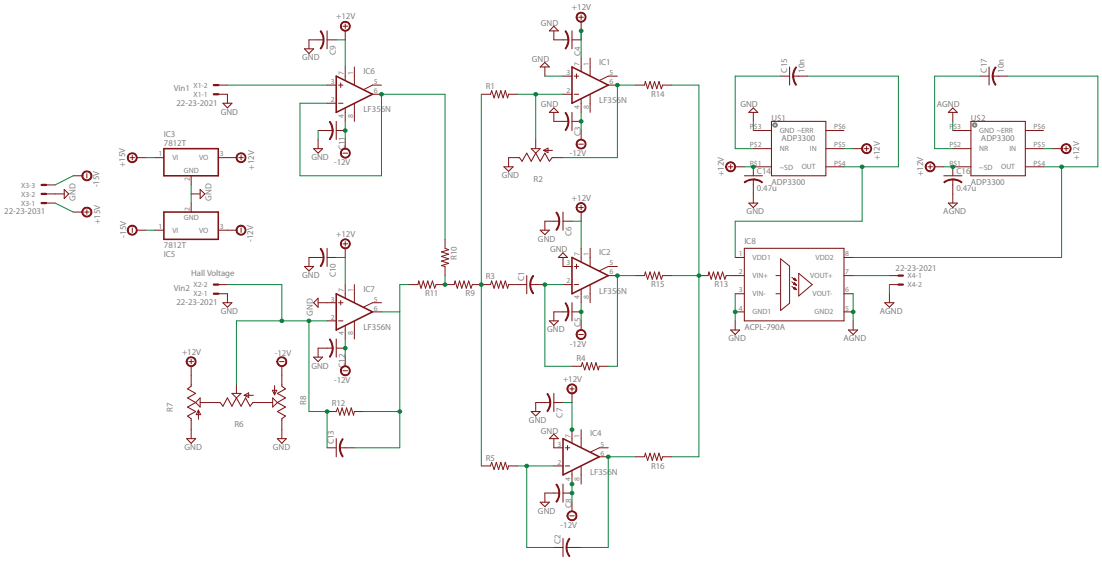

Figure B.9: Suggested improvement to current control circuit. PID parameters are in parallel allowing for individual adjustment. A high-bandwidth optoisolator provides optical isolation between the MOSFET gate and the circuit, physically breaking the current path between the MOSFET and the board.

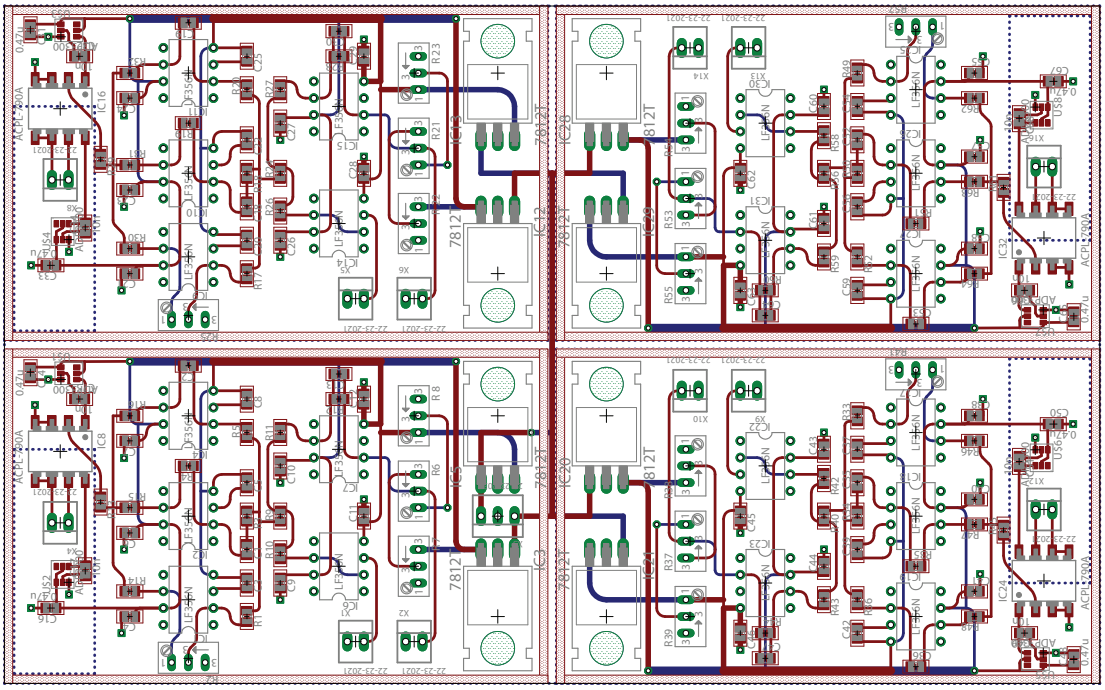

Figure B.10: Corresponding board layout to the improved current control circuit schematic. This board contains four current control circuits, similar to the current layout.

## BIBLIOGRAPHY


[1] A. Ashkin. Trapping of atoms by resonance radiation pressure. *Physical Review Letters*, 40(12):729–732, 1978.

[2] G. Birkl, M. Gatzke, I. H. Deutsch, S. L. Rolston, and W. D. Phillips. Bragg scattering from atoms in optical lattices. *Physical Review Letters*, 75 (15):2823–2826, 1995.

[3] Jr. Burke, J. P., S. Chu, G. W. Bryant, C. J. Williams, and P. S. Julienne. Designing neutral-atom nanotraps with integrated optical waveguides. *Physical Review A*, 65:043411, 2002.

[4] Th Busch, J.R. Anglin, J.I. Cirac, and P. Zoller. Inhibition of spontaneous emission in Fermi gases. *arXiv:cond-mat/9805037v1*, 1998.

[5] M. Cai, O. Painter, and K. J. Vahala. Observation of critical coupling in a fiber taper to a silica-microsphere whispering-gallery mode system. *Physical Review Letters*, 85 (1):74–77, 2000.

[6] W. Chaibi and F. Bondu. Optomechanical issues in the gravitational wave detector Advanced VIRGO. *C. R. Physique*, 12:888–897, 2011.

[7] S. Chu, J.E. Bjorkholm, A. Ashkin, and A. Cable. Experimental observation of optically trapped atoms. *Physical Review Letters*, 57(3):314–317, 1986.

[8] B. DeMarco and D.S. Jin. Spin excitations in a Fermi gas of atoms. *ArXiv:cond-mat/0109098v2*, 2008.

[9] P.M. Duarte, R.A. Hart, J.M. Hitchcock, T.A. Corcovilos, T.-L. Yang, A. Reed, and R.G. Hulet. All-optical production of a lithium quantum gas using narrow-line laser cooling. *arXiv: 1109.6635v2*, 2012.

[10] M. Eichenfield, Chan. J., R.M. Camacho, and O. Painter. Optomechanics of phononic-photonic crystal defect cavities. *Proceedings of CLEO/IQEC*, page CPDB9, 2009.

[11] Michael E. Gehm. Properties of $^6$Li, February 2003.

[12] F. Gerbier and Y. Castin. Heating rates for an atom in a far-detuned optical lattice. *Physical Review A*, 82, 2010.

[13] V. Gokhroo, G. Rajalakshmi, R. K. Easwaran, and C. S. Unnikrishnan. Sub-Doppler deep-cooled bosonic and fermionic isotopes of potassium in a compact 2d+-3d MOT set-up. *Journal of Physics B: Atomic, Molecular and Optical Physics*, 44:115307, 2011.

[14] R. Grimm and M. Weidemüller. Optical dipole traps for neutral atoms. *arXive*, arXiv:physics/9902072v1, 1999.

[15] G. Heinrich and F. Marquardt. Coupled multimode optomechanics in the microwave regime. *arXiv:1005.2155v1*, 2010.

[16] J.E. Hoffman, J.A Grover, Z. Kim, A.K. Wood, J.R. Anderson, A. J. Dragt, M. Hafezi, and C. J. Lobb. Atoms talking to SQUIDs. *Revista Mexicana de Física S*, 57(3):1–5, 2011.

[17] P.S. Jessen and I. H. Deutsch. Optical lattices. In *Advances in Atomic, Molecular and Optical Physics 37*. Academic Press, 1996.

[18] T. J. Kippenberg. Cavity optomechanics, August 2012.

[19] J. Lee, D. H. Park, S. Mittal, M. Dagenais, and S. L. Rolston. Integrated optical dipole trap for cold neutral atoms with an optical waveguide coupler. *arXiv:1303.2922v1*, 2013.

[20] H. Mabuchi and A.C. Doherty. Cavity quantum electrodynamics: Coherence in context. *Science*, 298:1372–1376, 2012.

[21] R. Marani, L. Cognet, V. Savalli, N. Westbrook, C. Westbrook, and A. Aspect. Using atomic interference to probe atom-surface interaction. *arXiv: physics0001015v1*, 2008.

[22] Kimball Milton. Resource letter VWCPF-1: van der Waals and Casimir-Polder forces. *American Journal of Physics*, 79:697, 2011.

[23] G. Modugno, C. Benkő, P. Hannaford, G. Roati, and M. Inguscio. Sub-Doppler laser cooling of fermionic $^{40}$K atoms. *Physical Review A*, 60 (5):R3373–R3376, 1999.

[24] Kenneth Martin O'Hara. *Optical trapping and evaporative cooling of fermionic atoms*. PhD thesis, Duke University, 2000.

[25] J.D. Pritchard, J.A. Isaacs, M.A Beck, R. McDermott, and M. Saffman. Hybrid atom-photon quantum gate in a superconducting microwave resonator. *ArXiv:1310.3910v1*, 2013.

[26] A. Schliesser. *Cavity optomechanics and optical frequency comb generation with silica whispering-gallery-mode microresonators*. PhD thesis, Ludwig-Maximilians-Universität München, 2009.

[27] A. Schliesser and T. J. Kippenberg. Hybrid atom-optomechanics. *Physics*, 4:97, 2011.

[28] Anetsberger G. Rivière R. Schliesser, A., O. Arcizet, and T. J. Kippenberg. High-sensitivity monitoring of micromechanical vibration using optical whispering gallery mode resonators. *ArXiv:0805.1608v1 [quant-ph]*, 2008.

[29] S. Singh, H. Jing, E. M. Wright, and P. Meystre. Quantum state transfer between a Bose-Einstein condensate and an optomechanical mirror. *ArXiv:1202.6100v1 [quant-ph]*, 2012.

[30] J.D. Thompson, B.M. Zwickl, A.M. Jayich, F. Marquardt, S.M. Girvin, and J.G.E. Harris. Strong dispersive coupling of a high-finesse cavity to a micromechanical membrane. *Nature*, 452:72–5, 2008.

[31] Stefan Alexander Weis. *Cavity-Optomechanics with Silica Mircotoroids: Quantum Coherent Coupling and Optomechanically Induced Transparency*. PhD thesis, École Polytechnique Fédérale de Lausanne, 2012.

[32] X. Xu, T.H. Loftus, J.W. Dunn, C.H. Greene, J.L. Hall, A. Gallagher, and J. Ye. Single-stage sub-Doppler cooling of alkaline earth atoms. *Physical Review Letters*, 90 (19):193002, 2003.